POLYTECHNICS OF TURIN

Master's Degree in Mechanical Engineering

Master's Degree Thesis

Modeling of Mechanical Transmission for Hybrid-Electric Propulsion Aircraft

Supervisors

Prof. Massimo Sorli

Ing. Antonio Carlo Bertolino

Ing. Andrea De Martin

Ing. Roberto Guida

Candidate

280264 Luigi Pulvirenti

December 2023

Summary

The thesis focuses on the purely dynamic rotation model of a dual-stage planetary transmission for a hybrid turboprop aircraft for regional transport. The model generates the mass of the entire transmission and the dynamic response of the same as a function of the relative phases of flight, through precise inputs (power and rotational speeds of turbine and electric motor, propeller speed and overall gear ratio).

Subsequently, in the second chapter, three possible architectures were chosen (Off-Set, In-Line and Mixed) and the same were dimensioned both in conventional propulsion and in hybrid propulsion. All aimed at maximizing the specific power and compactness of the transmission, thus arriving at the choice of the hybrid planetary dual-stage (In-Line) architecture with electric motor axial flow at low speeds, coaxial to the turbine, connected to the first stage carrier with a power density of about 18 kW/kg.

The third chapter focuses on the dynamic analysis of the transmission, which has been simulated through a model with concentrated parameters: the gears are modelled as a full disk with concentrated inertia; transmission shafts as torsional springs with stiffness and damping dependent on mass and inertia; meshing by non-linear springs, with stiffness in one case and in another case dependent on the frequency of meshing, positioned parallel to dampers. All this was accompanied by models that simulated the behaviour of the gas turbine, the electric motor, the propeller, the angle of the propeller and the atmosphere.

The fourth chapter analyses the results of the dynamic model in the various phases of flight of an aircraft, such as take-off, ascent, cruise, descent and landing, in conventional propulsion, hybrid and totally electric.

Finally, the fifth chapter sets out possible future developments in work.

Acknowledgements

Alla mia famiglia, ai miei nonni, ai miei genitori e mia sorella, senza i quali oggi non sarei dove sono.

"Luigi Pulvirenti"

Table of Contents

List of Tables

List of Figures

Acronyms

GB

Gearbox

cGB

Combined Gearbox

EM

Electric Motor

GR

Gear Ratio

TE

Thermal Engine

GT

Gas Turbine

ICE

Internal Combustion Engine

MAPE

Mean Average Percentage Error [$-$]

i,r,a,t,n,s,c,p

General, Radial, Axial, Tangential, Normal subscript, Sun, Carrier, Planet

Chapter 1

Introduction

1.1 Environmental Pollution in Aircraft Transport

The aerospace industry has undergone a remarkable transformation in recent decades, enabling people to travel around the world faster, more safely, and more conveniently than ever before. However, this progress has come at a cost, particularly in terms of the environmental impact of aviation. The aviation industry is responsible for a significant amount of pollution, including greenhouse gas emissions and other harmful pollutants that have far-reaching consequences for the health and well-being of people and the planet.

According to the International Civil Aviation Organization (ICAO), Valdes et al. [1], global aviation accounted for approximately 2.1% of all carbon dioxide (CO_2) emissions in 2019, that is 915 million out of 43 billion tons total, and it is responsible for 12% of CO_2 emission from all transports source. This figure is projected to increase as air travel continues to grow, particularly in emerging economies such as India and China, where demand for air travel is rapidly expanding. In addition to carbon dioxide emissions, aviation also generates other pollutants, including nitrogen oxides (NO_x), sulfur oxides (SO_x), particulate matter, and volatile organic compounds, which contribute to air pollution, smog, acid rain, and other environmental problems.

Moreover, from 2013 to 2018 the emissions are increased of 32% and it is expected that in 2050 they will rise to 2.35 billion tons, 2.6 times those of 2019, with an increase of 20% percentage points compared to today, going to represent the 22% of the world pollution [2].

The impact of aviation pollution on the environment and human health has been extensively researched and documented. Air pollution caused by aviation can lead to respiratory and cardiovascular diseases, as well as premature death, particularly in urban areas near airports. Furthermore, aviation emissions contribute to global warming and climate change, which have serious and potentially catastrophic consequences for the planet and future generations.

Given the scale and severity of the environmental impact of aviation, the aerospace industry has recognized the need to take action to reduce its carbon footprint and develop sustainable practices.

In recent years, to reduce CO_2 emissions and the consequent pollution, significant progress has been made in developing new technologies and alternative fuels that have the potential to reduce aviation's environmental impact significantly. For example, the use of biofuels and the development of hybrid and electric aircraft, such as the Pipistrel Velis Electro[3], which has shown promising results in reducing emissions and increasing energy efficiency. Or Nasa X-57 Maxwell [4], also known as the X-plane is an experimental aircraft being developed by NASA based on a modified Tecnam P2006T aircraft, which will be fitted with 14 electric motors and propellers distributed across its wings and it is designed to be highly efficient and quiet, and powered by a set of lithium-ion batteries to purpose to reduce fuel consumption, noise and emissions. The X-57 program has several phases, with the first phase involving ground and flight tests of the aircraft's electric propulsion system. The second phase will involve the modification of the aircraft's wings, with the addition of high-lift motors and propellers, to further improve its aerodynamic performance.

Another example can be the collaboration between Airbus, Roll Royce and Siemens, to purpose to develop a regional turboprop like E-Fan-X. According to the press release [5], the E-Fan X project aimed to replace one of the four gas turbine engines on a BAe 146 regional airliner with a 2MW electric motor, with the ultimate goal of replacing all four gas turbines with electric motors. The electric motor was powered by a 2MW generator, which was driven by a Rolls-Royce AE 2100 gas turbine engine and the power electronics for the system were designed and supplied by Siemens. The project aimed to achieve a power density of 5kW/kg, which would require significant advances in battery technology. The E-Fan X was expected to have a range of around 300 nautical miles and a maximum cruise speed of Mach 0.8.

Another cooperative work followed by Airbus with Dahar and Safran is the EcoPulse [6] [7], a hybrid-electric aircraft. The project is part of the European Union's Clean Sky 2 program, which is a program with two purposes: to reduce CO2 emissions by 40% by 2030 and 80% by 2050, compared to 1990 levels; and to maintain Europe's competitiveness in global aviation industry by developing new technologies that will help to reduce costs, improve efficiency, and enhance the passenger experience.

The EcoPulse aircraft is based on Daher's TBM 900 turboprop aircraft and incorporates Safran's ENGINeUS electric motor and Airbus' wing technology.

The aircraft is designed to operate in a hybrid mode, using both the traditional turboprop engine and the electric motor for takeoff and climb, and relying on the turboprop engine for cruising. Using the electric motor in this way is possible to reduce fuel consumption and emissions during takeoff and climb, which are the most fuel-intensive phases of flight. In terms of performance, the EcoPulse aircraft is expected to have a 30% reduction in fuel consumption and emissions compared to a traditional turboprop aircraft. The aircraft is also expected to have a cruising speed of 330 knots and a range of up to 1,000 nautical miles.

However, the EcoPulse project is still in the development phase, and further testing and validation are needed to ensure its safety and airworthiness for commercial use. Additionally, there are still challenges to overcome in terms of battery technology and infrastructure for electric charging in aviation.

In the end, coming back to more extended overall view there are many political interests, European and not, to reduce the pollution of air and so the footprint of CO_2. In fact, the Fit for 55 proposals is a package of legislative measures proposed by the European Commission in July 2021 to reduce greenhouse gas emissions by at least 55% by 2030, compared to 1990 levels, as part of the European Union's efforts to tackle climate change.

The proposal includes a range of measures, such as:

- Increasing the share of renewable energy in the EU's energy mix to 40% by 2030
- Setting binding national targets for energy efficiency, with a view to achieving a 36-39% improvement in energy efficiency by 2030
- Introducing a Carbon Border Adjustment Mechanism (CBAM) to ensure that imported goods are subject to the same carbon pricing as products made in the EU (a carbon tax to import/export)
- Expanding the EU emissions trading system (ETS) to cover new sectors, such as shipping and buildings, and lowering the emissions cap over time
- Promoting the deployment of clean hydrogen and sustainable fuels (New Fuels)
- Encouraging the use of electric vehicles through stricter CO2 emissions standards for cars and vans (Automotive)
- Introducing a tax on aviation fuel and ending tax exemptions for shipping and aviation fuels (Clean Sky 20)

Or international organizations and government agencies that have developed policies and initiatives to address the environmental impact of aviation. In this case, ICAO has developed a global framework for reducing aviation emissions, known as the Carbon Offsetting and Reduction Scheme for International Aviation (CORSIA), which aims to achieve carbon-neutral growth from 2020 onwards. Furthermore, some countries have implemented emissions trading schemes or introduced taxes on aviation fuel to incentivize airlines to reduce their carbon footprint.

Despite these efforts, there is still much to be done to achieve sustainable aviation and mitigate the impact of air transport on the environment. However, it is not discussible that there is an international and world collective engagement to follow all possible streets, from bio-fuel to more electric, to reduce the dependence on fossil fuels and going more and more to green transport.

1.2 State of Art

Cameretti et al.[8], are concentrated on the development of mathematical models which describe the behaviour of the various components of turboprop hybrid electric propulsion systems.

The components of the system include the Gas Turbine engine (GT), the Electric Motor (EM), the battery, and the propeller. The mathematical models are used to simulate the behaviour of the system under different operating conditions and to predict its performance.

The gas turbine engine is modelled using thermodynamic principles, which describe the flow of air through the engine and the combustion of fuel.

The electric motor is modelled using electromagnetic principles, which describe the interaction between the magnetic fields produced by the motor and the electrical currents flowing through it.

The battery is modelled using electrochemical principles, which describe the chemical reactions that take place inside the battery to produce and store electrical energy.

The propeller is modelled using aerodynamic principles, which describe the flow of air over the blades of the propeller and the resulting thrust generated by the propeller.

The purpose of all this is the analysis of the system's performance under different operating conditions to evaluate many factors like fuel consumption, emissions, noise, efficiency, and reliability.

In fact, fuel consumption is an important factor to consider when evaluating the performance of a hybrid electric propulsion system. The use of electric power can reduce the amount of fuel required by the gas turbine engine, resulting in lower fuel consumption and reduced emissions. However, the battery must be charged using energy from a power source, which may also consume fossil fuels.

In this case, they have been considered a conventional turboprop, with a base configuration with ATR42-300 and PW120, a second configuration with two PT6A-67-F respect than PW120, and a third configuration whit two PT6A-68 always respect than PW120. The difference between the base configuration with all the others consist in the second and third configurations are two smaller turbine respect than the original. After this change, a comparison between emissions of CO_2 and NOx is performed, with all other constraints held constant.

Emissions are another important factor to consider when evaluating the performance of a hybrid electric propulsion system. The use of electric power can reduce the emissions of pollutants, maxima in the take-off phase, such as nitrogen oxides (NOx) and particulate matter, from the GT engine. In fact, for instance, by increasing the hybridization rate the specific fuel consumption decrease, but the weight of the battery pack increase.

However, the emissions associated with the production and distribution of electricity must also be considered.

Noise is a third factor to consider when evaluating the performance of a hybrid electric propulsion system. The use of electric power can reduce the noise generated by the GT engine and resulting it in being quieter than conventional aircraft. However, the noise generated by the EM must also be considered.

Efficiency is a fourth factor to consider when evaluating the performance of a hybrid electric propulsion system. The use of electric power can increase the overall efficiency of the propulsion system, resulting in lower operating costs and improved range. However, the efficiency of the battery and the electric motor, the power density and the energy density of the battery must also be considered.

Reliability is a final factor to consider when evaluating the performance of a hybrid electric propulsion system. The use of multiple power sources, such as the GT engine and the battery, can increase the reliability of the propulsion system by providing redundancy. However, the reliability of each component of the system must be considered.

In conclusion, the modelling and investigation of a turboprop hybrid electric propulsion system is a complex task that requires the development of mathematical models and the analysis of performance under different operating conditions. The use of electric power and the continuous improvement of this technology can provide a number of benefits, including reduced fuel consumption, emissions, and noise, as well as increased efficiency and reliability. However, the performance of the system must be evaluated based on a number of factors, including fuel consumption, emissions, noise, efficiency, and reliability.

Other than this the study doesn't give relevant information about models for the gearbox mass estimation and how the weight of this changes between the conventional and the hybrid layouts of the system.

Vakan [9] highlights how full electric propulsion for civil aircraft to medium and long-range nowadays is not possible with the current state of technology, but he says also how there are advantages to use an electric motor. For instance, it's useful to use regenerative braking, to recharge the electric motor, when the aircraft is in flight and the propellers are spinning in a descent flight phase.

This means generating electric energy to recharge the battery pack when the aircraft is descending. When the aircraft will take off again, this stored energy can be used to power the electric motor and provide additional thrust to the gas turbine engine, reducing the amount of fuel needed. Or the electric motor can be used to provide propulsion during ground operations or it can give additional power during takeoff and climb, reducing the aircraft's takeoff distance and improving its rate of climb. In every case, it can further reduce fuel consumption and emissions.

However, there are also some challenges associated with implementing a parallel hybrid electric propulsion architecture for single-aisle aircraft. One of the main challenges is the weight and size of the battery pack needed to power the electric motor. The battery pack needs to be large enough to store sufficient energy to provide additional thrust during takeoff and climb, but it also needs to be lightweight to avoid adding too much weight to the aircraft. That means that a goal of the near future will be improving the power and energy density of these.

Unfortunately, also Vakan doesn't give a relevant information about the gearbox

Speirlign [10] starts talking about the benefits of a parallel hybrid propulsion system for a regional turboprop including:

Improved fuel efficiency: the electric motor assists the thermal engine, in this case an internal combustion engine (ICE), during takeoff and climb, and doing this the ICE can be operated at a more efficient level during cruise, further reducing fuel consumption

Reduced emissions: The electric motor produces zero emissions

Improved performance: The electric motor can provide additional power during takeoff and climb, improving the aircraft's performance and reducing the runway length required for takeoff.

Increased reliability: The hybrid system provides redundancy in case of engine failure, as the electric motor can be used to continue powering the aircraft in the event of an ICE failure.

Lower operating costs: reducing fuel consumption, therefore, decreasing operative costs

All of this is centred on vehicle Bombardier Dash 8-100 equipped by PW121 in a 250nm mission. The system has been sized to serve the gas turbine at maximum efficiency in all flight missions, which means that the gas turbine operates at a fixed point and the electric motor gives energy in critical phases.

The total power in take-off are given in this way:

- Take-off power: 1950 hp (1454kW) given for 51.3% (1000hp) by gas turbine engine and 48.7% by an electric motor (950hp)

- Cruise power: totally given by gas turbine

In this way, if conventional propulsion has a 30% of thermal efficiency, it's possible to get another 10%, which means 40% of the total efficiency of hybrid propulsion.

The consequence is the fuel saving is equal respectively to 25% and 30% in a short range of mission profile (250NM)

Unfortunately, also in this study, the authors are focused on the electrical part, on the battery storage, on the electric component and on the saving fuel, but they not given information about the weight of the gearbox (the only relevant information of the gearbox is an increase of 100 kg for parallel configuration)

It is clear such as in the state of art all references and studies are focused on the electric engine point of view when talking about hybrid aircraft and how the available performance is strongly dependent on the weight of the aircraft itself and the battery pack adopted. In fact, many studies analyze how the possible autonomy of aircraft depends on the hybridization rate, on the power density of the electric motor and on the energy density of the battery. In all of these studies, there isn't relevant information on how the gearbox changes between conventional layout and hybrid layout, nor the approximation of transmission itself for hybrid aeroplanes.

The only useful information about GB mass estimation (Table 1.1) are concentrated in three formulas: NASA '15, WATE 2 and Willis 1963.

These are helpful to estimate the Gearbox mass in conventional propulsion

Model-Year	Reference	$f(X)$
NASA 2015	[10]	$m_{GB}[kg] = f\left(P_{eng,[kW]}; N_{rotors,[-]}; \omega_{eng,[RPM]}; \omega_{prop,[RPM]}\right)$
WATE 2 1983	[11]	$m_{GB}[kg] = f\left(Torque_{[lb \cdot ft]}; \omega_{eng,[RPM]}; \omega_{prop,[RPM]}\right)$
Willis 1963	[12]	$m_{GB}[kg] = f\left(Torque_{[Nm]}; \omega_{eng,[RPM]}; N_{pl,[-]}; k\right)$
NASA 2005	[13]	$m_{GB}[kg] = f\left(Power_{[kW]}; \omega_{eng,[RPM]}; \omega_{prop,[RPM]}; k_{[-]}\right)$
NASA 1978	[14]	$m_{GB}[kg] = f\left(Power_{[kW]}; \omega_{eng,[RPM]}; \omega_{prop,[RPM]}\right)$

Table 1.1: Gearbox mass estimation methods

In this sense, the aim of this thesis is to explore one of the possible solutions to decrease the world pollution caused by the aerospace sector, such as using parallel hybrid propulsion systems for regional turboprop transport. The idea is to use the same power as conventional propulsion using a thermal engine combined with an electric engine. Doing this will be possible to use a smaller thermal engine, lighter, with less burned fuel and with fewer pollution missions, together with an electric engine which will give the power in critical phases, like for instance the take-off. To do this, our focus will be to manage both powers to input in the gearbox and transmit these to the propeller. So, from point of gearbox view, this means taking the high powers and low torques of two input-independent and parallel high-speed shafts, a thermal engine and an electric motor, and to convert these to low speeds and high torques to output available to the propeller. Furthermore, the gearbox will see different levels of power depending on different flight conditions (taxi-in, take-off, climb, cruise, descent and taxi-out) and, of all these conditions, the first sizing of the gearbox will be in hybrid take-off mode, namely the max of power of both engines (after to chose the layout of the gearbox itself).

When the gearbox layout will be fixed and it will be known the geometry, then we will focus on the work profiles of the gearbox depending on the flight phase for dynamic analysis.

1.3 Power Density Engine

In this chapter, the first and the second formulas, NASA '15 and WATE 2, will be analysed (Tab 1.1), to estimate the gearbox mass for different models of engines (Tab 1.2), most of them will be turboprop and only a few turboshafts. And, in the end, it will bring back the power density of all models analyzed by NASA'15 formula figure 1.1.

Model	Reference	Constructor	Type
PW100	[15]	Pratt Whitney	Turboprop
PT-6A 60 Series 2	[16]	Pratt Whitney	Turboprop
PT-6T Series 3	[17]	Pratt Whitney	Turboshaft
PW 200	[18]	Pratt Whitney	Turboshaft
PW210	[19]	Pratt Whitney	Turboshaft
AE2100 Series	[20]	Rolls Royce	Turboprop
M250	[21]	Rolls Royce	Turboprop
CT7	[22]	GE Aviation	Turboprop/shaft
H80	[23]	GE Aviation	Turboprop
M600	[23]	GE Aviation	Turboprop
GE Catalyst	[24]	GE Aviation	Turboprop
Honeywell TPE331	[25]	Honeywell Aerospace	Turboprop Gearbox

Table 1.2: Aircrafts Analyzed

All datasheets for all models are taken from EASA.

The first formula (1.1) or (1.2), NASA '15 [10], takes into input the number of rotors, the rotational high-speed shaft in RPM, the power in kW and the rotational low-speed shaft, which in this case is the propeller speed, always in RPM.

This is a formula based on the empirical data analysis of 52 rotorcraft.

From this estimation, the mean average percentage error (MAPE) is 8.6%. Add to this the method includes the gearbox accessories. This formula has been readapted to aircraft setting into it the number of the rotor equal to one.

$$m_{GB[kg]} = 54.6311 \cdot N_{rotors[-]}^{0.38553} \cdot P_{MaxContinuos[kW]}^{0.78137} \cdot \frac{\omega_{engine[RPM]}^{0.09899}}{\omega_{propeller[RPM]}^{0.80686}} \tag{1.1}$$

$$m_{GB[kg]} = 54.6311 \cdot P_{MaxContinuos[kW]}^{0.78137} \cdot \frac{\omega_{engine[RPM]}^{0.09899}}{\omega_{propeller[RPM]}^{0.80686}} \tag{1.2}$$

However, the second formula, WATE 2 [11], takes input torque and gear ratio. It is used to inline gearbox and powers between 1000 hp (745kW) to 2500 hp (1864 kW) shaft horsepower.

There is no mention of gearbox accessories or the nature of the empirical data source.

$$m_{GB[kg]} = 0.453592 \cdot (0.0174Q_{[lb \cdot ft]} + 45) \cdot \sqrt{0.118 \cdot \frac{\omega_{eng[RPM]}}{\omega_{prop[RPM]}}} \tag{1.3}$$

Finally, the last set of equations (1.4), (1.5) and (1.6), Willis 1963 [12], calculates the mass assuming that it is proportional to the volume of the gears

$$N_{pl} = \frac{16.3677}{3asin\frac{GR-1}{GR+1}1.1736} \tag{1.4}$$

$$2GR_s^3 + GR_s^2 = \frac{0.4GR^2+1}{N_{pl}} \tag{1.5}$$

$$m_{gb,[kg]} = 0.2268\frac{Q}{K\omega_{eng}} \cdot \left(\frac{1}{N_{pl}} + \frac{1}{N_{pl}GR_s} + GR_z + GR_z^2 + \frac{0.4GR^2}{N_{pl}GR_s}\right) \tag{1.6}$$

A mention shall be made with respect to the last two formulae given in Table 1.1. The first formula [13] can estimate the internal combustion engine mass, while the second [14] gives a power density comparable [10], but higher.

However, of all of this, it is reported only Nasa 15 gave the same gearbox power density as one turboprop constructor [26].

Model [−]	Power [kW]	ω_{prop} [RPM]	m_{GB} [kg]	Q [Nm]	Pd_{engine} [kW/kg]	Pd_{GT} [kW/kg]	Pd_{GB} [kW/kg]	Qd [Nm/kg]	%GB [kg]
PW118	1342	1313	124.5	9760.2	3.44	5.04	10.78	24.99	31.87%
PW118A	1342	1313	124.5	9760.2	3.42	5.00	10.78	24.85	31.68%
PW119B	1625	1339	142.5	11589.0	3.95	6.04	11.40	28.17	34.65%
PW119C	1625	1339	142.5	11589.0	3.95	6.04	11.40	28.17	34.65%
PW120	1491	1212	143.0	11747.5	3.57	5.44	10.43	28.15	34.27%
PW120A	1491	1212	143.0	11747.5	3.52	5.32	10.43	27.76	33.79%
PW121	1603	1212	151.3	12630.0	3.79	5.90	10.59	29.84	35.76%
PW121A	1640	1212	154.1	12921.5	3.78	5.86	10.65	29.77	35.50%
PW123	1775	1212	163.9	13985.1	3.94	6.20	10.83	31.08	36.42%
PW123AF	1775	1212	163.9	13985.1	3.94	6.20	10.83	31.08	36.42%
PW123B	1865	1212	170.3	14694.3	4.14	6.67	10.95	32.65	37.85%
PW123C	1604	1212	151.4	12637.8	3.56	5.37	10.59	28.08	33.64%
PW123D	1604	1212	151.4	12637.8	3.56	5.37	10.59	28.08	33.64%
PW123E	1775	1212	163.9	13985.1	3.94	6.20	10.83	31.08	36.42%
PW124B	1790	1212	165.0	14103.3	3.72	5.67	10.85	29.33	34.31%
PW125B	1864	1212	170.3	14686.4	3.88	6.00	10.95	30.55	35.41%
PW126	1978	1212	178.3	15584.6	4.11	6.54	11.09	32.41	37.09%
PW126A	1985	1212	178.8	15639.7	4.13	6.57	11.10	32.53	37.20%
PW127	2051	1212	183.5	16159.7	4.27	6.90	11.18	33.61	38.16%
PW127B	2051	1212	183.5	16159.7	4.27	6.90	11.18	33.61	38.16%
PW127D	2051	1212	183.5	16159.7	4.27	6.90	11.18	33.61	38.16%
PW127E	1790	1212	165.0	14103.3	3.72	5.67	10.85	29.33	34.31%
PW127F	2051	1212	183.5	16159.7	4.27	6.90	11.18	33.61	38.16%
PW127G	2178	1212	192.3	17160.4	4.50	7.46	11.33	35.43	39.69%
PW127M	2051	1212	183.5	16159.7	4.26	6.88	11.18	33.55	38.09%
PW127N	2051	1212	183.5	16159.7	4.26	6.88	11.18	33.55	38.09%
PW127XT-M	2051	1212	183.5	16159.7	4.15	6.59	11.18	32.67	37.09%
PW150A	3781	1020	334.3	35397.9	5.27	9.88	11.31	49.38	46.63%

Table 1.3: PW100 Turboprop [15]

Model $[-]$	Power $[kW]$	ω_{prop} $[RPM]$	m_{GB} $[kg]$	Q $[Nm]$	Pd_{engine} $[kW/kg]$	Pd_{GT} $[kW/kg]$	Pd_{GB} $[kW/kg]$	Qd $[Nm/kg]$	%GB $[kg]$
PT-6A-65B	820.3	1700	70.9	4608	3.7	5.3	11.6	20.5	31.6%
PT-6A-65AR	1061.9	1700	86.8	5965	4.7	7.6	12.2	26.2	38.2%
PT-6A-65AG	969.4	1700	80.8	5445	4.3	6.6	12.0	24.0	35.6%
PT-6A-67A	894.8	1700	75.9	5027	3.8	5.6	11.8	21.3	32.2%
PT-6A-67P	894.8	1700	75.9	5027	3.6	5.2	11.8	20.1	30.4%
PT-6A-67B	894.8	1700	75.9	5027	3.7	5.3	11.8	20.6	31.1%
PT-6A-67R-T	1061.9	1700	86.8	5965	4.4	6.8	12.2	24.6	35.8%
PT-6A-67D	953.8	1700	79.8	5357	3.9	5.9	12.0	22.1	32.9%
PT-6A-67F	1193.1	1700	95.1	6702	4.8	7.7	12.6	26.9	38.1%
PT-6A-67AG	1006.7	1700	83.2	5655	4.2	6.5	12.1	23.7	35.0%
PT-6A-67AF	1061.9	1700	86.8	5965	4.2	6.5	12.2	23.8	34.7%
PT-6A-60A	783.0	1700	68.4	4398	3.6	5.3	11.4	20.4	31.7%
PT-6A-60AG	783.0	1700	68.4	4398	3.5	4.9	11.4	19.4	30.2%

Table 1.4: PT-6A-60 Series 2 Turboprop [16]

Model $[-]$	Power $[kW]$	ω_{prop} $[RPM]$	m_{GB} $[kg]$	Q $[Nm]$	Pd_{engine} $[kW/kg]$	Pd_{GT} $[kW/kg]$	Pd_{GB} $[kW/kg]$	Qd $[Nm/kg]$	%GB $[kg]$
PT6T-3	1342.3	6600.0	35.2	1942	4.3	4.8	38.1	6.2	11.3%
PT6T-3B	1342.3	6600.0	35.2	1942	4.3	4.8	38.1	6.2	11.3%
PT6T-3BF	1342.3	6600.0	35.2	1942	4.3	4.8	38.1	6.2	11.3%
PT6T-3BE	1342.3	6600.0	35.2	1942	4.3	4.8	38.1	6.2	11.3%
PT6T-3BG	1342.3	6600.0	35.2	1942	4.3	4.8	38.1	6.2	11.3%
PT6T-3D	1342.3	6600.0	35.2	1942	4.3	4.8	38.1	6.2	11.3%
PT6T-3DE	1342.3	6600.0	35.2	1942	4.3	4.8	38.1	6.2	11.3%
PT6T-3DF	1342.3	6600.0	35.2	1942	4.3	4.8	38.1	6.2	11.3%

Table 1.5: PT-6T-3 Series 3 Turboshaft [17]

Model $[-]$	Power $[kW]$	ω_{prop} $[RPM]$	m_{GB} $[kg]$	Q $[Nm]$	Pd_{engine} $[kW/kg]$	Pd_{GT} $[kW/kg]$	Pd_{GB} $[kW/kg]$	Qd $[Nm/kg]$	%GB $[kg]$
PW210S	559	6409	17.9	832.9	3.4	3.9	31.2	5.1	11.0%
PW210A	615	14832	9.8	395.9	3.8	4.1	62.7	2.5	6.1%
PW210A1	615	14832	9.8	395.9	3.8	4.1	62.7	2.5	6.1%

Table 1.6: PW 210 Turboshaft [19]

Model $[-]$	Power $[kW]$	ω_{prop} $[RPM]$	m_{GB} $[kg]$	Q $[Nm]$	Pd_{engine} $[kW/kg]$	Pd_{GT} $[kW/kg]$	Pd_{GB} $[kW/kg]$	Qd $[Nm/kg]$	%GB $[kg]$
PW206A	410	6240	14.9	627.4	3.8	4.4	27.5	5.8	13.9%
PW206B	321	6134	12.5	499.7	2.7	3.0	25.7	4.2	10.5%
PW206B2	321	6134	12.5	499.7	2.7	3.1	25.7	4.3	10.6%
PW206B3	324	6193	12.5	499.6	2.8	3.1	26.0	4.3	10.7%
PW206C	418	6120	15.4	652.2	3.9	4.5	27.2	6.1	14.3%
PW206E	426	6240	15.4	651.9	3.7	4.3	27.7	5.7	13.5%
PW207C	426	6120	15.6	664.7	3.7	4.3	27.3	5.8	13.7%
PW207D	426	6240	15.4	651.9	3.7	4.3	27.7	5.7	13.5%
PW207D1	455	6240	16.2	696.3	4.1	4.8	28.1	6.3	14.6%
PW207D2	455	6240	16.2	696.3	4.0	4.7	28.1	6.2	14.4%
PW207E	426	6240	15.4	651.9	3.7	4.3	27.7	5.7	13.5%
PW207K	429	6240	15.5	656.5	3.7	4.3	27.8	5.7	13.5%

Table 1.7: PW 200 Turboshaft [18]

Model $[-]$	Power $[kW]$	ω_{prop} $[RPM]$	m_{GB} $[kg]$	Q $[Nm]$	Pd_{engine} $[kW/kg]$	Pd_{GT} $[kW/kg]$	Pd_{GB} $[kW/kg]$	Qd $[Nm/kg]$	%GB $[kg]$
AE 2100A	2787.0	1100.0	245.4	24194.4	3.8	5.7	11.4	32.8	33.3%
AE 2100D2	3458.0	1020.7	306.2	32351.8	4.3	6.9	11.3	40.2	38.0%
AE 2100D2A	3458.0	1020.7	306.2	32351.8	4.3	6.9	11.3	40.2	38.0%

Table 1.8: AE 2100 Series Turboprop [20]

Model $[-]$	Power $[kW]$	ω_{prop} $[RPM]$	m_{GB} $[kg]$	Q $[Nm]$	Pd_{engine} $[kW/kg]$	Pd_{GT} $[kW/kg]$	Pd_{GB} $[kW/kg]$	Qd $[Nm/kg]$	%GB $[kg]$
B15A	201.0	2025.0	20.8	947.9	3.1	4.7	9.6	14.8	32.6%
B15G	201.0	2025.0	20.8	947.9	3.1	4.7	9.6	14.8	32.6%
B17	287.0	2030.0	27.3	1350.1	4.0	6.5	10.5	18.8	38.1%
B17B	313.0	2030.0	29.3	1472.4	4.4	7.4	10.7	20.5	40.8%
B17C	287.0	2030.0	27.3	1350.1	4.0	6.5	10.5	18.8	38.1%
B17D 23005700	287.0	2030.0	27.3	1350.1	3.2	4.6	10.5	15.0	30.5%
B17D 23051125	287.0	2030.0	27.3	1350.1	3.2	4.6	10.5	15.0	30.5%
B17E	313.2	2030.0	29.3	1473.3	3.4	5.0	10.7	16.1	32.0%
B17F	313.2	2030.0	29.3	1473.3	3.3	4.7	10.7	15.3	30.4%
B17F/1	335.6	2030.0	30.9	1578.5	3.4	5.0	10.9	16.2	31.7%
B17F/2	335.6	2030.0	30.9	1578.5	3.5	5.1	10.9	16.4	32.1%

Table 1.9: M250 Turboprop [21]

Model $[-]$	Power $[kW]$	ω_{prop} $[RPM]$	m_{GB} $[kg]$	Q $[Nm]$	Pd_{engine} $[kW/kg]$	Pd_{GT} $[kW/kg]$	Pd_{GB} $[kW/kg]$	Qd $[Nm/kg]$	%GB $[kg]$
CT7-5A2	889.6	1,384	86.5	6138.2	2.5	3.3	10.3	17.3	24.4%
CT7-7A	945.5	1,384	90.8	6524.1	2.7	3.6	10.4	18.4	25.6%
CT7-9B	973.1	1,384	92.8	6714.4	2.7	3.6	10.5	18.4	25.4%
CT7-9C	973.1	1,384	92.8	6714.4	2.7	3.6	10.5	18.4	25.4%
CT7-9C3	973.1	1,384	92.8	6714.4	2.7	3.6	10.5	18.3	25.4%

Table 1.10: CT7 Turboprop [22]

Model $[-]$	Power $[kW]$	ω_{prop} $[RPM]$	m_{GB} $[kg]$	Q $[Nm]$	Pd_{engine} $[kW/kg]$	Pd_{GT} $[kW/kg]$	Pd_{GB} $[kW/kg]$	Qd $[Nm/kg]$	%GB $[kg]$
CT7-2A	886.6	1,384	86.0	6117.6	4.6	8.2	10.3	31.4	44.2%
CT7-2E1	1040.3	1,384	97.4	7177.5	4.7	8.3	10.7	32.2	43.8%
CT7-2F1	952.3	1,384	90.9	6570.4	4.4	7.5	10.5	30.1	41.6%
CT7-6	955.2	1,384	91.2	6591.0	4.3	7.2	10.5	29.5	40.8%
CT7-6A	955.2	1,384	91.2	6591.0	4.3	7.2	10.5	29.5	40.8%
CT7-8	1136.0	1,384	104.4	7838.5	4.7	8.2	10.9	32.2	42.9%
CT7-8A	1136.0	1,384	104.4	7838.5	4.6	8.0	10.9	31.9	42.5%
CT7-8A5	1199.4	1,384	108.9	8275.9	4.9	8.8	11.0	33.7	44.3%
CT7-8A6	1295.1	1,384	115.6	8935.8	5.3	9.9	11.2	36.3	47.0%
CT7-8B	1134.9	1,384	104.3	7830.8	4.6	8.0	10.9	31.8	42.4%
CT7-8B5	1197.8	1,384	108.8	8264.4	4.9	8.7	11.0	33.6	44.2%
CT7-8E	1134.9	1,384	104.3	7830.8	4.6	8.0	10.9	31.8	42.4%
CT7-8E5	1197.8	1,384	108.8	8264.4	4.9	8.7	11.0	33.6	44.2%
CT7-8F	1089.9	1,384	101.1	7520.0	4.4	7.5	10.8	30.6	41.1%
CT7-8F5	1196.1	1,384	108.7	8252.8	4.9	8.7	11.0	33.6	44.2%

Table 1.11: CT7 Turboshaft [22]

Model $[-]$	Power $[kW]$	ω_{prop} $[RPM]$	m_{GB} $[kg]$	Q $[Nm]$	Pd_{engine} $[kW/kg]$	Pd_{GT} $[kW/kg]$	Pd_{GB} $[kW/kg]$	Qd $[Nm/kg]$	%GB $[kg]$
H80-100	597.0	2080.0	47.2	2740.8	3.0	3.9	12.6	13.7	23.6%
H75-100	560.0	2080.0	44.9	2571.0	2.8	3.6	12.5	12.9	22.4%
H85-100	634.0	2080.0	49.5	2910.7	3.2	4.2	12.8	14.6	24.7%
H80	597.0	2080.0	47.2	2740.8	3.0	3.9	12.6	13.6	23.4%
H80-200	522.0	2080.0	42.5	2396.5	2.6	3.3	12.3	11.9	21.0%
H75-200	560.0	2080.0	44.9	2571.0	2.8	3.6	12.5	12.7	22.2%
H85-200	634.0	1950.0	52.1	3104.7	3.1	4.2	12.2	15.4	25.8%

Table 1.12: H80 Turboprop [23]

Model [−]	Power [kW]	ω_{prop} [RPM]	m_{GB} [kg]	Q [Nm]	Pd_{engine} [kW/kg]	Pd_{GT} [kW/kg]	Pd_{GB} [kW/kg]	Qd [Nm/kg]	%GB [kg]
M601D	490.0	2080.0	40.4	2249.6	2.5	3.1	12.1	11.4	20.5%
M601D-1	490.0	2080.0	40.4	2249.6	2.5	3.1	12.1	11.4	20.5%
M601D-2	400.0	1950.0	36.4	1958.8	2.0	2.5	11.0	9.9	18.5%
M601E	490.0	2080.0	40.4	2249.6	2.4	2.9	12.1	10.9	19.5%
M601E-21	490.0	2080.0	40.4	2249.6	2.4	2.9	12.1	10.9	19.5%
M601F	500.0	2080.0	41.1	2295.5	2.4	3.0	12.2	11.1	19.9%
M601E-11AS	485.0	2080.0	40.1	2226.6	2.3	2.9	12.1	10.8	19.4%
M601FS	500.0	2080.0	41.1	2295.5	2.4	3.0	12.2	11.1	19.9%
M601D-11	450.0	1950.0	39.9	2203.7	2.2	2.7	11.3	10.8	19.5%
M601D-11NZ	320.0	1950.0	30.5	1567.1	1.6	1.8	10.5	7.7	15.0%
M601Z	245.0	1900.0	25.3	1231.4	1.2	1.4	9.7	6.1	12.6%
M601E-11S	490.0	2080.0	40.4	2249.6	2.3	2.9	12.1	10.6	19.1%
M601E-11AS	490.0	2080.0	40.4	2249.6	2.3	2.9	12.1	10.6	19.1%
M601FS	485.0	2080.0	40.1	2226.6	2.3	2.8	12.1	10.5	18.9%

Table 1.13: M600 Turboprop [23]

Model [−]	Power [kW]	ω_{prop} [RPM]	m_{GB} [kg]	Q [Nm]	Pd_{engine} [kW/kg]	Pd_{GT} [kW/kg]	Pd_{GB} [kW/kg]	Qd [Nm/kg]	%GB [kg]
GE Catalyst	1190.0	2000.0	83.9	5681.8	4.2	6.0	14.2	20.1	29.7%

Table 1.14: GE Catalyst Turboprop [24]

Model [−]	Power [kW]	ω_{prop} [RPM]	m_{GB} [kg]	Q [Nm]	Pd_{engine} [kW/kg]	Pd_{GT} [kW/kg]	Pd_{GB} [kW/kg]	Qd [Nm/kg]	%GB [kg]
TPE331	760.6	2000.0	51.8	3631.7	—	—	—	4.36	14.7%

Table 1.15: TPE 331 Honeywell Turboprop [25]

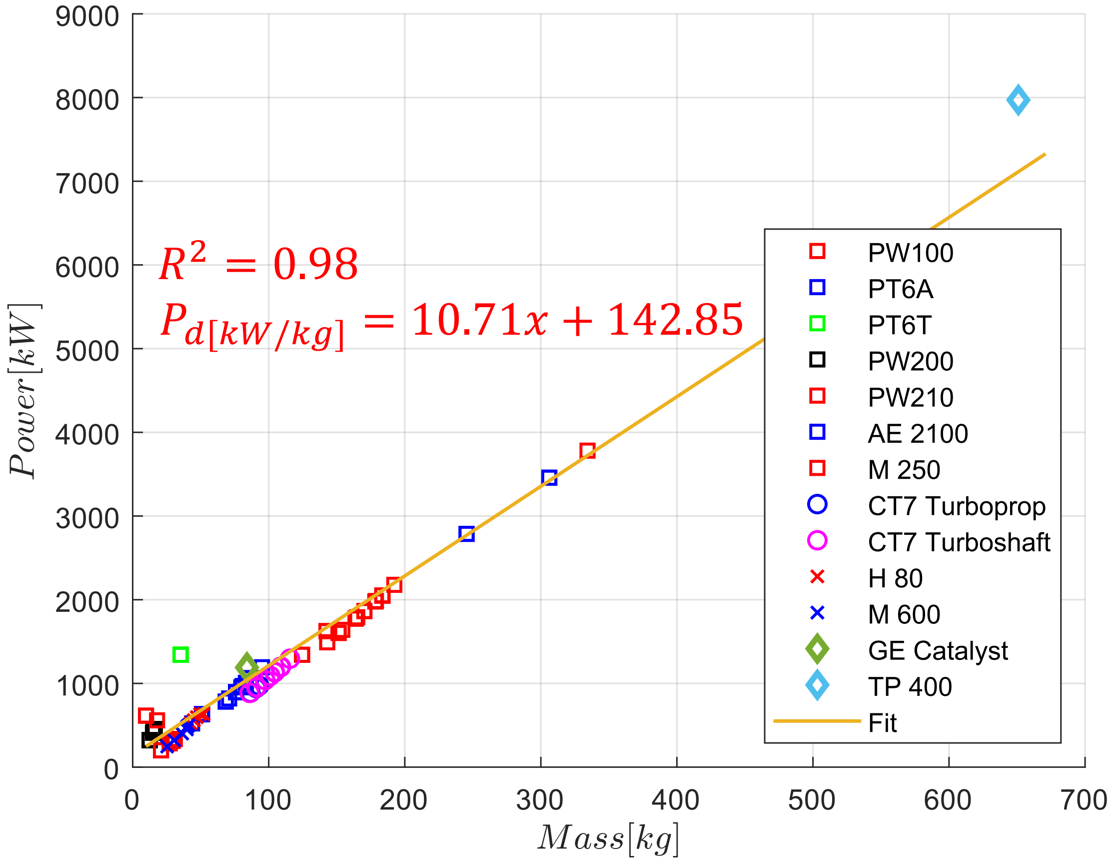

Figure 1.1: Power Density: All Models

The power density of the PW 100 series is between 10 and 11.5 kW/kg and it's confrontable whit the Roll Royce Turboprop M250 series. Also, the percentage weight of these GB is confrontable. From the only point of view of the installed power, without comparing the type of layout, these models are equivalent (whit differences in the production house).

If it compares the torque density the PW100 is higher than M250. So, with the same mass for both systems, the PW100 produces more torque.

Other information can be individuated from PT6A 60 Series 2 and PT6T Series 3.

The PT6T Series 3 is the engine whit the maximum of power density and lower torque density of all models in the tables. So, since the gearbox sizing depends on the torque and doesn't on the power, that means that these models have the smallest gearbox than other models. This makes sense because these are turboshafts, in which there are lower transmission ratios and consequently higher rotor speeds compared to a propeller.

In addition, with around 1 MW of power, the PT6A 60 Series 2 has an interesting torque density to give at the propeller whit a weight of the system weight not too high. This is possible for the layout type: epicycloidal gearbox.

In conclusion, a similar analysis can be done for all combinations of all models indicated. For instance, in figure 1.1 there is all power and mass estimated by NASA'15 (1.2) and a fit which represent the power density trend of all models.

Also, if there are no design indications to adopt a parallel shaft to the first stage and a different layout for the second stage, then the in-line architecture transmission, whit a planetary gearbox, is the best solution. However, if there were to be different design indications, then other solutions will be considered.

Chapter 2

Gearbox Sizing

In this chapter, the aeronautical gearboxes will be analysed, the typical architecture and how these work, and the logic flux that will be used to size them.

As mentioned above, some of the possible solutions and those most proven in aerospace will be analysed.

So the typical architectures are:

- Off-set architecture whit parallel shaft;
- In-line architecture with a planetary transmission;
- Mixed architecture, an architecture which uses both parallel shaft and planetary gears;

All of these transmissions have the same goals: to take the high power and low torque from the input shaft, linked to a thermal engine, and transmit it to the output shaft, linked to the propeller, whit the same power, unless losses, but increase the torque. In these cases, the thermal engine is equal to all three configurations, namely a gas turbine (GT) generally called a power turbine in the literature.

2.1 General Architecture Definition

In the first architecture, the offset layout is adopted by Pratt Whitney in series 100, in Figure 2.1 and 2.2. In this case, the power range is between 2 MW and 3.7 MW, a propeller speed between 1020 RPM and 1339 RPM and a gear ratio of 16.67 between the input shaft, power turbine shaft, and propeller shaft (Tab. 1.3).

This configuration uses a double reduction stage. In the first stage of reduction, the two-helical pinion with opposing propellers (1 and 1a) engage whit helical gears $2 - 2_a - 3$ and 3_a and, in the second stage of reduction, the pinions 6 and 4 mesh with the helical crown 5.

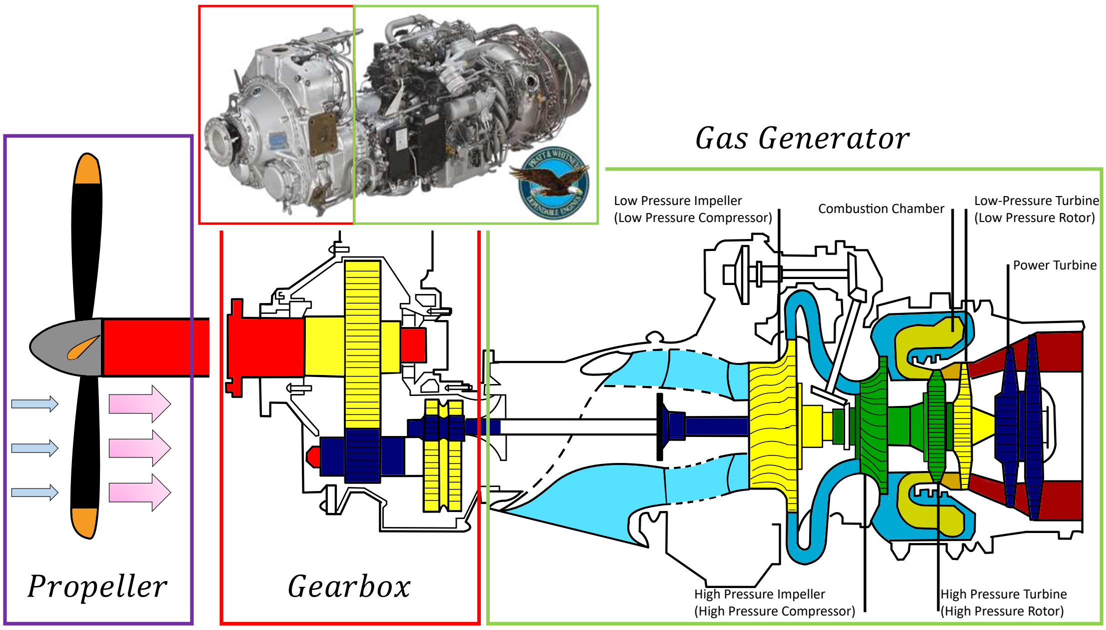

Figure 2.1: Pratt Whitney PW100: Off-Set Architecture

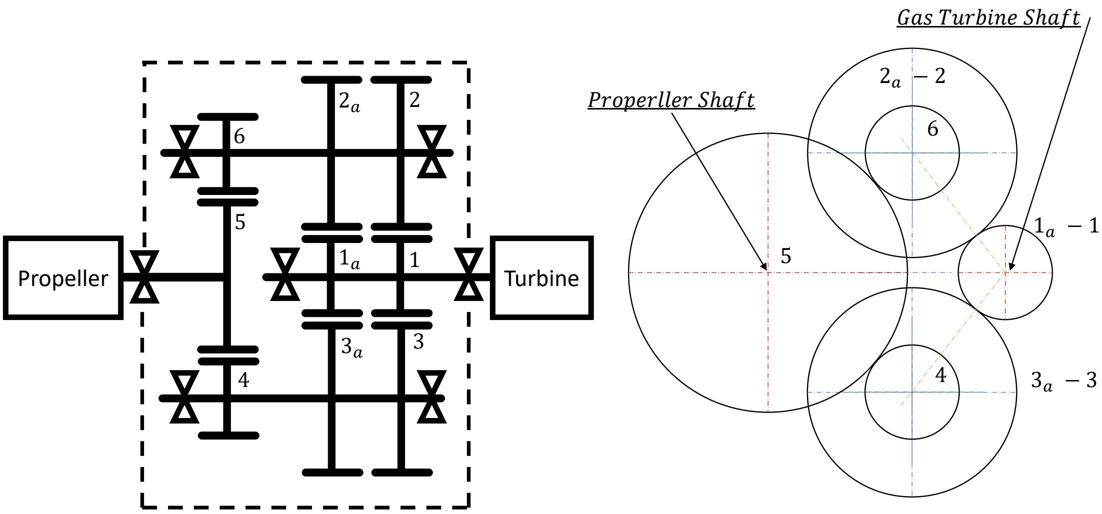

Figure 2.2: Pratt Whitney PW100: Off-Set Architecture in Top view

This layout uses the pinions whit opposing propellers for two aims: first to eliminate the axial force on the bearings and therefore on housing, and after to divide equally the power between shafts.

This layout has some vantages and disadvantages:

- Is simple to size in conventional propulsion and it's simple to re-use and to re-adapt in a hybrid gearbox (see later);
- Is perfectly balanced from powers and torques point of view;
- Must use lightened wheels to not compromise the total weight of the transmission for high torques;
- Is not the smallest and most compact solution possible;

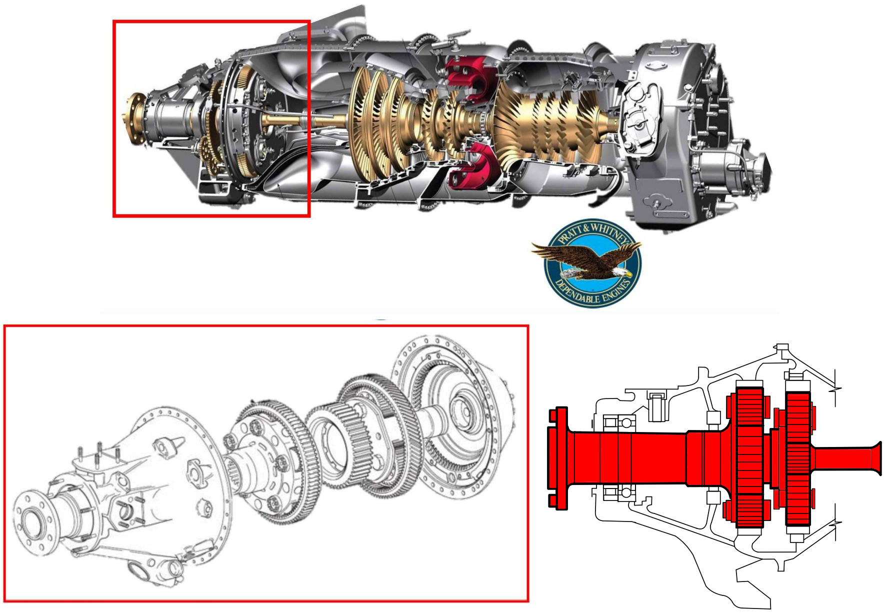

Figure 2.3: Pratt Whitney PT 6A Series 2: In-Line Architecture

The second layout is also adopted by Pratt Whitney in PT 6A Seris 2 as in-line architecture Figure 2.3 and 2.4. In this case, the power range is between 400 kW and 1.4 MW, a propeller speed between 1500 RPM and 1700 RPM and a gear ratio of 17.67 or 15.67 between the input shaft, power turbine shaft, and propeller shaft (Tab. 1.4).

In this case, there is a central gear, known as the sun gear, surrounded by multiple smaller gears, known as planet gears, which are in turn enclosed within an outer ring gear, also called the annular gear or ring gear.

The planetary gears are mounted on a carrier that rotates around the sun gear. The carrier is typically connected to the output shaft, while the sun gear is connected to the input shaft. The ring gear remains stationary or acts as the output shaft, depending on the specific design.

The key characteristic of the epicyclic gearbox is the motion of the planet's gears. As the carrier rotates, the planet gears rotate both around their own axes and also revolve around the sun gear. This combination of rotation and revolution creates an interesting gear motion, resulting in different gear ratios and torque outputs.

If you write the gear ratio you can see there are infinite to 1 solutions, because the gear ratio of the epicyclic gearbox can be known by fixing any two of the three components: sun gear, planet gears, or ring gear, while allowing the other component to act as the input or output. By controlling the engagement and locking of these gears, different gear ratios can be achieved, providing various speed reduction or increase options.

In the scheme of Figure 2.4 you can see that:

- there are two stages in line of two planetary gearboxes;
- there is a different number of planets between the first and second stages;

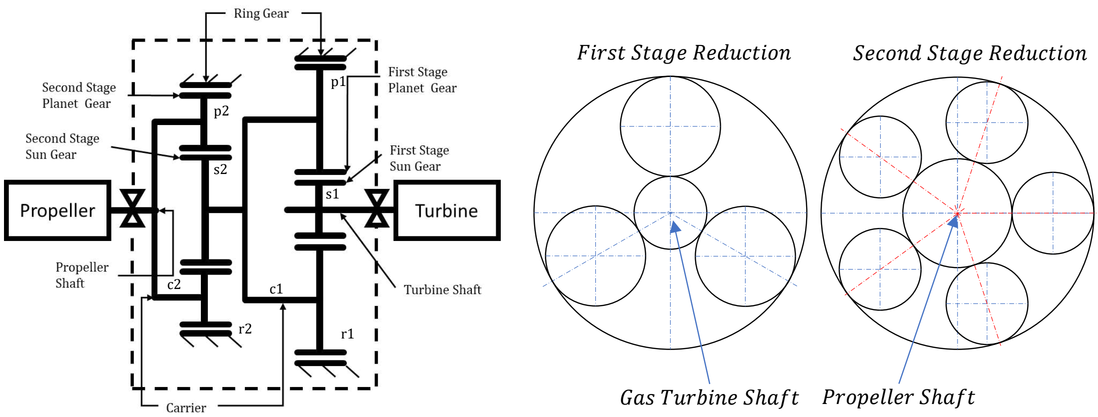

Figure 2.4: Pratt Whitney PT 6A Series 2: In-Line Architecture

This is adopted because two planetary gearboxes in a series can give a higher gear ratio than only one and usually the number of planets increases from the first to the second stage due to a growing torque. In addition the scheme of Figure 2.4 represent the condition in which the ring of the first and of the second stage are blocked. As the last point, this transmission can be built with helical or spur gears. The analysis of several studies about helical gears [27] [28] [29] and spur gears [30] has shown how the spur gears are the ideal choice if the purpose is to maximize the torque density and working life under higher loads the spur gears and how helical gears are preferred if you are looking for smoother and less noisy transmissions. For this reason, in the in-line architecture, you choose a spur gear.

In summary, this type of transmission offers several advantages:

- compact size whit high power density for spur gears;
- no axial force on bearing and housing;
- high working life under high loads;
- the ability to handle high torque loads;
- gear ratio greater than other architecture of equal weight;
- they must have co-axial shafts;

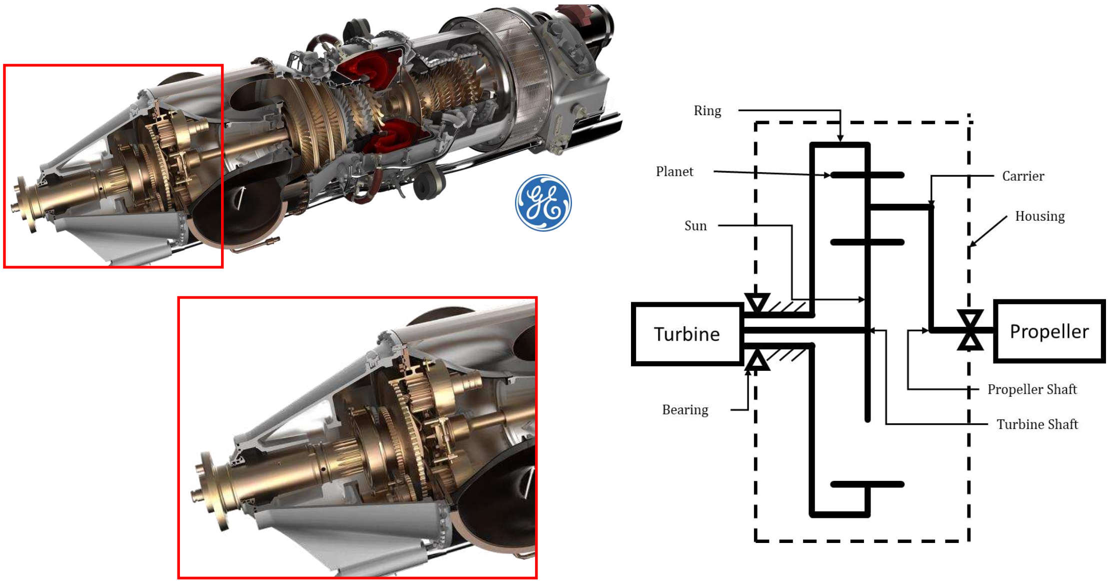

Figure 2.5: General Electric Catalyst

This architecture is also used by General ELectric in the Catalyst model Figure 2.5. However in this case there is only one stage of planetary transmission, then lighter than the previous layout if they both had the same power.

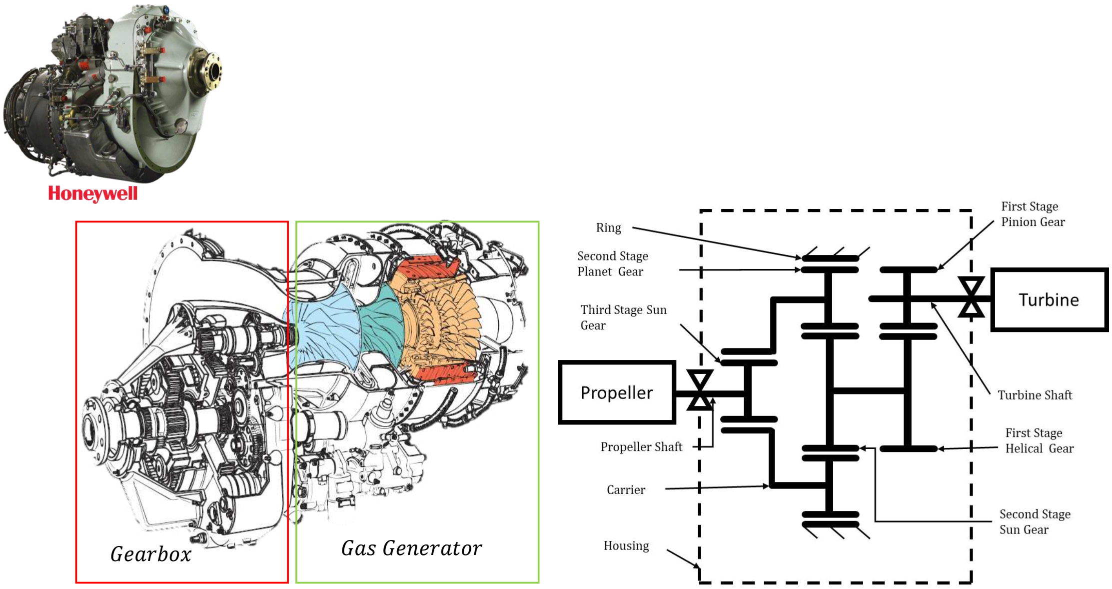

Figure 2.6: Honeywell TPE 331

In conclusion about the analyzed layouts, the end is a mixed architecture of Honeywell TPE331 Figure 2.6. This gearbox uses a power range between 300 kW and 900 kW whit a parallel shaft in the first stage and planetary transmission for the second end stages. This architecture is used when the gear ratio is higher, plus 20, and there is a design specification of don't to have a co-axial shaft in the first stage.

2.2 Hybrid Architecture Definition

This section aims to identify how it is possible to go from a conventional propulsion layout with a single input shaft to a parallel hybrid layout with two input shafts. Then understand how you change the flow of power to vary the type of layout adopted and as a result, how to change the gearbox sizing.

Another point to add to the discussion is the topology of Electric Motor. It can be essentially of two types:

- typology of flux: axial or radial
- range of rotational speed
- depending on the last two points the mass/volume and the weight of the electric system

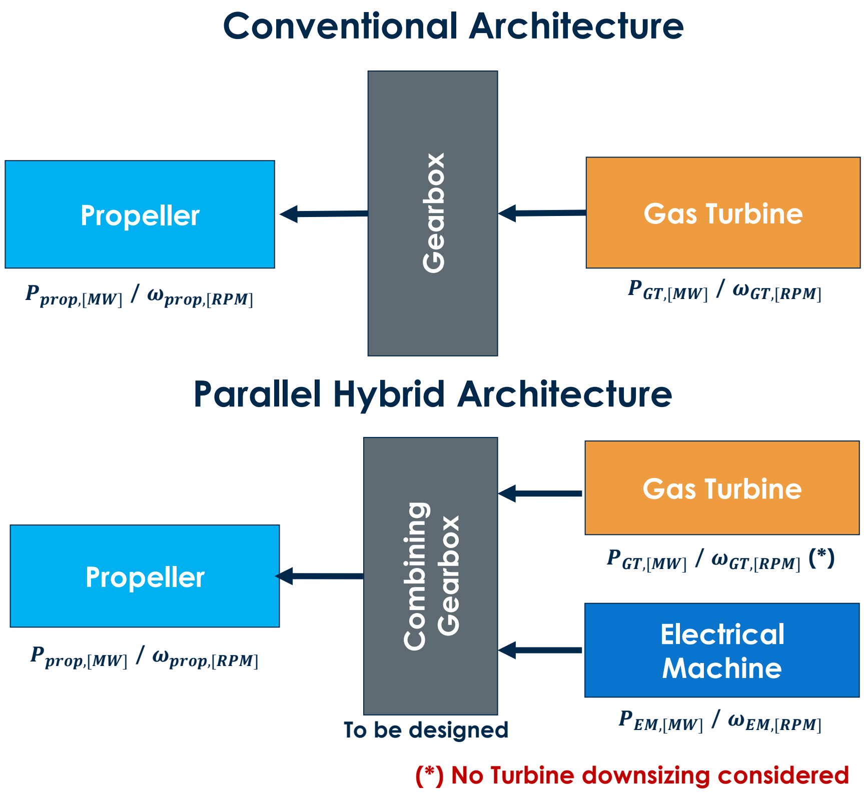

Figure 2.7: Gearbox and Combined Gearbox

In general, a radial flux electric motor has a higher speed, a lower torque, a higher power density and a higher efficiency 0.98 than an axial flux machine and it adopts a long and slender shaft. So this machine results lighter than axial flux. In opposite to this the axial flux has a lower speed, a higher torque than radial flux and a squat shaft. In this case, it is heavier than radial flux.

In conclusion, in Figure 2.8, there are two goals to reach at the same time: identify the best solution with the best type of Electric Motor to minimize the mass and so the weight of all systems.

Also, in the Figure 2.7 is indicated how the Gas Turbine has not been downsized because it is hypothesized to do a conventional take-off if the battery storage is discharged or the aircraft is climbed, in a flight phase of the mission, without the power of the battery and so only with gas turbine power.

If it takes Figure 2.2 as a reference it is possible to obtain three different layouts of the combined gearbox represented in Figure 2.9.

In detail, in Off-Set H1 used a high-speed EM, ideally the same as GT, and all EM power is discharged in the first pinion of the first reduction stage. Also, the power of GT and the power of EM are equally divided between the gears of the

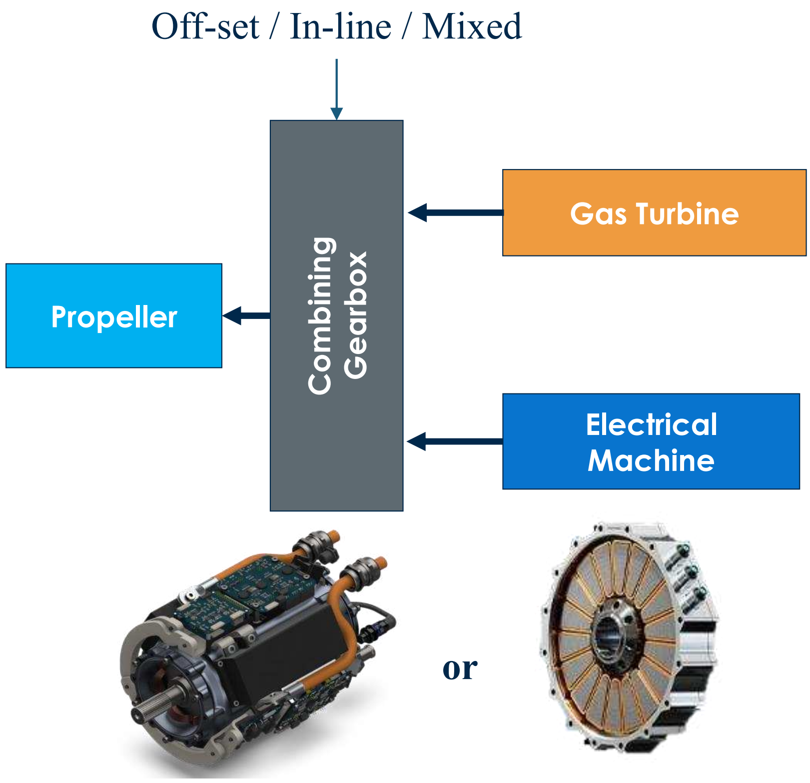

Figure 2.8: Type Electric Motor

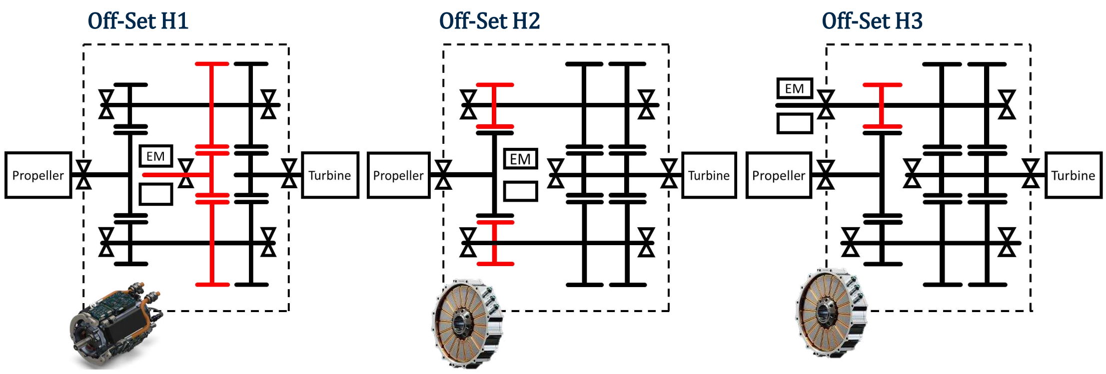

Figure 2.9: Combined Gearbox in Off-Set Layout

first stage and each meshing sees a 50% percentage of power or torque, in this case.

However, the second stage of reduction doesn't see any difference from conventional propulsion in terms of torque and power.

In the detail of Off-Set H2, in Figure 2.2, is used a low-speed EM is added a

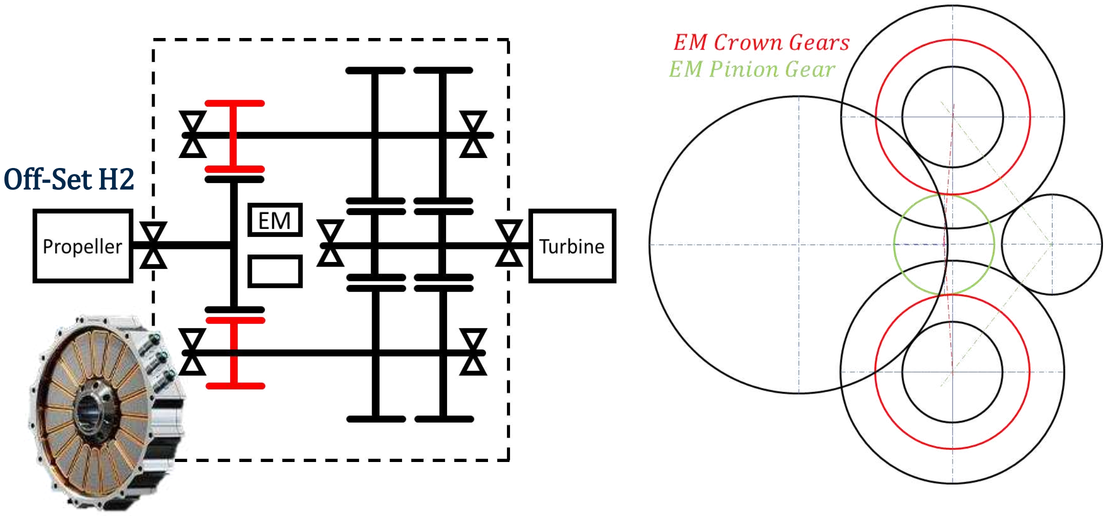

Figure 2.10: Combined Gearbox Off-Set H2

pinion to EM. In this instance, the torque of EM is discharged in two meshing of the second stage of reduction and after to the crown gear linked to the propeller shaft. It is also possible a direct meshing between the pinion gear of EM and the crown gear of the propeller shaft, but in doing so the EM torque would discharge in only one teeth contact so a higher module respect at the solution proposed. The first stage instead doesn't see any difference from conventional propulsion, in which the all power of GT is discharged in two pinion and four crown gears. In this way each meshing sees a 25% of the total torque of the GT.

In the end, Off-Set H3 always in Figure 2.9, it is another possible solution where collocate the EM in the combined gearbox. But, this layout is not used for two reasons: an imbalanced system from a torque point of view (too much torque discharged in a single meshing whit too high a module) and a difficult positioning of EM near the propeller shaft (stretch the propeller shaft to make room).

With regard to the in-line configuration in Figure 2.11, there are some points to define: first the two possible layouts and depending on them the electric motor speed to use.

The first possible solution, named "Hybrid 1", is to add a pinion and a crown gear of electric motor axes and gas turbine axes and, in this way theoretically, is possible to use whatever range of speed of the EM. The advantage is that the speed of the EM and the speed of the GT are not correlated because it uses the gear ratio of pinion and crown gear added. In fact, in the picture is represented with a high-speed EM.

Despite this, to not have too big gears to link the shaft of EM with the gas turbine shaft, it will use a minimum speed of EM equal to 4000 RPM.

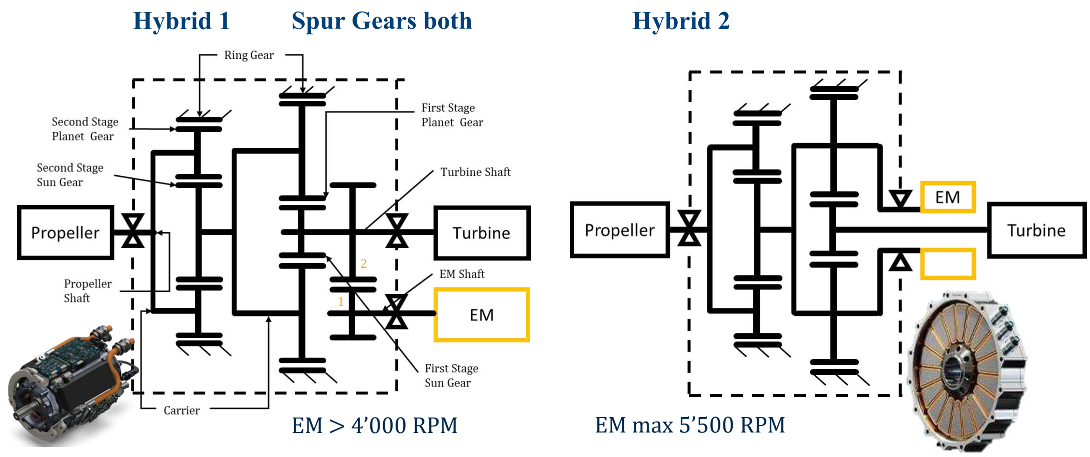

Figure 2.11: In-Line Hybrid Architecture

However, the disadvantage is adding other weight and an unbalanced system.

The second possible solution, named "Hybrid 2" always in Figure 2.11, and it has some advantages: this scheme doesn't add any gears and so no other weight; the link between EM, Gearbox and Gas Turbine is done by the carrier; the volume of all system is similar to conventional propulsion; the EM shaft and the GT shaft are coaxial and then they don't add bearings on the housing.

The only disadvantage is on the EM speed, i.e. it is possible to use a range between 4500 RPM and 5500 RPM.

For these reasons, this layout is the architecture adopted for all after calculations to follow. This is the better solution of all in terms of weight and volume.

In the end, by layout of Figure 2.6 is is possible to add the EM and obtain the other two solutions 2.12.

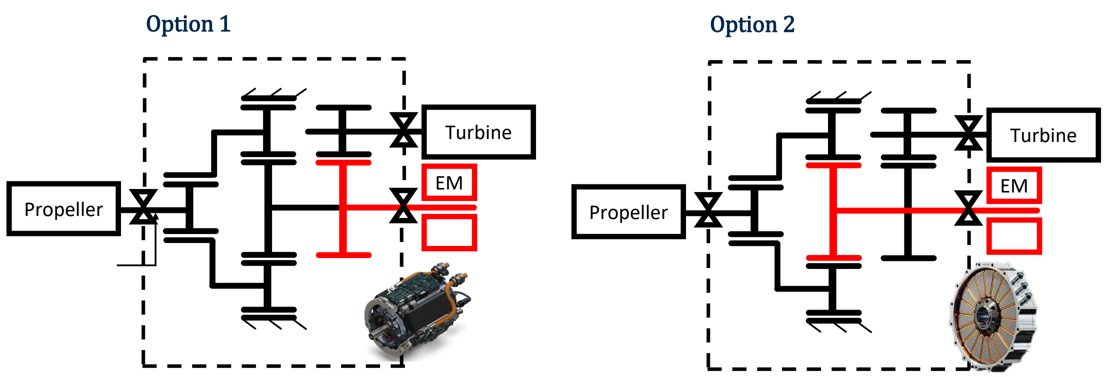

Figure 2.12: Mixed Hybrid Architecture

This layout uses an off-set configuration in the first stage of reduction and an in-line architecture in the second stage of reduction.

Starting from this configuration you can use a high-speed EM "Option 1" or a low-speed EM in "Option 2".

The operation is similar to the previous cases.

The only difference is in Option 2. In this case, the power and torque of EM are discharged directly in the second stage of reduction. To do this it uses a grooved coaxial shaft. This architecture is useful when the axes of GT and the axes of EM are not in the same axe, whit a higher complication with respect to other earlier layouts.

2.3 Gears Sizing for Conventional Propulsion

This chapter will analyse the sizing of all three layouts seen before. It starts with parallel shafts architecture, after with mixed architecture and at the end with in-line architecture.

The methodology for all sizing consists of calc the gear ratio of all transmissions and single stage, after the aim is to find the power and torque flux and finally size each component, gear and shaft (Figure 2.13).

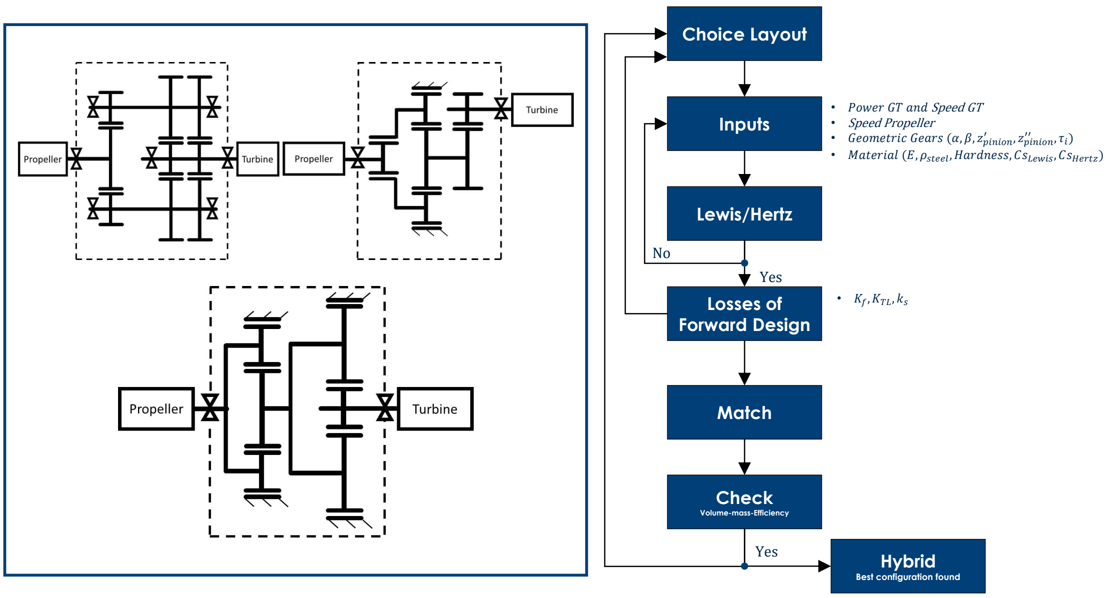

Figure 2.13: Methodology

After individuating the power flux and the critical meshing the gearbox has been pre-sizing with Lewis (2.1) and Hertz's theory (2.2 - 2.3) to estimate the weight of all transmission components.

$$m_{n,i} = \sqrt{\frac{2T_iY(z_{v,i})cos\beta_i}{\lambda \cdot z_i \cdot \sigma_{Rp02}/Cs_{Lewis}}} \quad z_v = \frac{z_i}{cos^2\beta_{bi} \cdot cos\beta_i}$$
$$\beta_{bi} = arcisn(sin\beta_i \cdot cos\alpha_i) \tag{2.1}$$

$$\frac{\sigma_{H0}}{Cs_{Hertz}} = \frac{2.5 \cdot HB}{Cs_{Hertz}} \geq 0.4118 \cdot \sqrt{\frac{\frac{F_{t,i}}{cos\alpha_i \cdot sin\alpha_i} \cdot E \cdot \frac{r_i + r_j}{r_ir_j}}{\frac{b_i}{cos\beta_i}}} \tag{2.2}$$

$$\epsilon_{\beta_i} = \frac{b \cdot sin\beta_i}{\pi \cdot m_{ni}} \geq 1.15 \quad b_i = \frac{1.15 \cdot \pi \cdot m_{ni}}{sin\beta_i} \tag{2.3}$$

In reference to Figure 2.2, the gear ratio, total (2.4) and for single stage (2.5), has been written:

$$\tau = \frac{\omega_{in}}{\omega_{out}} = \frac{\omega_{GT}}{\omega_{prop}} = \frac{\omega_1}{\omega_2} \cdot \frac{\omega_2}{\omega_6} \cdot \frac{\omega_6}{\omega_5}$$
$$\tau = \frac{\omega_1}{\omega_2} \cdot 1 \cdot \frac{\omega_6}{\omega_5} = \tau_{12} \cdot \tau_{65} = \frac{z_2}{z_1} \cdot \frac{z_5}{z_6} \tag{2.4}$$
$$\tau = \frac{z_2 \cdot z_5}{z_1 \cdot z_6}$$

$$\tau_{12,i} = \sqrt{\tau} \cdot \psi \quad \tau_{65,i} = \frac{\tau}{\tau_{12,i}} \tag{2.5}$$

$$z_{min,1} = \frac{2 \cdot cos^3\beta_1 \cdot (1 - x_1)}{sin^2\alpha_1} \tag{2.6}$$

Where:

- z_i with I for 1 to 6 are the number of number of i-th wheel teeth
- ψ is a corrective factor (input) to change the way the speeds are distributed in the transmission
- ω_i gear speed of i-th wheels
- x_i wheel toothing correction factor

Individuated the gear ratio of all stages, it is possible to fix the number of teeth of the pinions of the first and second stages (z_1 and z_6) by verifying (2.6).

This process continues until convergence is achieved, or the difference between the ideal total gear ratio and the effective total gear ratio is less than a fixed percentage (in this case 5%).

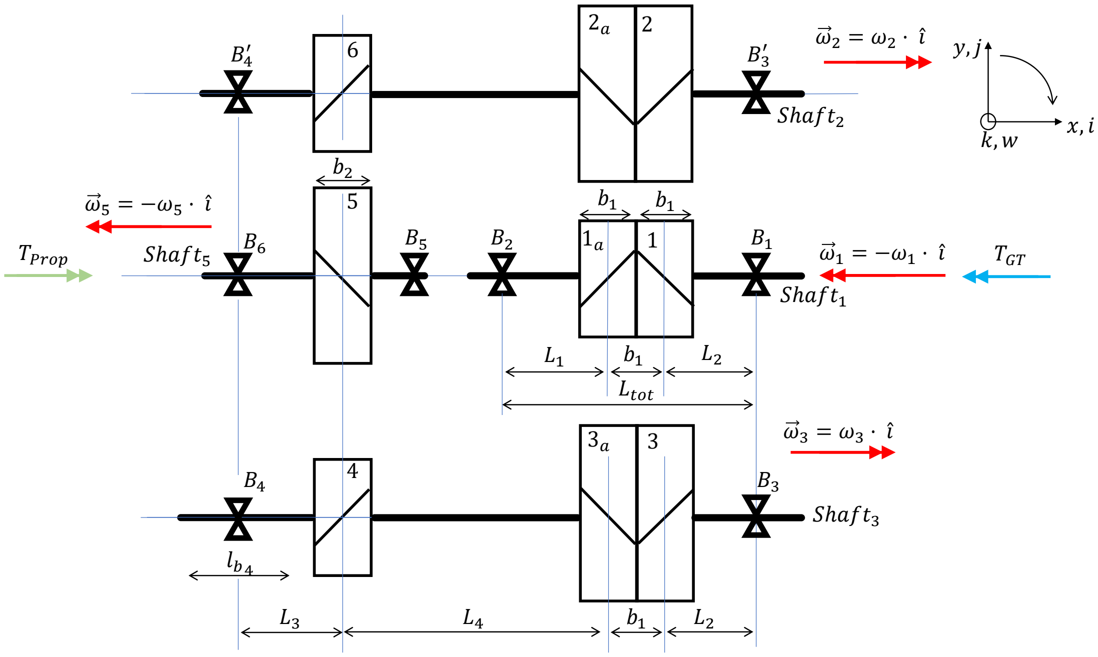

Figure 2.14: Degree Of Freedom Off-Set Architecture

Switching to power flow calculation, always in reference to Figure 2.2, the free body diagram is represented in Figure 2.14.

For this type of layout, the power flux is as follows:

$$P_{GT} = T_1 \cdot \omega_1 + T_{1a} \cdot \omega_{1a} = T_{GT} \cdot \omega_{GT} \tag{2.7}$$

But the speeds are equal because of the same shaft, and the layout is symmetrical, therefore the equation (2.7) becomes (2.8):

$$\begin{aligned} T_{GT} &= T_1 + T_{1a} \\ T_1 &= T_{1a} = \frac{T_{GT}}{2} \end{aligned} \tag{2.8}$$

Figure 2.15 represents the first stage of meshing and it is possible to write the forces which discharge on the teeth.

So the equations are:

$$T_1 = \frac{T_{GT}}{2} = F_{t13} \cdot \frac{m_1 z_1}{2} + F_{t12} \cdot \frac{m_1 z_1}{2} = T_{13} + T_{12} \tag{2.9}$$

In the end, in a single meshing of the first stage of reduction, the pinion sees the 50% of the GT power and the 25% of the same torque. So the module with the Lewis method of the first stage results in (2.10):

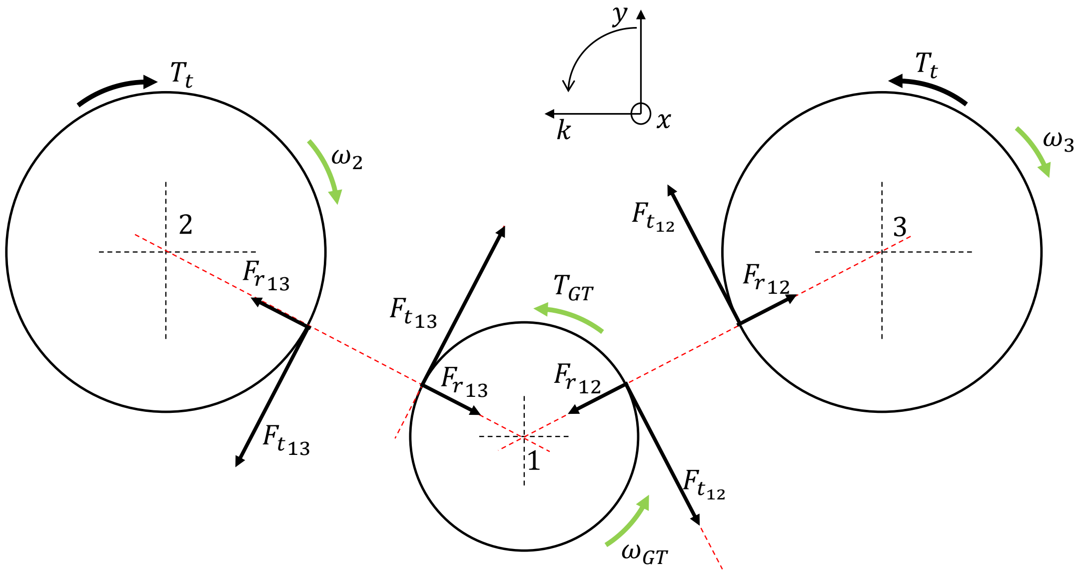

Figure 2.15: Meshing First Stage between Gears 1,2 and 3

$$m_{n1} = \sqrt{\frac{2T_{13}Y(z_v)cos\beta_1}{\lambda \cdot z_1 \cdot \sigma_{Rp02}/Cs_{Lewis}}} \tag{2.10}$$

$$z_v = \frac{z_i}{cos^2\beta_{b1} \cdot cos\beta_1} \quad \beta_{b1} = arcisn(sin\beta_1 \cdot cos\alpha_1) \tag{2.11}$$

Where:

- T_{12} is the torque of meshing considered
- $Y(z_v)$ is the Lewis coefficient which depends on virtual teeth (more the number of teeth is little more this coefficient is higher)
- $cos\beta$ takes into account the inclination of the tooth and, in this case, is not zero because there are helical gears
- z_i is the number of teeth of the littler gear, so the pinion
- σ_{RP02}/CS_{Lewis} is the admissible tension, so the maximum elastic tension divided by the adopted safety Lewis coefficient

In addition, the $Y(z_v)$ is calculated for incorrect gears ($x_1 = 0$ and $x_3 = 0$) since this is a preliminary sizing to gearbox weight and volume estimation.

After calculating the module with Lewis it is possible to use Hertz (2.12) to size a Hertzian contact, so at the maximum pressure of contact.

In this case, equation 2.12 will be used with the conditions on the coverage ratio and bandwidth (2.13)

$$\frac{\sigma_{H0}}{Cs_{Hertz}} = \frac{2.5 \cdot HB}{Cs_{Hertz}} \geq 0.4118 \cdot \sqrt{\frac{\frac{F_{t,13}}{cos\alpha_1 \cdot sin\alpha_1} \cdot E \cdot \frac{r_1 + r_3}{r_1 r_3}}{\frac{b_1}{cos\beta_1}}} \tag{2.12}$$

$$\epsilon_{\beta 1} = \frac{b \cdot sin\beta_1}{\pi \cdot m_{n1}} \geq 1.15 \quad b_1 = \frac{1.15 \cdot \pi \cdot m_{n1}}{sin\beta_1} \tag{2.13}$$

Finished this part the size of the first stage of reduction is known. Now is possible to calculate the second stage with the same methodology, so power and torque flux, to find the critical meshing and sizing it.

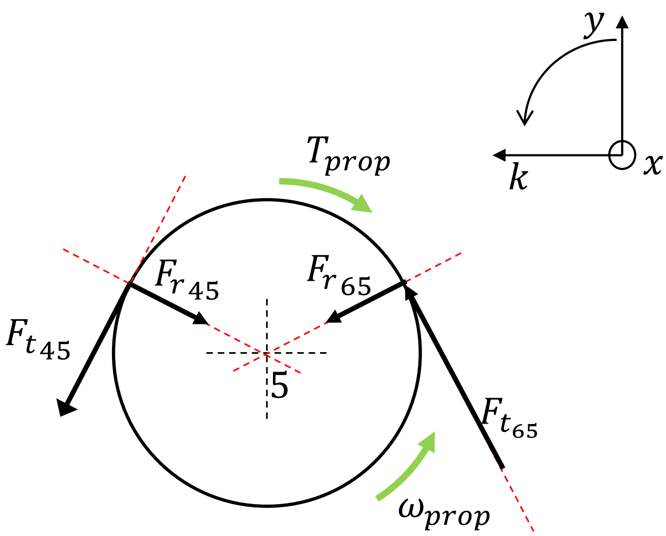

Figure 2.16: Propeller Gear

In reference Figure 2.16 it is possible to see the degree of freedom of gear number five, so the linked gear to the propeller shaft. The power flux is following (2.15):

$$T_2 \cdot \omega_2 + T_{2a} \cdot \omega_{2a} = T_6 \cdot \omega_6 = P_6 = \frac{P_{GT}}{2} \tag{2.14}$$

But the speed are equal, so:

$$
\begin{aligned}
&T_1 \cdot \omega_1 = T_2 \cdot \omega_2 + T_3 \cdot \omega_3 \\
&T_1 \cdot \omega_1 = 2 \cdot T_2 \cdot \omega_2 \\
&T_2 = \frac{T_1 \cdot \omega_1}{2 \cdot \omega_2} = \frac{T_1}{2} \cdot \tau_{12} = \frac{T_1}{2} \cdot \frac{z_2}{z_1} \\
&T_{2a} = \frac{T_{1a}}{2} \cdot \frac{z_{2a}}{z_{1a}} \\
&T_6 = T_2 + T_{2a} = \frac{T_1}{2} \cdot \frac{z_2}{z_1} + \frac{T_{1a}}{2} \cdot \frac{z_{2a}}{z_{1a}} = T_1 \cdot \frac{z_2}{z_1}
\end{aligned} \tag{2.15}
$$

So the torque of pinion 6 is known and by eq. (2.1) and (2.2) used it to mesh is possible to calculate the module (eq. 2.16 and 2.17).

$$
\begin{aligned}
&m_{n,6} = \sqrt{\frac{2T_6 Y(z_{v,6}) cos\beta_2}{\lambda \cdot z_6 \cdot \sigma_{Rp02}/Cs_{Lewis}}} \quad z_{v,6} = \frac{z_6}{cos^2\beta_{b2} \cdot cos\beta_2} \\
&\beta_{b2} = arcisn(sin\beta_2 \cdot cos\alpha_2)
\end{aligned} \tag{2.16}
$$

$$
\frac{\sigma_{H0}}{Cs_{Hertz}} = \frac{2.5 \cdot HB}{Cs_{Hertz}} \geq 0.4118 \cdot \sqrt{\frac{\frac{F_{t,65}}{cos\alpha_2 \cdot sin\alpha_2} \cdot E \cdot \frac{r_6 + r_5}{r_5 r_6}}{\frac{b_6}{cos\beta_2}}} \tag{2.17}
$$

Now the sizes of all gears are known, so it's possible to calculate firstly the volume (2.18) and after the weight (2.19).

In general, the volume of single gear is the following (2.18):

$$
V_{g,i} = \frac{\pi}{4} \cdot \left(\frac{m_i \cdot z_i}{2}\right)^2 \tag{2.18}
$$

$$
W_{g,i} = V_i \cdot \rho \tag{2.19}
$$

In this point the first layout is sized, so the mass and the dimension are known and consequentially is possible to pass to analyse the second layout: mixed architecture represented in Figure 2.6.

This architecture, represented in Figure 2.17, is a hybrid beten an Offset layout and an in-line layout in that, in the first stage, there is an Offset between the axis of the GT and the axis of the first crown. After that, there is an In-line configuration so the axis of the first sun, the second sun and the crown of the first stage are all in-line whit the axis of the propeller. Add to this, in the first stage of reduction, there is a double helical gear in such a way that the axial force is equal to zero for both, the first and second stages of reduction (in this way the bearing firstly and the housing secondly shall not support axial forces).

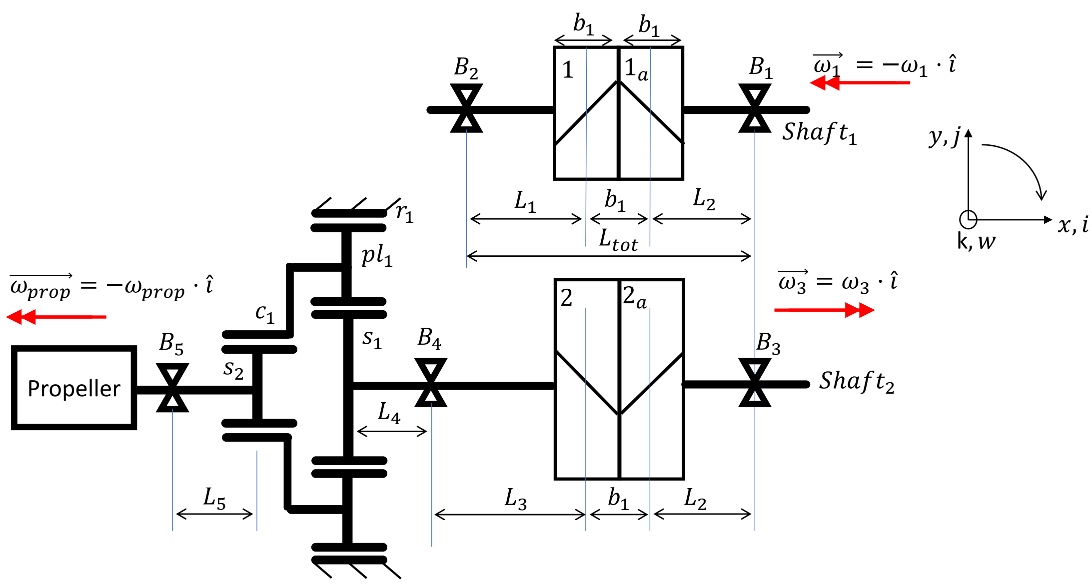

Figure 2.17: Degree Of Freedom of Mixed Architecture

As in the before case, the kinematic relations are (2.20) and (2.21):

$$\tau = \tau_1 \cdot \tau_2 \cdot \tau_3 \tag{2.20}$$

$$\tau = \frac{z_2}{z_1} \cdot \left(1 + \frac{z_{r1}}{z_{s1}}\right) \cdot 1 \tag{2.21}$$

$$z_s + 2z_p = z_r \tag{2.22}$$

The equation (2.21) the calculation of τ_2 will be explained after, in the third architecture. Like in the before case, inside the τ_1, is considered a corrective factor to change the distribution of torque between different gears (inside the formula is not explicated).

Like the previous case following the calculation of power and torque flux for each mesh (2.23 - 2.24 - 2.28), this will be useful for the Lewis and Hertz module calculation.

$$\begin{aligned} P_{GT} &= T_1 \cdot \omega_1 + T_{1a} \cdot \omega_{1a} \\ T_{GT} &= T_1 + T_{1a} = \frac{T_{GT}}{2} \end{aligned} \tag{2.23}$$

$$
\begin{aligned}
&T_1 \cdot \omega_1 = T_2 \cdot \omega_2 \\
&T_{1a} \cdot \omega_{1a} = T_{2a} \cdot \omega_{2a} \\
&T_2 = T_1 \cdot \tau_{12} \qquad\qquad T_{2a} = T_{1a} \cdot \tau_{1a2a} \\
&T_{s1} = T_2 + T_{2a}
\end{aligned}
\tag{2.24}
$$

$$T_{s1} = T_1 \cdot \tau_{12} + T_{1a} \cdot \tau_{1a2a} \tag{2.25}$$

$$T_{s1} = \sum_{i=1}^{N_{contacts}} (F_{t,s1pl-i}) \cdot \frac{m_{s1} z_{s1}}{2} \tag{2.26}$$

For a number of planets N_{pl} equal to three the equation (2.26) becomes equation (2.25):

$$T_{s1} = (F_{t,s1pl1} + F_{t,s1pl2} + F_{t,s1pl3}) \cdot \frac{m_{s1} z_{s1}}{2} \tag{2.27}$$

$$T_{s1} = T_{s1pl1} + T_{s1pl2} + T_{s1pl3} = T_{s1}/N_{pl} \tag{2.28}$$

$$T_{s2} = T_{s1} \cdot \tau_2 \quad T_{s2} = T_{prop} = P_{GT}/\omega_{prop} \tag{2.29}$$

Now, using the equation (2.1) and (2.2) with the (2.23) for the first stage, with the (2.24) for second stage (first sun) and whit (2.29) for the final stage (second sun), is possible to calculate the module and so the mass of the system.

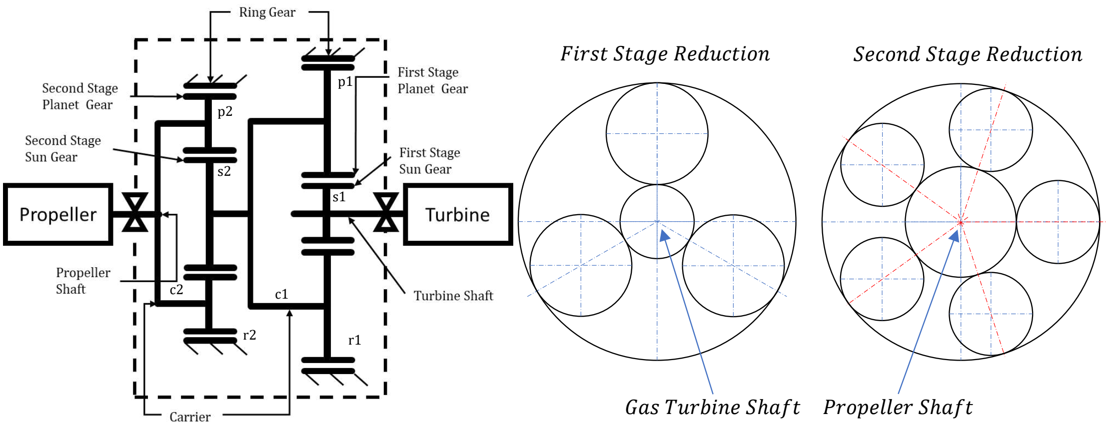

Figure 2.18: In-Line Architecture

For the third gearbox architecture, reference in Figure 2.18, the process to size it is the same using Offset and Mixed layouts. Then, to not burden the explanation, it will report only the kinematic calculation (with a note about the gear ratio between stages and total) and the power and torque flux.

In this case, there are two stages of reduction and each is an epicycloidal mechanism. Then, for the definition of the epicycloidal mechanism, it has two degrees of freedom and it is impossible to write an only equation about the gear ratio if it does not fix one shaft speed (2.31).

In formulas, this is reported following:

$$\tau = \frac{\omega_{GT}}{\omega_{prop}} = \frac{\omega_{s1}}{\omega_{c1}} \cdot \frac{\omega_{s2}}{\omega_{c2}} = \tau_1 \cdot \tau_2 \tag{2.30}$$

In the first stage it is possible to write the gear ratio whit Lewis's method :

$$\tau_1 = \frac{\omega_{s1} - \omega_{c1}}{\omega_{r1} - \omega_{c1}} \tag{2.31}$$

In reference to Figure 2.18 the rings are fixed for both architectures so

$$\omega_{r1} = \omega_{r2} = 0 \tag{2.32}$$

$$\begin{aligned} &\omega_{c1} = \omega_{s2} \quad \omega_{c2} = \omega_{prop} \\ &\omega_{s1} = \omega_{GT} \quad \omega_{c1} = \omega_{s2} \end{aligned} \tag{2.33}$$

By combining equations (2.31) and (2.32) we obtain (2.34)

$$\begin{aligned} &\frac{\omega_{s1} - \omega_{c1}}{-\omega_{c1}} = -\frac{z_{pl1}}{z_{s1}} \cdot \frac{z_{r1}}{z_{pl1}} = -\frac{z_{r1}}{z_{s1}} \\ &\tau_{01} = \frac{z_{r1}}{z_{s1}} \\ &\tau_1 = 1 - \frac{\omega_{s1}}{\omega_{c1}} = -\tau_{01} \\ &\tau_1 = \tau_{01} + 1 \end{aligned} \tag{2.34}$$

By joining (2.33) whit (2.34), obtain:

$$\tau_1 = \frac{\omega_{s1}}{\omega_{s2}} = \frac{z_{r1}}{z_{s1}} + 1 \tag{2.35}$$

The procedure to write the second stage of reduction is equal to that reported between (2.30) - (2.35). So it is reported only the result of the second stage and the total gear ratio in (2.36) - (2.37).

$$\tau_2 = \frac{\omega_{s2}}{\omega_{prop}} = \frac{z_{r2}}{z_{s2}} + 1 \tag{2.36}$$

$$\tau = \tau_1 \cdot \tau_2 = \left(\frac{z_{r1}}{z_{s1}} + 1\right) \cdot \left(\frac{z_{r2}}{z_{s2}} + 1\right) \tag{2.37}$$

So knowing the gear ratio of the first and the second stages (eq. 2.37) makes it possible to calculate the output torque (eq. 2.38), that means the propeller torque as following:

$$T_{prop} = T_{GT} \cdot \left(\frac{z_{r1}}{z_{s1}} + 1\right) \cdot \left(\frac{z_{r2}}{z_{s2}} + 1\right) \tag{2.38}$$

Then the output torque will be more significant if smaller suns, s_1 and s_2, and bigger rings, r_1 and r_2, will be adopted.

Readjusting the equations (2.1), (2.2) and (2.3) to (2.39) and (2.41) is possible to know the size of all transmissions.

$$m_{n,s_1} = \sqrt{\frac{2 \cdot T_{GT} \cdot Y(z_{s_1})}{N_{pl1} \cdot \lambda \cdot z_{s_1} \cdot \sigma_{Rp02}/Cs_{Lewis}}} \tag{2.39}$$

$$m_{n,s_2} = \sqrt{\frac{2 \cdot T_{prop} \cdot Y(z_{s_2})}{N_{pl2} \cdot \lambda \cdot z_{s_2} \cdot \sigma_{Rp02}/Cs_{Lewis}}} \tag{2.40}$$

$$\frac{\sigma_{H0}}{Cs_{Hertz}} = \frac{2.5 \cdot HB}{Cs_{Hertz}} \geq 0.4118 \cdot \sqrt{\frac{\frac{F_{t,s_1p_{11}}}{cos\alpha \cdot sin\alpha} \cdot E \cdot \frac{r_{s_1} + r_{p_{11}}}{r_{s_1} r_{p_{11}}}}{b}} \tag{2.41}$$

$$\frac{\sigma_{H0}}{Cs_{Hertz}} = \frac{2.5 \cdot HB}{Cs_{Hertz}} \geq 0.4118 \cdot \sqrt{\frac{\frac{F_{t,s_2p_{21}}}{cos\alpha_2 \cdot sin\alpha_2} \cdot E \cdot \frac{r_{s_2} + r_{p_{21}}}{r_{s_2} r_{p_{21}}}}{b}} \tag{2.42}$$

Should be noted that the eq.(2.39) is valid if the number of teeth of the sun s_1 is smaller than the number of teeth of the planet p_{11}. If this is not true inside the eq.(2.39) or eq.(2.40) must be insert the number of teeth of the planet in $Y(z_{p11})$ or $Y(z_{p21})$ because the higher module is given from the ratio between a higher torque and a smaller number of teeth.

2.4 Shafts Sizing for Conventional Propulsion

In this part of the work, the dimensions, the weights and the volume of all gears in the transmission are known, therefore the next goal is sizing the shafts to link the transmission stages. In order will be analyzed: the Off-Set architecture, the In-Line architecture and in the end the Mixed architecture.

As explained previously some layouts are helical gears, Off-Set architecture (Figure 2.2), others have spur gears, In-Line architecture (Figure 2.4), and only one has a mixed layout between the spur and helical gears, Mixed architecture (Figure 2.6).

If you analyze the helical gears in the first architecture (Off-Set layout) it is possible to split the plane between radial and axial force and after with tangential force. In this way is possible to calc the single effect of each force and after use the superposition to obtain the real size of the shaft under all forces. In reality, is enough to combine the forces previously and then use them to calculate the maximum bending moment to size the shaft. This is possible because the shafts are cylindric and then they have a double plane of symmetry.

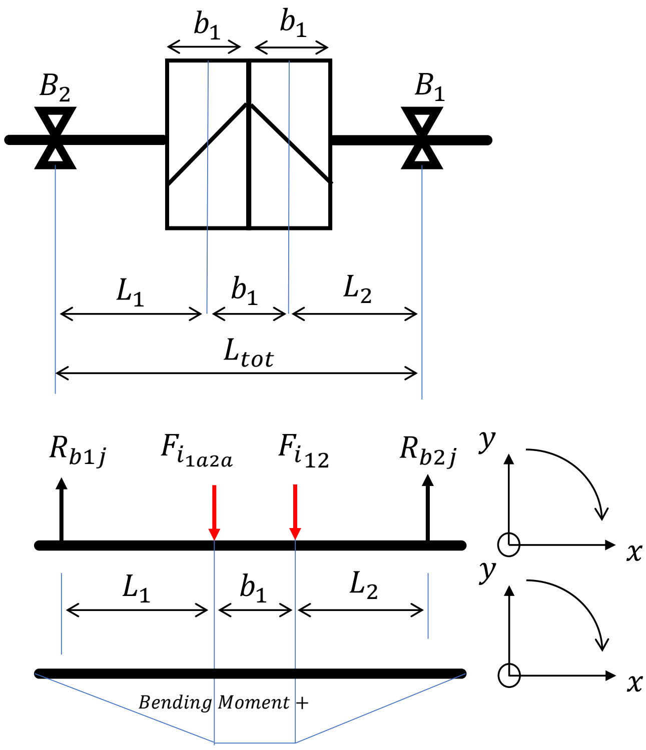

Figure 2.19: Shaft 1 Off-Set Architecture

From reference to Figure 2.14 is possible to describe the forces discharged over the first shaft of reduction (Figure 2.19). With reference to this is possible to write two equations of equilibrium to vertical translation and moment (2.43):

$$\begin{aligned} R_{b_1,j} + R_{b_2,j} - F_{i,1_a2_a} - F_{i,12} = 0 \\ R_{b_2,j} = \frac{F_{i,1_a2_a} \cdot L_1 + F_{i,12} \cdot (L_1 + b_1)}{L_1 + b_1 + L_2} \end{aligned} \tag{2.43}$$

The next step is to calculate the max bending moment between the three sections

(Figure 2.20): $R_{b_1,j}$ and $F_{i,1_a2_a}$ (Section I), $F_{i,1_a2_a}$ and $F_{i,12}$ (Section II) and $F_{i,12}$ and $R_{b_2,j}$ (Section III).

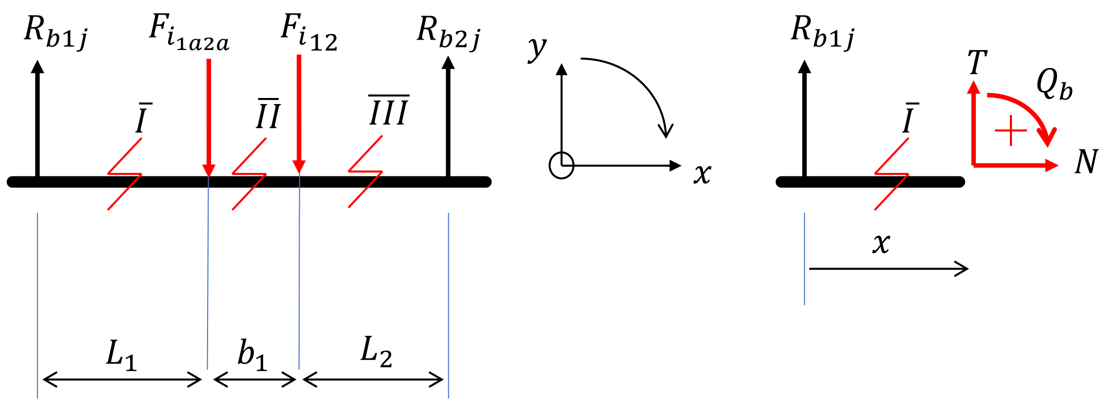

Figure 2.20: Section Shaft 1 in Off-Set Architecture

With reference always to Figure 2.20 is possible to write one equation for each section as follows (eq. 2.44):

$$\begin{aligned}
&R_{b_1,j} \cdot x + Q_b = 0 \\
&Q_b = -R_{b_1,j} \cdot x && 0 \leq x \leq L_1 \\
&Q_b = -[R_{b_1,j} \cdot (L_1 + x) - F_{i,1_a2_a} \cdot x] && 0 \leq x \leq b_1 \\
&Q_b = -[R_{b_1,j} \cdot (L_1 + b_1 + x) - F_{i,1_a2_a} \cdot (b_1 + x) - F_{i,12} \cdot x] && 0 \leq x \leq L_2
\end{aligned} \tag{2.44}$$

This procedure is followed for each shaft to aim to determine the size and then the weight itself to add to the weight of helical gears previously calculated.

Always from reference to Figure 2.14 is possible to describe the forces discharged over the second shaft of reduction (Figure 2.21)

The procedure to calculate the constraining forces of reaction and the maximum bending moment is the same as "Shaft 1" with the difference, in this case, of one added helical pinion gear.

So the constraining forces of reaction are reported in eq.(2.45) and moment's trend is reported in eq.(2.46) (with the same convention used for previously calculated)

$$\begin{aligned}
&R_{b_4,y} + R_{b_3,y} - F_{i,45} - F_{i,1_a3_a} - F_{i,13} = 0 \\
&R_{b_3,y} = \frac{F_{i,13} \cdot (L_3 + L_4 + b_1) + F_{i,1_a3_a} \cdot (L_3 + L_4) - F_{i,45} \cdot L_3}{L_3 + L_4 + b_1 + L_2}
\end{aligned} \tag{2.45}$$

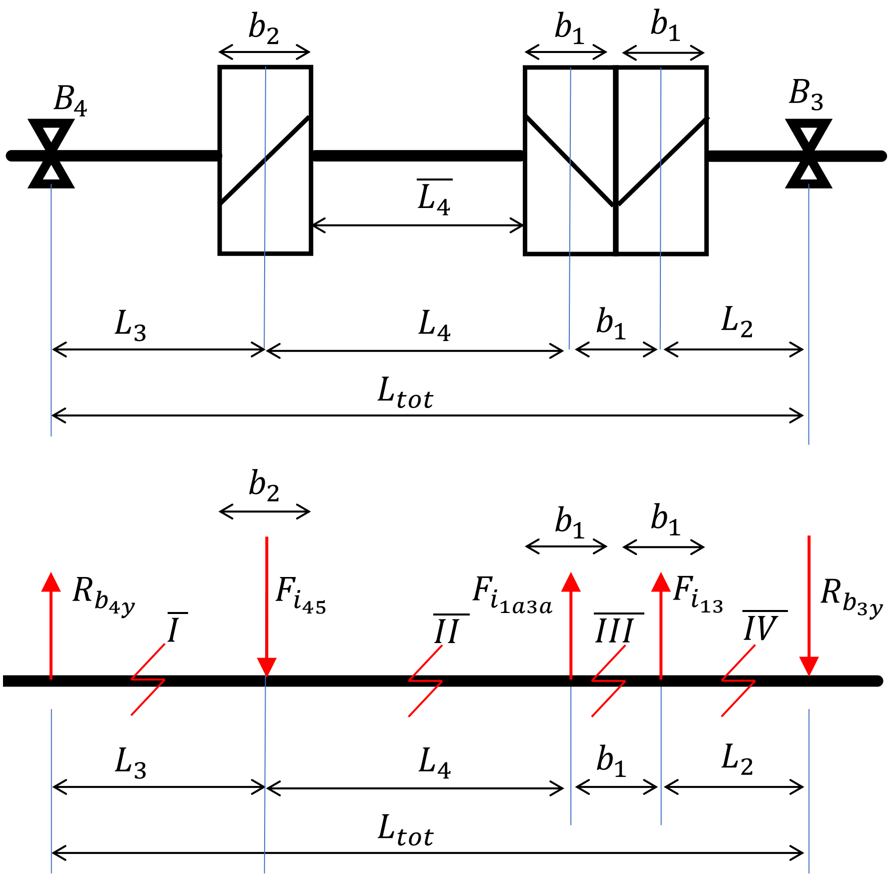

Figure 2.21: Shaft 3 Off-Set Architecture

$$
\begin{aligned}
&0 \leq x \leq L_3 \\
&Q_b = -R_{b_4,y} \cdot x \\
\\
&0 \leq x \leq L_4 \\
&Q_b = -[R_{b_4,y} \cdot (L_3 + x) - F_{i,45} \cdot x] \\
\\
&0 \leq x \leq b_1 \\
&Q_b = -[R_{b_4,y} \cdot (L_3 + L_4 + x) - F_{i,45} \cdot (L_4 + x) + F_{i,1_a3_a} \cdot x] \\
\\
&0 \leq x \leq L_2 \\
&Q_b = -[R_{b_4,y} \cdot (L_3 + L_4 + b_1 + x) - F_{i,45} \cdot (L_4 + b_1 + x) + \\
&+ F_{i,1_a3_a} \cdot (b_1 + x) + F_{i,13}] \cdot x
\end{aligned}
\tag{2.46}
$$

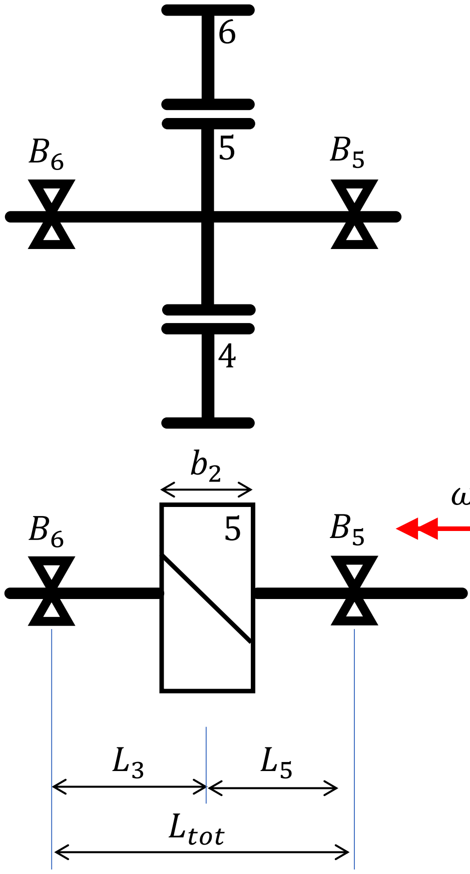

Figure 2.22: Shaft 3 Off-Set Architecture

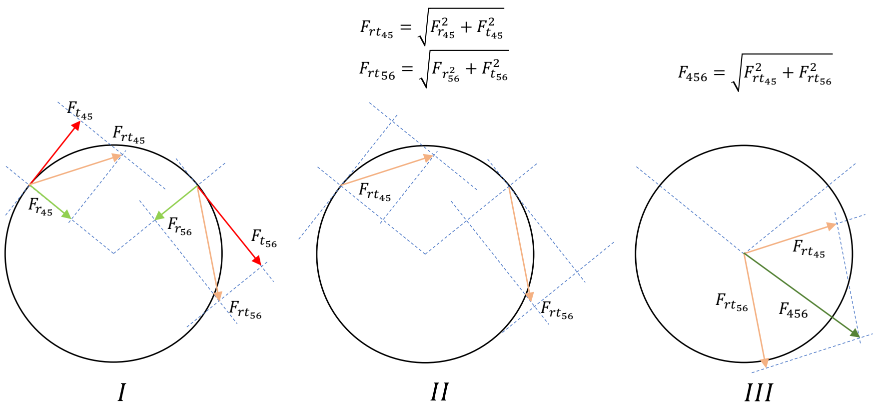

Figure 2.23: Gear of Shaft 3 Off-Set Architecture

In the end, to reference in Figures 2.22 and 2.23, it is possible to understand how the gears's forces are downloaded in the last shaft, which means the propeller's shaft.

Given that the procedure of calculation of the constraining forces of reaction and the maximum bending moment is equal to previous cases and more complex, in this case, it is not reported.

$$\frac{\sigma_{Rp0.2}}{C_s} = \sqrt{\sigma_b^2 + 4 \cdot \tau_t^2} = \sqrt{\left(\frac{32 \cdot Q_b}{\pi \cdot d^3}\right)^2 + 4 \cdot \left(\frac{16 \cdot T}{\pi \cdot d^3}\right)^2} \tag{2.47}$$

Now the information about the maximum bending moment and torque discharged for each shaft are known, then by eq.(2.47) is possible to calculate all shaft diameters.

Now, all information about the first architecture, in terms of mass and volume, is known.

It is possible to follow this procedure to analyze the second layout, namely In-Line architecture (Figure 2.18).

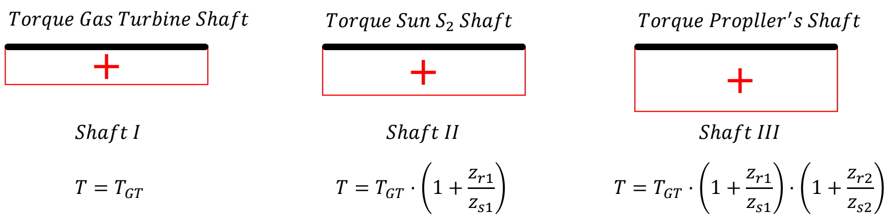

Figure 2.24: Torques to the shafts in the In-Line Architecture

In this case, the linking shafts between the first, second and third stages are all under torsion stress only, so is possible to calculate the torsion stress for each shaft, by eq.(2.47), by changing the torque discharged as illustrated in Figure 2.24.

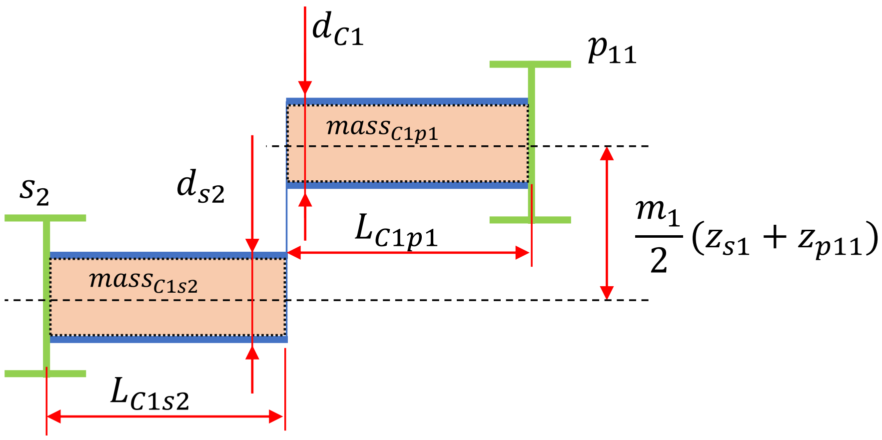

Figure 2.25: Degree Of Freedom of Carrier First Stage

In this architecture, the linking between the first sun (s_1) and the second sun (s_2), is done by carrier 1 (c_1) (Figure 2.25).

In Figure 2.25, it is possible to see how the carrier is modelled, namely two cantilever shafts for the planet of the first stage and the sun of the second stage. While, in the central part, the linking between the planet shaft to the sun shaft is neglected.

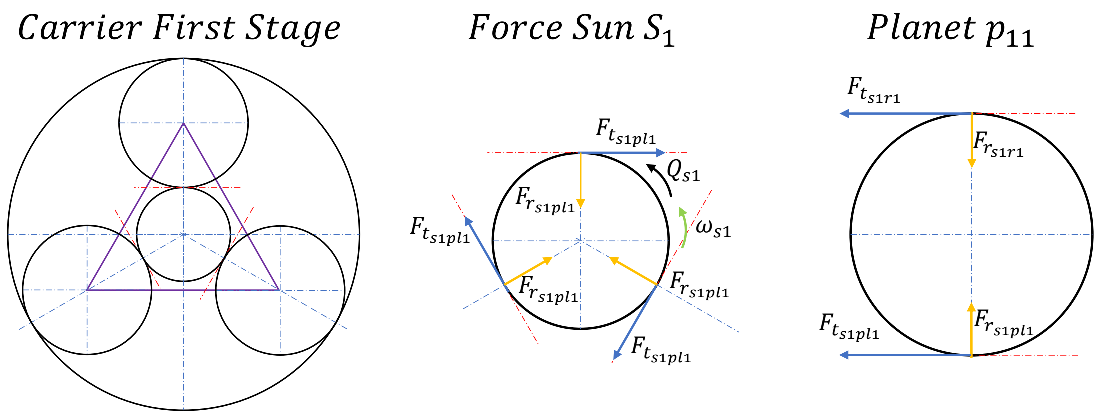

Figure 2.26: Degree Of Freedom of First Stage Carrier

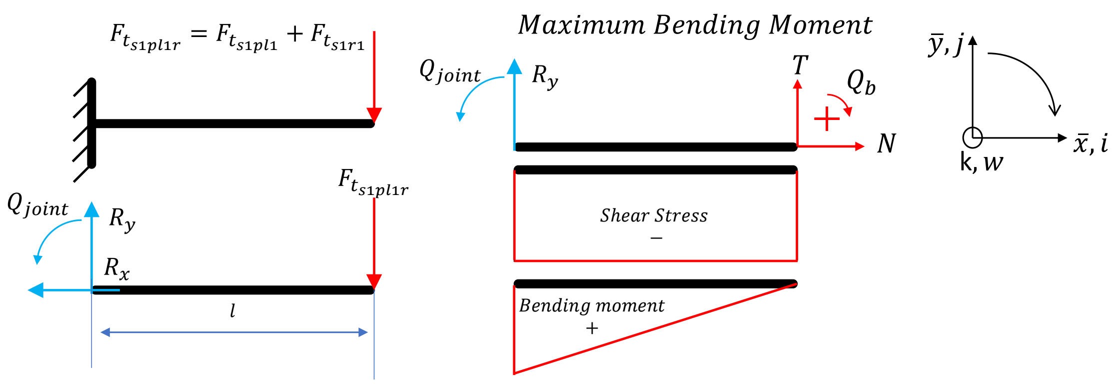

Figure 2.27: Carrier First Stage Force

Also, observing how the forces are discharged (Figures 2.26 2.27) it is possible to see that the carrier is equal at the free body diagram of the cantilever shaft, so the bending moment and shear force are easy to calculate. Other than this the carrier is subjected only to a bending moment and shear force and not torque (only normal stress tension).

In the end, it is possible to analyse the Mixed Architecture in Figure 2.17. The process of sizing is equal to previous models, namely is possible to take the sizing algorithm, flux of power and torque, of the first stage of reduction of Off-Set Architecture to size the first stage of reduction of the Mixed Architecture and for the second and third stages is possible refer to flux power and torque of the In-Line Architecture (the planetary stages).

2.5 Gears Sizing for Hybrid Propulsion

As regards Hybrid propulsion, the methodology is similar to conventional propulsion, taking into account that the contribution of the Electric Motor in terms of power and especially torque must be considered.

Each architecture must take into account the considerations made in Chapter 2.2 about the type of EM, in relation to the flux radial or axial, the range of rotation speed of the machine and the size of itself.

By the analyse the Off-Set Hybrid Architecture, Off-Set H1 in Figure 2.9 and Figure 2.28 it is possible to write the new flux of power and torque, eq.(2.48).

$$\begin{aligned} &P_{EM} + P_{GT} = P_{prop} \\ &T_{EM} \cdot \omega_{EM} + T_{GT} \cdot \omega_{GT} = T_{prop} \cdot \omega_{prop} \\ &T_{prop} = T_{EM} \cdot \frac{\omega_{1a}}{\omega_5} + T_{GT} \cdot \frac{\omega_1}{\omega_5} \end{aligned} \tag{2.48}$$

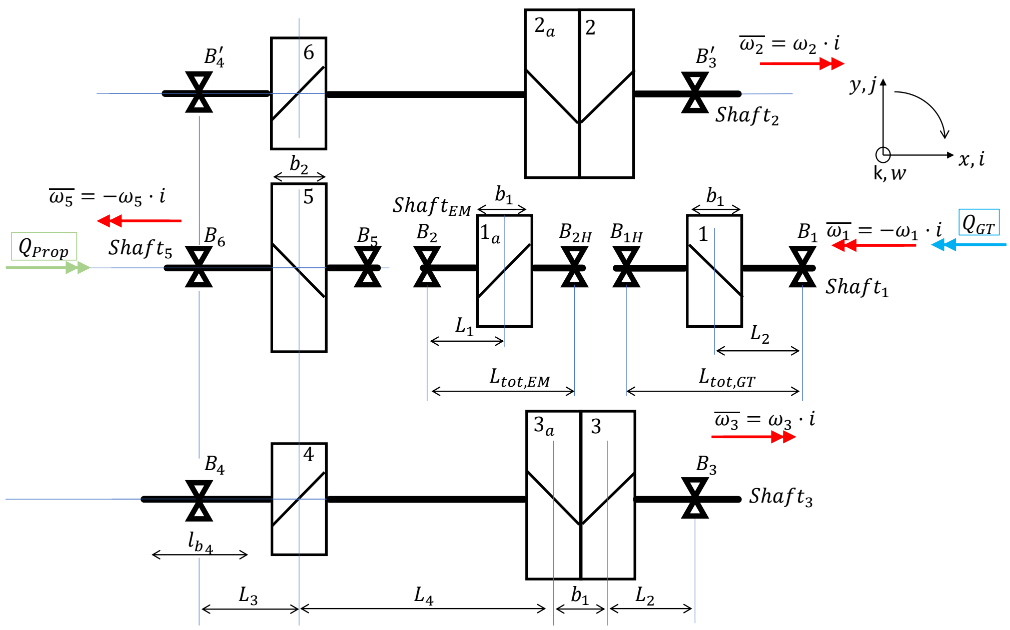

Figure 2.28: Off-Set Hybrid Architecture - Off-Set H1

Explaining the gear ratio with the rotational speed in the gear ratio of teeth, it obtain:

$$\begin{aligned}
&T_{prop} = T_{EM} \cdot \frac{z_{2a} z_5}{z_{1a} z_6} + T_{GT} \cdot \frac{z_2 z_5}{z_1 z_6} \\
&T_{prop} \cdot \omega_5 = T_6 \cdot \omega_6 + T_5 \cdot \omega_5 = 2T_6 \omega_6 \\
&T_6 = \frac{T_{prop}}{2} \cdot \frac{\omega_5}{\omega_6}
\end{aligned} \tag{2.49}$$

So it is possible to calculate the module for the first and the second stages as follows:

$$m_{n1} = \sqrt{\frac{2\frac{T_{GT}}{2} Y(z_{v,1}) cos\beta_1}{\lambda \cdot z_1 \cdot \sigma_{Rp02}/Cs_{Lewis}}} \tag{2.50}$$

$$m_{n1a} = \sqrt{\frac{2\frac{T_{EM}}{2} Y(z_{v,1a}) cos\beta_{1a}}{\lambda \cdot z_{1a} \cdot \sigma_{Rp02}/Cs_{Lewis}}} \tag{2.51}$$

$$m_{n2} = \sqrt{\frac{2T_6 Y(z_{v,6}) cos\beta_2}{\lambda \cdot z_6 \cdot \sigma_{Rp02}/Cs_{Lewis}}} \tag{2.52}$$

In the case of Off-Set H2, as referenced in Figure 2.9, the first stage of reduction is equal to conventional propulsion, while, for the second stage of reduction, the pinion of EM must be considered and added to the whole system (gear 7).

$$\begin{aligned}
&T_1 \cdot \omega_1 = T_2 \cdot \omega_2 + T_3 \cdot \omega_3 \\
&T_2 = T_3
\end{aligned} \tag{2.53}$$

$$\begin{aligned}
&T_{GT} \cdot \omega_{GT} = T_1 \cdot \omega_1 + T_{1a} \cdot \omega_{1a} \\
&T_{GT} = T_1 + T_{1a}
\end{aligned} \tag{2.54}$$

$$\begin{aligned}
&T_1 = T_{1a} = \frac{T_{GT}}{2} \\
&T_2 = T_{2a} = \frac{T_1}{2} \cdot \frac{\omega_1}{\omega_2} = \frac{T_{GT}}{4} \cdot \frac{z_2}{z_1}
\end{aligned} \tag{2.55}$$

$$\begin{aligned}
&T_7 \cdot \omega_7 = T_{EM} \cdot \omega_7 \\
&T_{EM} \cdot \omega_7 = T_6 \cdot \omega_6 + T_4 \cdot \omega_4
\end{aligned} \tag{2.56}$$

$$\begin{aligned}
&T_{EM} \cdot \omega_7 = 2T_{6,EM} \cdot \omega_6 \\
&T_{6,EM} = \frac{T_{EM}}{2} \cdot \frac{z_6}{z_7}
\end{aligned} \tag{2.57}$$

$$T_6 = T_2 + T_{2a} + T_{6,EM} = \frac{T_{GT}}{4} \cdot \frac{z_2}{z_1} + \frac{T_{GT}}{4} \cdot \frac{z_{2a}}{z_{1a}} + \frac{T_{EM}}{2} \cdot \frac{z_6}{z_7} \tag{2.58}$$

For the calculation of the module of the second stage, the eq (2.58) is inserted in the eq. (2.52) and it represents the torque discharged at the wheel 6.

For the Architecture Off-Set H3, in Figure 2.9, the methodology is equal to previous cases, but the torque of wheal 6 is the following in eq. (2.59):

$$T_6 = T_2 + T_{2a} + T_{EM} = \frac{T_{GT}}{4} \cdot \frac{z_2}{z_1} + \frac{T_{GT}}{4} \cdot \frac{z_{2a}}{z_{1a}} + T_{EM} \tag{2.59}$$

In this case, the pinion of the second stage is too big, the system is not balanced from the point of view of torques and the mass of this wheel and the second stage in general is too high. This is a possible solution but not convenient. In addition to this, the EM is low-speed, therefore a lower efficiency given by the electric machine would be added.

At this point, all hybrid architectures of Off-Set layout are known and it is possible to move to hybrid In-Line architecture.

In reference to Figure 2.11 is possible to identify two layouts: Hybrid 1 and Hybrid 2.

In Hybrid 1 the EM is linked to the first crown of the first stage by its own pinion, so in this case, there is not a constrain on rotational speed between EM and GT because is managed by the gear ratio between Gas Turbine rotational speed and Electric Motor rotational speed.

Therefore, the balance of torques and powers, is sufficiently adding the power, eq. (2.60) of EM or the torque, eq(2.61)-(2.63), itself correct by the gear ratio.

$$P_{prop} = P_{EM} + P_{GT} \tag{2.60}$$

$$T_{prop} \cdot \omega_{c2} = T_{EM} \cdot \omega_1 + T_{GT} \cdot \omega_{s1} \tag{2.61}$$

$$T_{prop} \cdot \frac{\omega_{c2}}{\omega_{s1}} = T_{EM} \cdot \frac{\omega_1}{\omega_{s1}} + T_{GT} \tag{2.62}$$

$$T_{prop} = \left(T_{EM} \cdot \frac{z_2}{z_1} + T_{GT}\right) \cdot \left(1 + \frac{z_{r1}}{z_{s1}}\right) \cdot \left(1 + \frac{z_{r2}}{z_{s2}}\right) \tag{2.63}$$

Recalling Lewis's formula for calculating the gear ratio for an epicycloidal mechanism.

$$\frac{\omega_{s1}}{\omega_{c2}} = \left(1 + \frac{z_{r1}}{z_{s1}}\right) \cdot \left(1 + \frac{z_{r2}}{z_{s2}}\right) \quad \frac{\omega_1}{\omega_{s1}} = \frac{z_2}{z_1} \tag{2.64}$$

It is easy to see how the torque of EM gets in the gearbox correct by gear ratio and so, it is easy to think, that depending on this gear ratio is possible to boost the input torque by the Electric Motor. As you can see it is also possible to use a high-speed EM with a higher efficiency than Hybrid 2. However, the cons of this architecture are: firstly is not possible to increase without limiting the gear ratio between z_2 and z_1 (the pinion mass varies with the variation of this ratio) and secondly the system is not balanced.

Rather, if it analyses the second possibility, Hybrid 2, is true that it must use a lower-speed Electric Motor (for constraints sizing on the second stage), but it is possible to not add the other two wheels. Moreover, the electric motor torque is discharged directly in the sun s_2 of the second stage, eq.(2.65), and, only in the transitory, a quota is used to accelerate the carrier c_1 of the first stage.

$$T_{prop} = \left[T_{GT} \cdot \left(1 + \frac{z_{r1}}{z_{s1}}\right) + T_{EM}\right] \cdot \left(1 + \frac{z_{r2}}{z_{s2}}\right) \tag{2.65}$$

In conclusion, the torque on the first sun s_1 is equal for both conventional and hybrid propulsion, eq.(2.39) (2.41), while for the second stage it is possible to use the eq.(2.65) into eq.(2.40) and (2.42).

For the sizing of carriers, of the first and second stages, the methodology is equal to both conventional and hybrid.

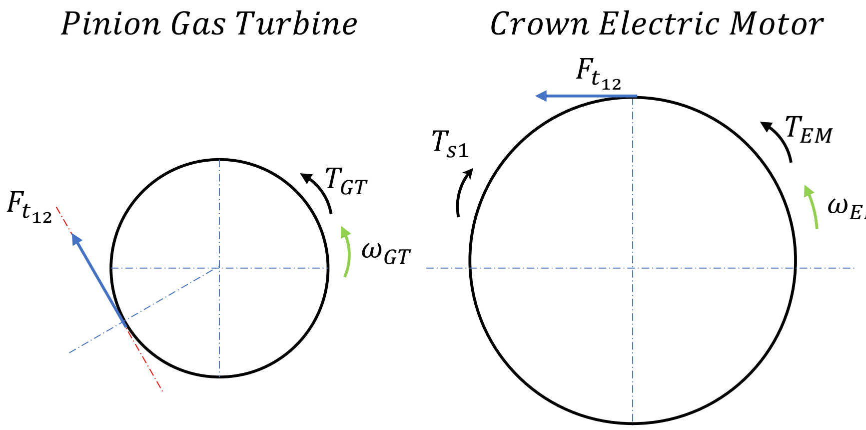

Figure 2.29: Force in Mixed Hybrid Architecture in the First Meshing

In the end, the Mixed Hybrid Layout is represented in Figure 2.12.

In Option 1 the EM torque is discharged in the first meshing of the first stage, namely the pinion sees only the torque of GT while the crown sees the force given by the meshing between the meshing pinion-crown with the addition of the torque given by EM (Figure 2.29).

So in this case it use eq. (2.1) twice to determine the maximum ratio of torque to tooth number.

$$T_{s1} = T_{GT} \cdot \frac{\omega_1}{\omega_2} + T_{EM} \quad \tau_{12} = \frac{z_2}{z_1} = \frac{\omega_1}{\omega_2} \tag{2.66}$$

In Option 2 the free body diagram is analogue to Figure 2.29 but the torque of EM is directly discharged in the second stage, that is in the first planetary stage by a splined shaft by eq (2.66).

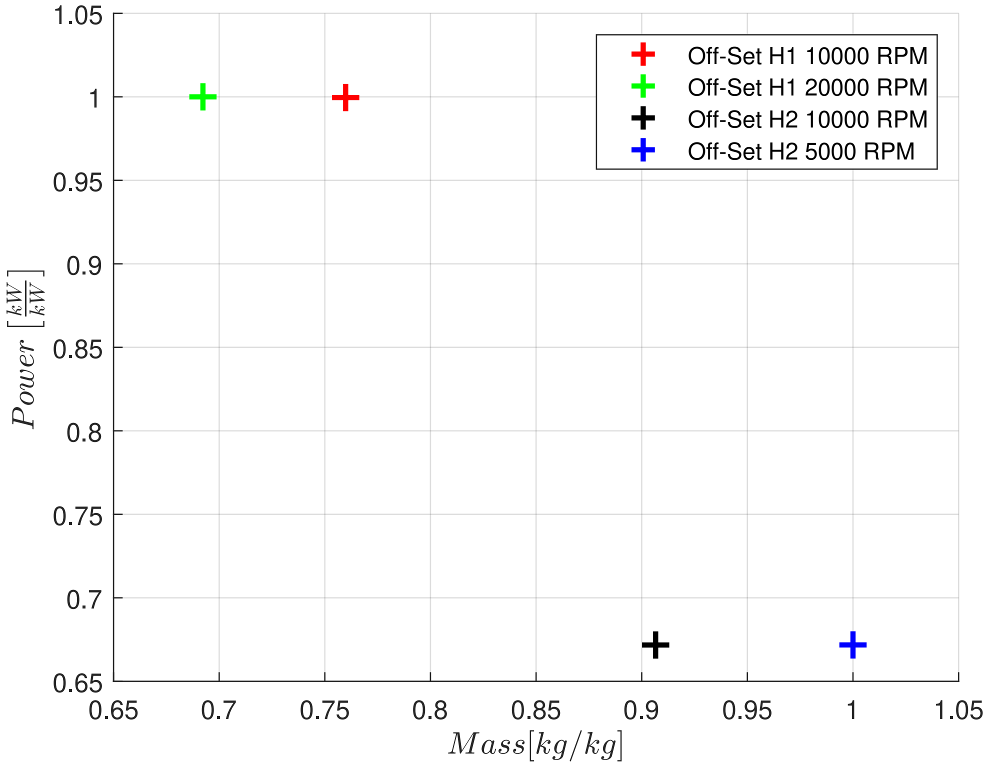

Figure 2.30: Comparison between combined Gearboxes of Off-Set Architecture H1 and H2

In conclusion, by Figure 2.30, it is possible to see four cases that concern the first and the second type of combined gearbox of Off-Set Architecture. The first two points, green and red, represent the combined Gearbox with high-speed EM, while the other two, black and blue, represent the same cGB but with low-speed EM.

There are some points to notice:

- Combined Gearboxes with the lower rotational speed of EM are heavier than the other two by about 53 per cent

- The Off-Set H2 5000 RPM (blue) is heavier than Off-Set H2 10000 RPM by around 10 per cent
- The Off-Set H1 20000 RPM (green) is lighter and more powerful than all
- The green and the red have the same power installed and are more powerful of 35 per cent than black and blue architectures

By this is possible to add another conclusion:

- The higher the rotation speed of the electric motor, the greater the weight savings, for both four cases (green respect to red and black respect to blue)
- The choice of the best solution between these layouts is the Off-Set H1 20000 RPM, namely that architecture which uses the high-speed electric motor

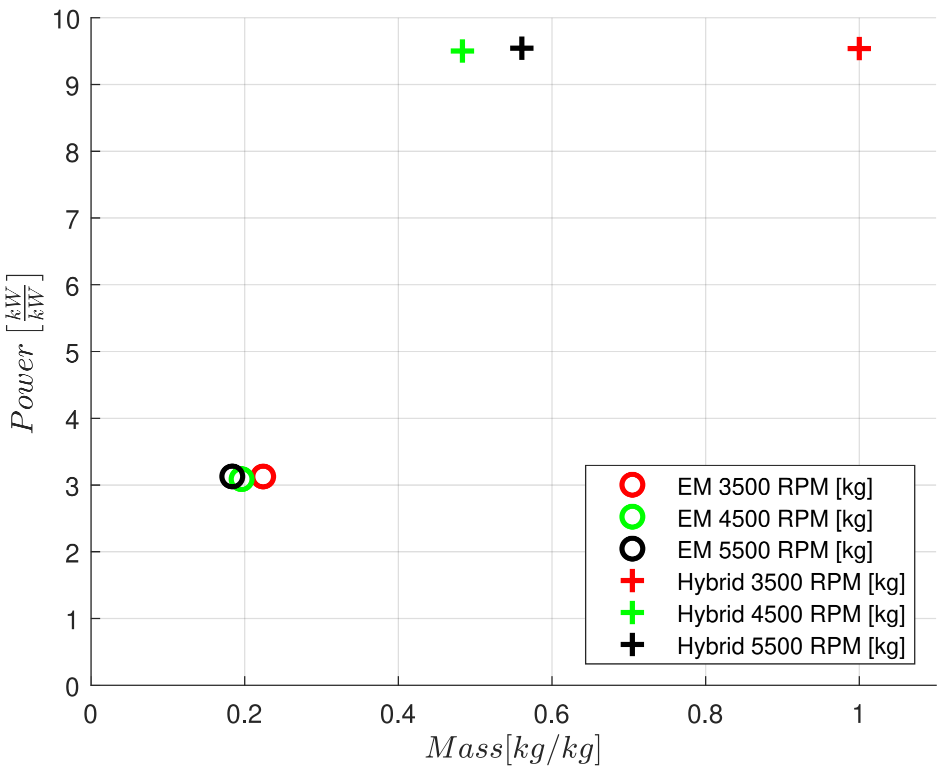

Figure 2.31: In-Line Architecture with difference rotational speeds of Electric Motor

If it is analyzed only the In-Line Architecture, in Figure 2.31, chosen as the best solution between all for combined Gearbox, it is possible to see how:

- A 2000 RPM difference between the lowest and the highest rotational speed doesn't give any difference in terms of mass for the only EM (circle point) (the power of the EM is fixed)
- The same difference in speed gives a difference, in terms of mass, for the total system (cross point).
- The cGB that uses an EM with a mean rotational speed (4500 RPM - green cross) is the best in terms of mass and power, i.e. lowest mass and maximum power.
- Hybrid 4500 RPM (green cross) is lighter by 22 per cent than Hybrid 5500 RPM and by 55 per cent lighter than Hybrid 3500 RPM
- The mass of the Electric Motor alone weighs around 30 per cent of the total of the hybrid architecture between all cases

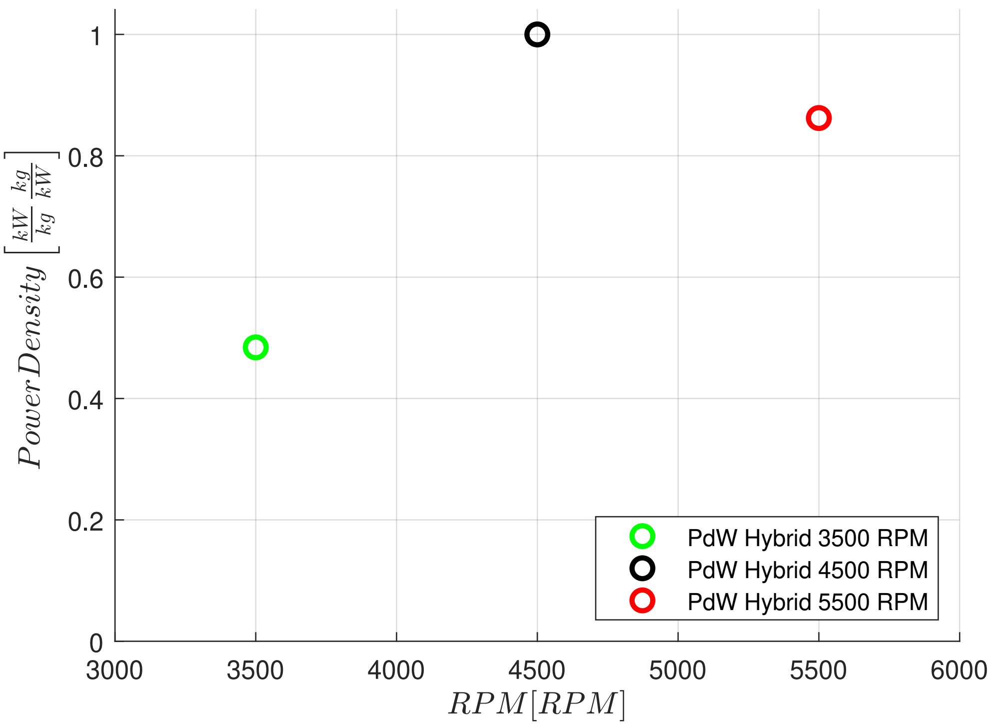

Figure 2.32: Power Density depending on the rotational speed of the Electric Motor

Another difference that it is possible to see is the power density trend in the function of the speed of the EM in Figure 2.32.

In this case, the higher value has the minimum of mass. In other words, the Hybrid 4500 RPM is lighter by 55 per cent than the Hybrid 3500 RPM and 18 per cent power density between all is the Hybrid 4500 RPM, so near this range of speed there is the In-Line Hybrid Architecture with the maximum of power than the Hybrid 5500 PRM. Add to this, to calculate how changing the power density on depending RPM with a fixed pitch of 100 RPM, it is possible to see Figure 2.33.

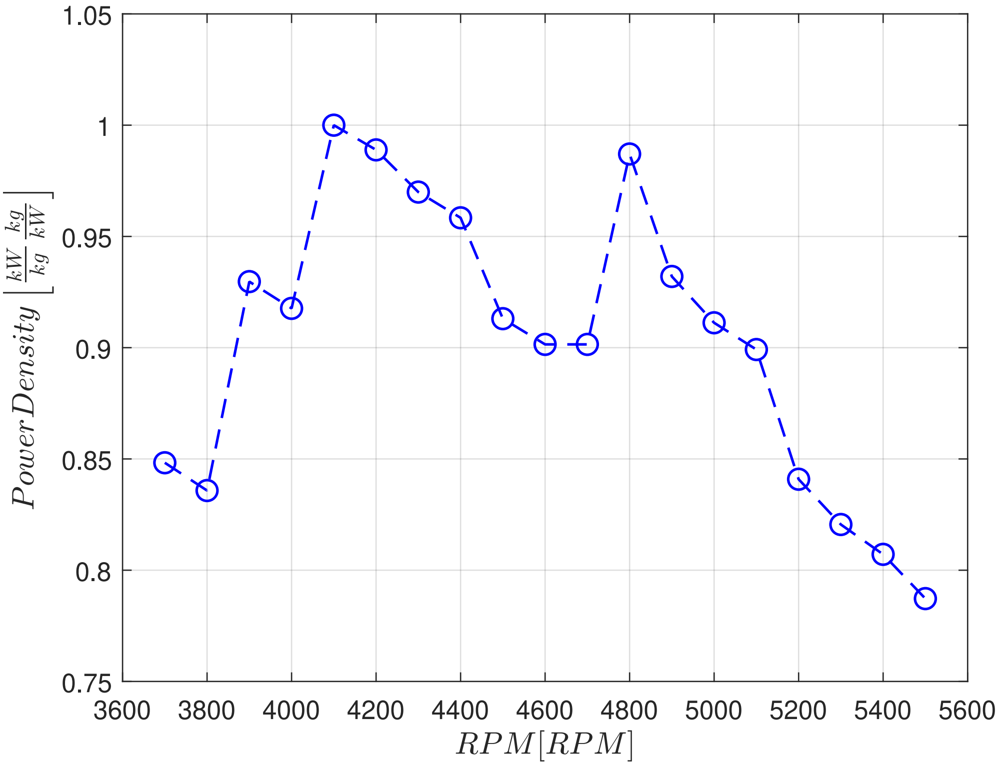

Figure 2.33: Power Density Trend

In this Figure 2.33 is plotted the trend of Power Density depending on the rotational speed of EM. As you can see the best point, the highest, it's not at 4500 RPM but slightly before at around 4100 RPM. Despite this, if you operate the EM at 4500 RPM the difference in power density between this point and the point at 4100 RPM is 5 per cent less. In Figure 2.33 for the highest rotational speed of the carrier of the first stage, the power density decreases significantly and this happens because the rotational speed of the sun s_2 increases and so as a consequence the gear ratio of the second stage must be increased. If it uses a higher gear ratio of the second stage means that, as the first hypothesis, the diameter of the ring r_2 will increase or the diameter of the sun s_2 will decrease. In both cases, the mass in the second stage increases and consequently, the power density decreases.

Chapter 3

Dynamic Model

At this point it is possible to do a dynamic analysis of the transmission (Matlab/Simullink Software), which means, in general terms, understanding the response of the gearbox depending on the phase of the flight mission.

The methodology used is similar to earlier works [31]-[32], but in this case is applied to a different system (double reduction stage of hybrid planetary transmission)

As anticipated, there are some hypotheses following:

- Elastodynamic analysis
- Model with concentrated parameters
- Radial geometry carrier mass purely rotational [33]

If it talks about an elastodynamics model with concentrated parameters then you must define the inertia of rotational components, shaft and gears, and the stiffness and damping factors.

In conclusion, an elastodynamics model is an analogue to a spring-damper system for both shafts and gears in eq.(3.1) or in rotational coordinates in eq.(3.2)

$$F_i = K_{eq} \cdot \Delta x + c\dot{x} \tag{3.1}$$

$$F_i = K_{eq} \cdot \Delta \theta + c\dot{\theta} \tag{3.2}$$

To this is added, in the third hypothesis, a radial geometry carrier mass purely rotational [33] and this introduces some advantages:

- Effects of revolution not considered (only rotational effects)

- Fewer dynamic motion equations and so a lower degree of freedom for the system (5 for the first carrier, given by rotational of sun, rotation of three planets and rotation of carrier, and 7 for the second carrier)
- Computational cost reduced

and disadvantages:

- All translation effects, like as bearing force and reaction, are neglected.

This model uses a variable stiffness of meshing (k_{eq}) and this represents the stiffness between the force of gearing and the teeth $[N/(m \cdot rad)]$. In this work, this parameter is taken firstly constant [34] to all contact lines between teeth and after variable [33]-[35] always along the same contact line.

3.1 General Model Implementation - Inertia and Stiffness

To the calculate inertia of the transmission, it is assumed that the gears are similar to a disk with a constant mass distribution. That said it is possible to write eq. (3.3) (3.4) and (3.5) for the gear's mass of the first stage and eq. (3.6)(3.7) and (3.8) for the moment of inertia the same stage.

$$m_{s1} = \pi r_{s1}^2 \cdot b_{s1} \cdot \rho \tag{3.3}$$

$$m_{pl,i} = \pi r_{pl,i}^2 \cdot b_{pl,i} \cdot \rho \tag{3.4}$$

The mass is equal to all planets, so:

$$m_{pl,I} = m_{pl,11} = m_{pl,12} = m_{pl,13} \tag{3.5}$$

$$I_{s1} = \frac{1}{2} m_{s1} r_{s1}^2 \tag{3.6}$$

$$I_{pl,i} = \frac{1}{2} m_{pl,i} r_{pl,i}^2 \tag{3.7}$$

The inertia's moment is equal to all planets, so:

$$I_{pl,I} = I_{pl,11} = I_{pl,12} = I_{pl,13} \tag{3.8}$$

The same methodology is used for the mass of the second stage but repeated for five planets in eq.(3.9)

$$\begin{aligned} &m_{s2} = \pi r_{s2}^2 \cdot b_{s2} \cdot \rho \\ &m_{pl,II} = m_{pl,21} = m_{pl,22} = m_{pl,23} = m_{pl,24} = m_{pl,25} \end{aligned} \tag{3.9}$$

and for the moment of inertia in eq.(3.10).

$$\begin{aligned} &I_{s2} = \frac{1}{2} m_{s2} r_{s2}^2 \\ &I_{pl,II} = I_{pl,21} = I_{pl,22} = I_{pl,23} = I_{pl,24} = I_{pl,25} \end{aligned} \tag{3.10}$$

For the inertia of the carrier, for the first and second stages, is used a formula in eq.(3.11) [36] in which the inertia of the carrier depends on the number of planets, the gear ratio, the dimension of the suns and satellites. This model is based on the hypothesis that the mass of the carrier is concentrated in the centre of the carrier itself.

$$I_{C,i} = \frac{4.5 \cdot \pi}{256 \cdot \tau_i^2} \cdot n_{pl,i} \cdot b_i \cdot d_{s,i}^2 \cdot (d_{s,i} + d_{pl,i})^2 \tag{3.11}$$

In which:

- with $i = 1$ for the first stage and $i = 2$ for the second stage
- τ_i is the gear ratio of the stage (> 1) $\tau_i = \omega_{s,i}/\omega_{c,i}$
- $n_{pl,i}$ is the number of planets, three for the first stage and five for the second

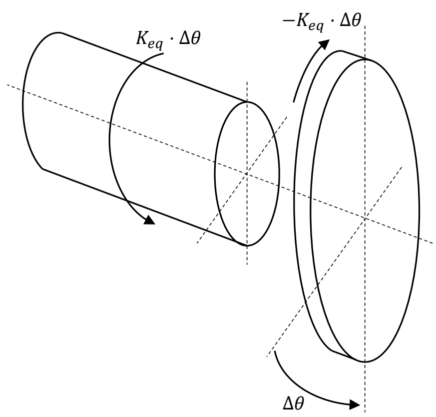

Figure 3.1: Torsional stiffness of a general shaft

Regarding the torsional stiffness in Figure 3.1 is possible to write a general rotational stiffness of the shaft in eq. (3.12) and after can be used to calculate the stiffness of the transmission shafts for the GT, the EM and the carriers.

$$K_{eq,i} = \pi \cdot G \cdot \frac{d^4_{shaft,i}}{32 \cdot L_{shaft,i}} \tag{3.12}$$

To continue, this parameter is used to calculate the damping factor in that this depends on stiffness in eq. (3.12), the mass of the shafts and a *eps* reported by the eq. (3.13)

$$c_{shaft,i} = 2 \cdot eps \cdot \sqrt{K_{eq,i} \cdot m_{shaft,i}} \tag{3.13}$$

In which:

- $L_{shaft,i}$ is the length of the considered shaft in this case in $[mm]$
- $d_{shaft,i}$ is the diameter of the considered shaft in this case in $[mm]$
- G tangential modulus of elasticity in $[GPa]$
- eps is a damping factor equal to 0.1 $[-]$

In conclusion of this part, it is possible to see that:

- an increase of the diameter of the shafts and decrease the length produce an increase in the stiffness factor and damping factor, so the system results faster with an increase of K_{eq} and more damped with an increase of $c_{shaft,i}$.
- To obtain a still more damped system it is possible to increase *eps* from 0.1 to 0.2.

Now is possible to calculate the stiffness and damping factors for the gas turbine, in eq.(3.14) and eq.(3.15)

$$K_{GT} = \frac{\pi \cdot G \cdot d^4_{GT}}{32 * l_{GT,shaft}} \tag{3.14}$$

$$c_{GT} = 2 \cdot eps \cdot \sqrt{K_{GT} \cdot m_{GT,shaft}} \tag{3.15}$$

and electric motor shafts, in eq.(3.16) and eq.(3.17)

$$K_{EM} = \frac{\pi \cdot G \cdot d^4_{EM}}{32 * l_{EM,shaft}} \tag{3.16}$$

$$c_{EM} = 2 \cdot eps \cdot \sqrt{K_{EM} \cdot m_{EM,shaft}} \tag{3.17}$$

It is now possible to define how the first gear stiffness proposed by Kuang and Yang [34] was calculated, in which post Finite Element Analysis (FEA) stiffness was obtained for straight tooth gears in eq.(3.18). For simplicity, the equations used for the calculation of the various parameters in order to determine the stiffness of the mesh.

$$K_i(r_i) = 10^9 \cdot (A_0 + A_1 \cdot X_i) + (A_2 + A_3 \cdot X_i) \cdot \frac{r_i - R_i}{(1 - x_i) \cdot m} \tag{3.18}$$

In which:

- A_0,A_1,A_2,A_3 are parameters that depend on number of teeth $A_i = f(z_i^3)$ in ed.(3.20) to (3.22)
- r_i is the radius relative to the position of the load $[mm]$
- R_i is the pitch radius $[mm]$
- m is the normal module of the teeth $[mm]$
- X_i coefficient of displacement of the tooth profile, for wheels with correct toothing (in this case $X_i = 0$)

$$A_0 = 3.867 + 1.612 \cdot z_i - 0.02916 \cdot z_i^2 + 0.0001553 \cdot z_i^3 \tag{3.19}$$

$$A_1 = 17.060 + 0.7289 \cdot z_i - 0.01728 \cdot z_i^2 + 0.00009993 \cdot z_i^3 \tag{3.20}$$

$$A_2 = 2.637 - 1.222 \cdot z_i + 0.02217 \cdot z_i^2 - 0.0001179 \cdot z_i^3 \tag{3.21}$$

$$A_3 = -6.330 - 1.033 \cdot z_i + 0.0.2068 \cdot z_i^2 - 0.0001179 \cdot z_i^3 \tag{3.22}$$

Now is possible to calculate the stiffness factor for the sun and the planets of the first stage $K_{s,i}$, $K_{p,ij}$, eq.(3.18) and eq.(3.19) (with i = 1,2 to indicate the stage and $j = 1, ..., N_{p,i}$). This procedure is repeated to determine the factors of the second stage of reduction ($i = 2$, $j = 1, ..., N_{p2}$).

$$K_c = \frac{K_1 \cdot K_2}{K_1 + K_2} \tag{3.23}$$

All these parameters represent the bending stiffness of the single teeth of that gear, therefore to calculate the bending stiffness of the gear mesh it is assumed that the gear teeth are similar to two springs put in series according to the eq.(3.23).

Through this equation (3.23) is possible to get at following equations (3.24) to (3.25)

$$K_{c1,s1p11} = \frac{K_{s1} \cdot K_{p11}}{K_{s1} + K_{p11}} \tag{3.24}$$

$$K_{c1,p11r1} = \frac{K_{r1} \cdot K_{p11}}{K_{r1} + K_{p11}} \tag{3.25}$$

By which by eq. (3.24) is possible to extend to all three planets of the first stage, but the stiffness factors are equal between them because the geometric parameters of all planets are the same for all. And, for the same reason, this applies also to eq. (3.25), i.e. for the contact between the planet and the ring.

$$K_c^{eq} = K_c = \sum_{i=1}^{N_{p,i}} K_{c,i} \tag{3.26}$$

$$K_{sp} = (0.75 \cdot \varepsilon + 0.25) \cdot K_c \cdot b_{s,i} \tag{3.27}$$

$$K_{rp} = (0.75 \cdot \varepsilon + 0.25) \cdot K_c \cdot b_{r,i} \tag{3.28}$$

Subsequently, the general equivalent stiffness is obtained by eq.(3.26); the stiffness of the gear mesh between sun and planets and between ring and planets are obtained by eq.(3.27)(3.28).

From this, the equivalent meshing damping is calculated for sun-planet gearing in eq.(3.29) and for planet-ring gearing in eq.(3.30).

$$c_{sp} = 2 \cdot eps \cdot \sqrt{\frac{K_{sp} \cdot mass_{s,i} \cdot mass_{pl,i}}{mass_{s,i} + mass_{pl,i}}} \tag{3.29}$$

$$c_{pr} = 2 \cdot eps \cdot \sqrt{K_{rp} \cdot mass_{pl,i}} \tag{3.30}$$

With $eps = 0.1$ is the damping ratio of meshing gear [32].

It is also possible to use a variable stiffness [32] where a Fourier series is used to model the contact between the various gear teeth. This stiffness takes into account a frequency of meshing and a delay of contact because the various planets do not mesh with the solar and the ring all at the same time.

To support this there will be delays that take into account solar-plant contact (γ_{sp}) and planet-ring contact (γ_{pr}) reported in eq.(3.31)(3.32).

$$\gamma_{sp} = \pm \frac{z_{sun,i} \cdot \Psi}{2 \cdot \pi} \tag{3.31}$$

$$\gamma_{rp} = \pm \frac{z_{ring,i} \cdot \Psi}{2 \cdot \pi} \tag{3.32}$$

$$\Psi_i = p_{n,i} \cdot \frac{2 \cdot \pi}{z_{ring,i} \cdot z_{sun,i}} + \phi_i = \Psi_{i-1} + \phi_i \tag{3.33}$$

$$\phi_i = \phi_{i-1} + 360/(N_{p,i} - 1) \tag{3.34}$$

In which:

- $z_{sun,i}$ and $z_{ring,i}$ represent the number of solar and ring teeth in that phase of reduction ($i = 1, ...,2$) in which the positive values are for hourly rotations of the for γ_{sp} and counterclockwise for γ_{rp}, while for negative values rotations reverse;
- $p_{n,i}$ is the wheelbase in that stage of reduction ($i = 1, ...,2$);
- ϕ_i represents the angle that takes into account the initial position of that given planet, according to the eq.(3.34) with $i = (0, ..., N_p + 1)$

Now according to the equations (3.35) and (3.36) it is possible to calculate the various gear stiffness for each wheel for each stage with $j = 1, ...,2$ and $i = 1, ..., N_{p,j}$.

$$\begin{aligned} K_{s_j,p_{ji}} = K_{sp} + \frac{2 \cdot \left(\frac{K_{sp}}{2}\right)}{\pi} \cdot sin\left(\omega_{m,j} \cdot (t - \gamma_{s_j,p_{ji}} \cdot T_{m,j})\right) + \\ + \frac{2 \cdot \left(\frac{K_{sp}}{2}\right)}{3\pi} \cdot sin\left(3 \cdot \omega_{m,j} \cdot (t - \gamma_{s_j,p_{ji}} \cdot T_m\right) + \\ + \frac{2 \cdot \left(\frac{K_{sp}}{2}\right)}{5\pi} \cdot sin\left(5 \cdot \omega_{m,j} \cdot (t - \gamma_{s_j,p_{ji}} \cdot T_m\right) \end{aligned} \tag{3.35}$$

$$\begin{aligned} K_{r_j,p_{ji}} = K_{rp} + \frac{2 \cdot \left(\frac{K_{rp}}{2}\right)}{\pi} \cdot sin\left(\omega_{m,j} \cdot (t - \gamma_{r_j,p_{ji}} \cdot T_{m,j})\right) + \\ + \frac{2 \cdot \left(\frac{K_{rp}}{2}\right)}{3\pi} \cdot sin\left(3 \cdot \omega_{m,j} \cdot (t - \gamma_{r_j,p_{ji}} \cdot T_m\right) + \\ + \frac{2 \cdot \left(\frac{K_{rp}}{2}\right)}{5\pi} \cdot sin\left(5 \cdot \omega_{m,j} \cdot (t - \gamma_{r_j,p_{ji}} \cdot T_m\right) \end{aligned} \tag{3.36}$$

Whereas eq. (3.35) and (3.36) are added (3.37),(3.38),(3.39) and (3.40).

$$\omega_{m,j} = 2\pi \cdot f_{m,j} \tag{3.37}$$

$$f_{m,j} = f_{s,j} \cdot \frac{z_{s,j} \cdot z_{r,j}}{z_{s,j} + z_{r,j}} \tag{3.38}$$

$$f_{s,j} = \frac{\omega_{s,j}}{2\pi} \tag{3.39}$$

$$T_{m,j} = \frac{1}{f_{m,j}} \tag{3.40}$$

Which represent:

- the variable stiffness in function of the frequency of meshing between solar-planet ($K_{s_j,p_{ji}}$) and planet-ring ($K_{r_j,p_{ji}}$);
- the speed of rotation of meshing ($\omega_{m,j}$);
- meshing frequency ($f_{m,j}$);
- solar meshing frequency ($f_{s,j}$),that it depend on the rotational speed of the sun-gear, where j indicates the first or second stage;
- meshing period equal to reciprocal of meshing freqeuncy (f_m).

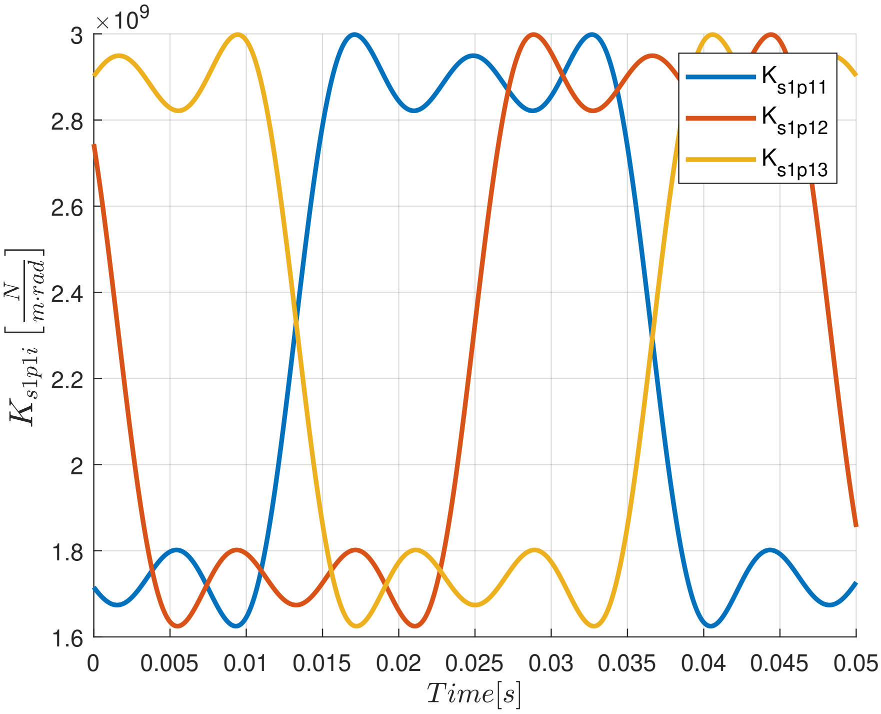

Figure 3.2: Variable solar-planet meshing stiffness as a function of frequency - First Stage

The Figure 3.2 describes the meshing gear trend between solar and planet gears. The lower value indicates a single meshing between two gear wheels, while a higher value indicates a double meshing between two gear wheels.

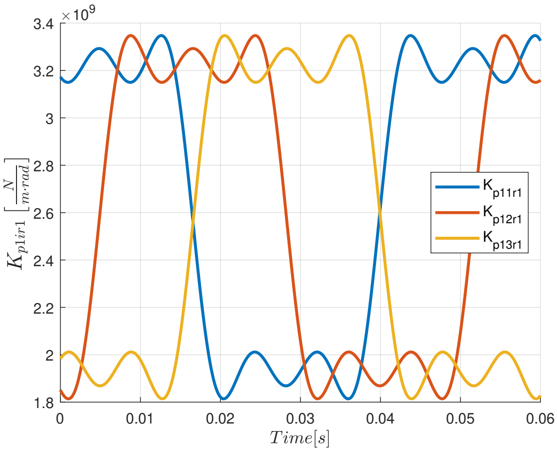

Figure 3.3: Variable planet-ring meshing stiffness as a function of frequency - First Stage

Figure 3.3 describes the meshing between planets and ring of the first reduction stage. The considerations are similar to the previous Figure 3.2. In addition to this, it is possible to see how the trends between these two Figures 3.3 and 3.2 are similar to each other with the only difference in a time delay in x axis.

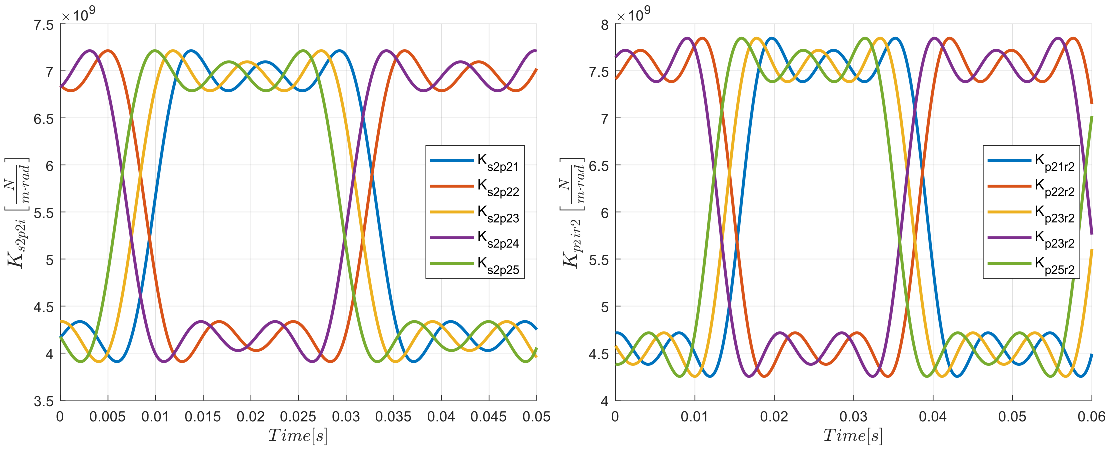

Figure 3.4: Variable sun-planets-ring meshing stiffness as a function of frequency - Second Stage

The considerations on the rigidity between the solar-planetary ring previously carried out with regard to Figures 3.2 and 3.3 are similar to those reported in Figure 3.4 with the difference in this case that there are 5 trends, one for each planetarium of the second stage.

3.2 Gearbox Model

Before going deep into the analysis of the gearbox, the single stage and the boundaries condition, a general view of the same gearbox will given with a more general approach in Figure 3.5. This means analyze the gearbox like a black box.

Moreover, all system is modelled in the following method, namely for each dynamic quantity in input the model gives a kinematic quantity in output and the other way round.

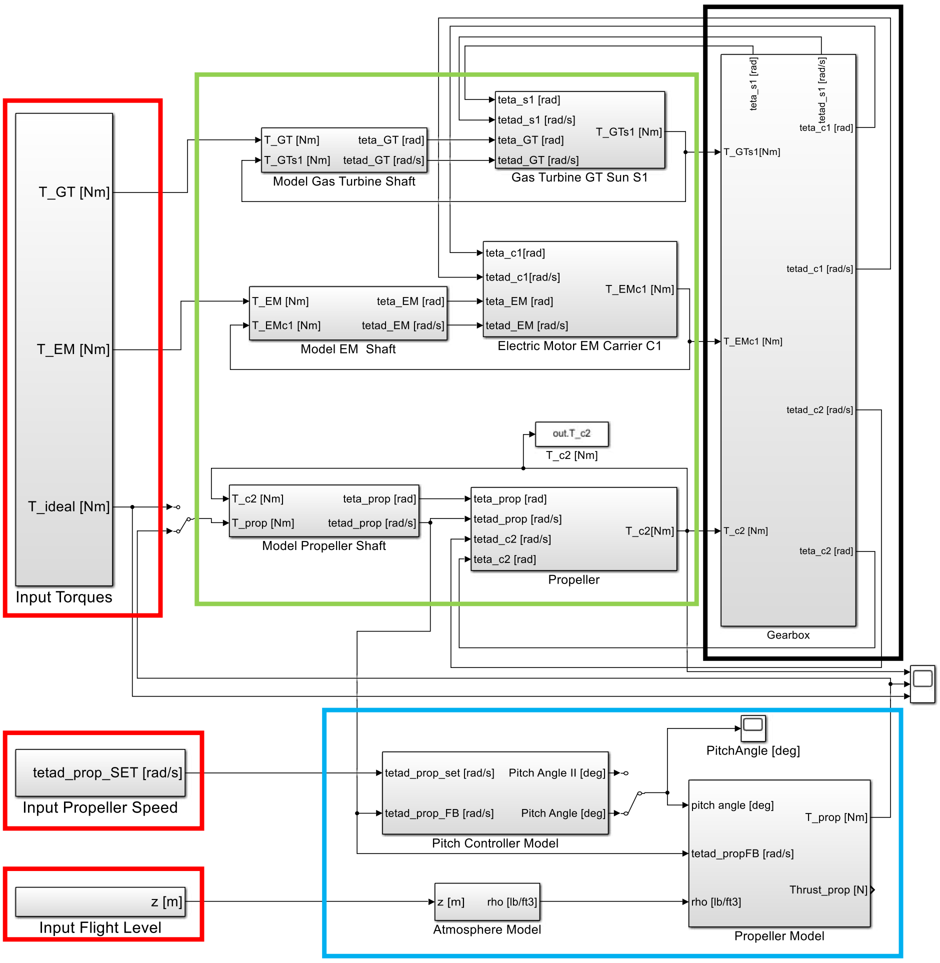

Figure 3.5: Simulink General Model

In this Figure 3.5 it is possible to see some blocks about the entire systems. In greater detail:

- The red blocks represent the variables input of all sub systems.

- The black block represents the core block of the thesis, that is the Gearbox Model. This block sees the input torques of the GT (T_{GTs1}), of the EM (T_{EMc1}) and the torque of the propeller shaft (T_{c2}) and gives output the angles and the rotational speeds of the solar gear and carrier of the first, θ_{s1}, $\dot{\theta}_{s1}$, θ_{c1} and $\dot{\theta}_{c1}$, and second stage, θ_{c2} and $\dot{\theta}_{c2}$.

- The light blue block represents the system of the "Pitch Controller Model", the "Atmosphere Model" and the "Fluidynamic Propeller Torque". In this case, the block named "Pitch Controller Model" gives a specific angle of pitch depended on an error between the set propeller speed and feedback propeller speed ($e_\omega = \omega_{prop,SET} - \omega_{prop,FB}$) in different cases, with a order model equal to one or two; a density in the US system depending on the altitude of the aircraft, for instance constant to cruise phase and linear for climb or takeoff, in the "Atmosphere Model"; and depending on all these parameters the fluid-dynamic propeller torque and thrust are obtained in the "Propeller Model" or named also "Fluidynamic Propeller Torque".

- The green blocks represent the model of the transmission shaft of the gas turbine, the electric motor and the propeller, and the torques transmitted between GT and sun s_1, between EM and carrier c_1 and between carrier c_2 and propeller in "Model Gas Turbine Shaft","Gas Turbine GT Sun S1","Model EM Shaft" and "Electric Motor EM Carrier C1".

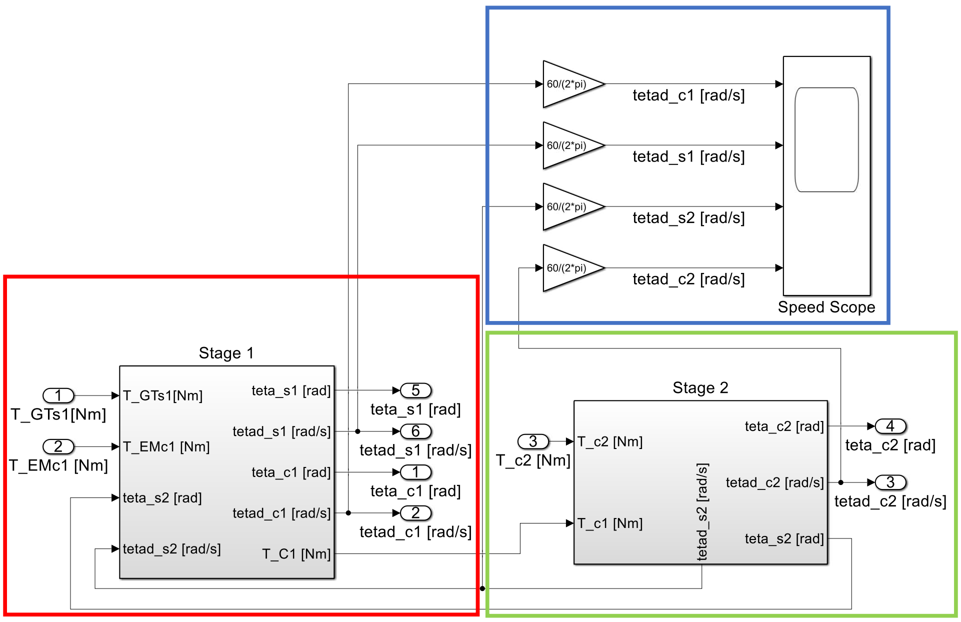

Figure 3.6: Simulink Model of the Stage 1 and Stage 2 of the Gearbox

Now, by referencing Figure 3.5, it is possible to pass a better analysis, block by block, in a detailed way at the black block "Gearbox" in Figure 3.6.

In Figure 3.6 it is possible to see:

- The red block to reference for the first stage of the reduction "Stage 1";
- the green block to reference for the second stage of the reduction "Stage 2";
- the block scope, "Speed Scope", to analyse that the steady speeds of the solar gear, $\dot{\theta}_{s1}$, and the carrier, $\dot{\theta}_{c1}$ and $\dot{\theta}_{c2}$, are appropriate to static sizing (in steady-state post-transitory).

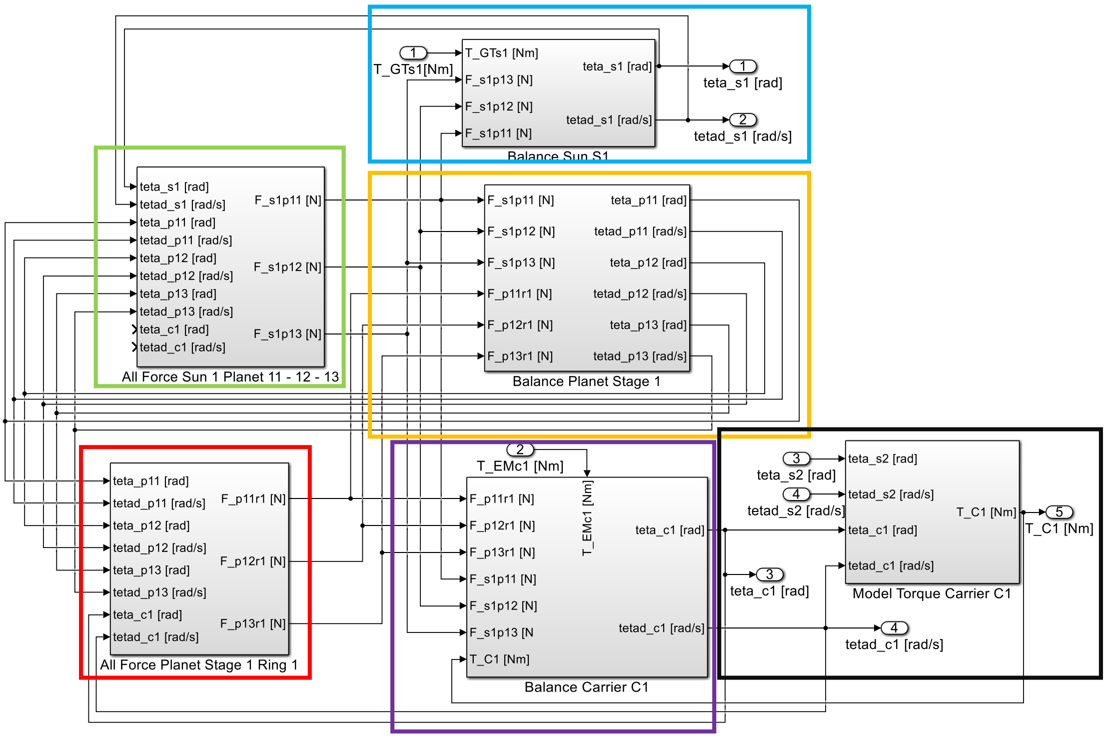

Figure 3.7: Simulink Model Stage 1 of the Gearbox

By this Figure 3.6 is now possible to analyse stage to stage the transmission, starting with "Stage 1" in Figure 3.7.

In Figure 3.7 there are balance blocks, the orange, "Balance Planet Stage 1", the light blue, "Balance Sun S1", and the violet, "Balance Carrier C1".

All these blocks will be deepened in the section 3.2.1 Shaft Model, while the red and the green blocks, "All Force Planet Stage 1 Ring 1" and "All Force Sun 1 Planet 11-12-13", will be deepened in 3.2.2 Gear Model.

The black block will give a definition when talking about the model of the GT and EM, always in the section refsubsection GearModel Gear Model.

In general when talking about "Balance" it means an equilibrium of the torque on that element (shaft) to calculate the angle of rotation of that object, in opposite when you don't read "Balance" then, in that block, the mesh gear force is modelled between planet gears and ring gear or between sun gear and planet gears.

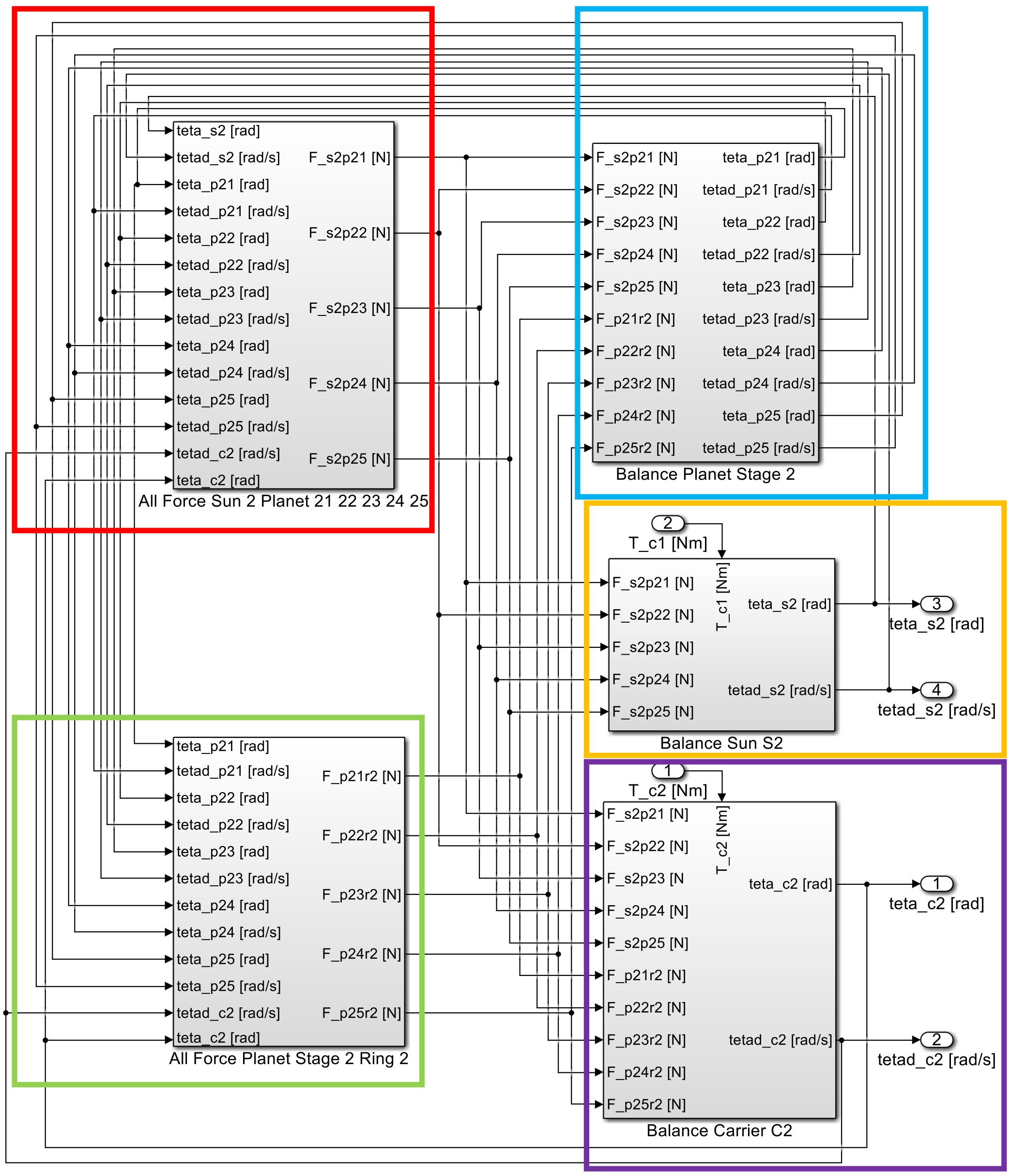

Figure 3.8: Simulink Model Stage 2 of the Gearbox

With reference to Figure 3.6, you individuate the block named "Stage 2" and this is reported in Figure 3.8 and the considerations done for Stage 1 are analogue to Stage 2.

The only difference between these subsystems are:

- the number of equations that depend on the number of planets for each stage;
- the not present black block named "Model Torque Carrier C1", Figure 3.7, in that this represents the link's block between the first and the second stage of reduction, namely the equation of the output torque of carrier c_1 and the input torque to sun s_2.

3.2.1 Shaft Model

At this point of the work, the information about the stage of reduction of the gearbox are sufficient and it is possible to to deepen the rotational equilibrium in this subsection, in other words, deepen the blocks named "Balance" for both stages of reduction.

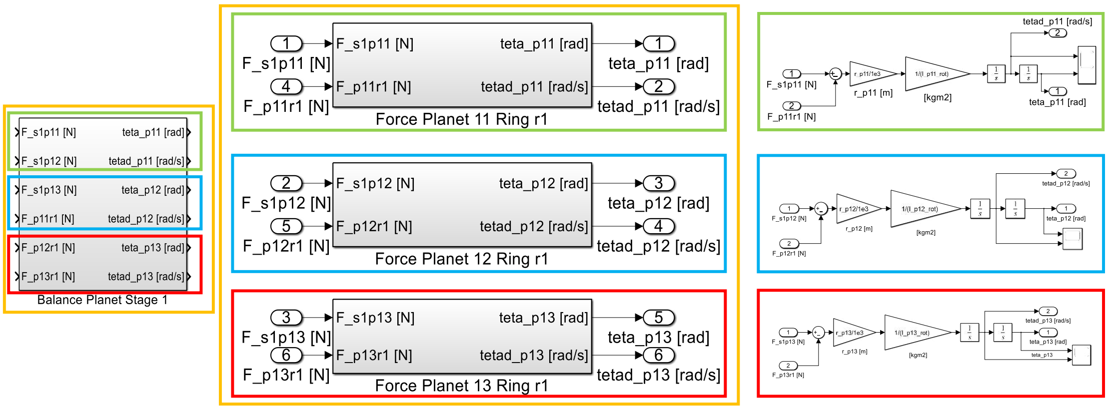

Figure 3.9: Simulink Balance Stage Planet 1

With reference to Figure 3.7, it is possible to analyse the orange block named "Balance Planet Stage 1" reported in Figure 3.9.

The orange rectangle contains the green, the light blue and the red rectangles which indicate the relative balance for each planet of the first stage of reduction. Add to this it is possible to see how the model is only rotational type in that there is no contribution of revolution's inertia of the planets.

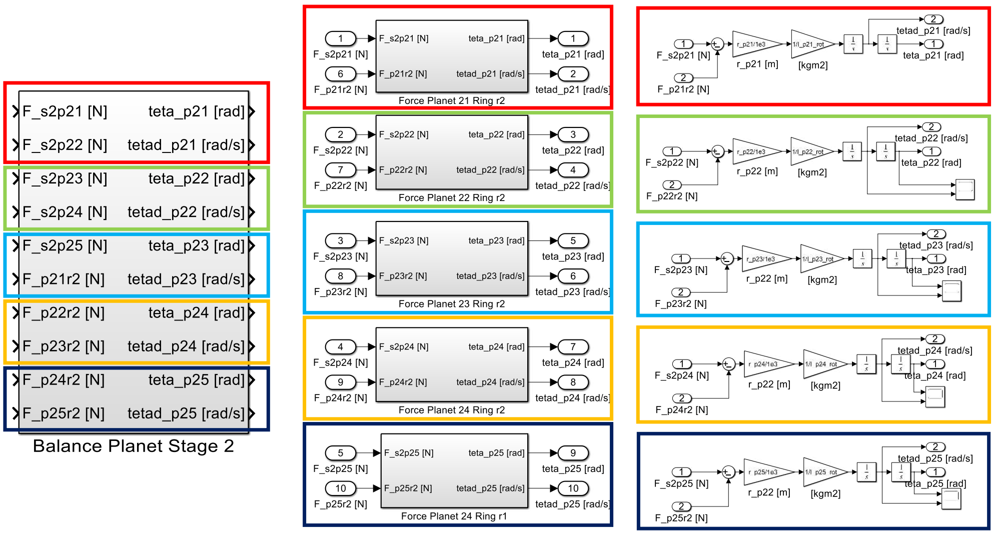

Figure 3.10: Simulink Balance Stage Planet 2

These considerations are analogues for the balance of the planets in the stage of reduction 2 reported in Figure 3.10.

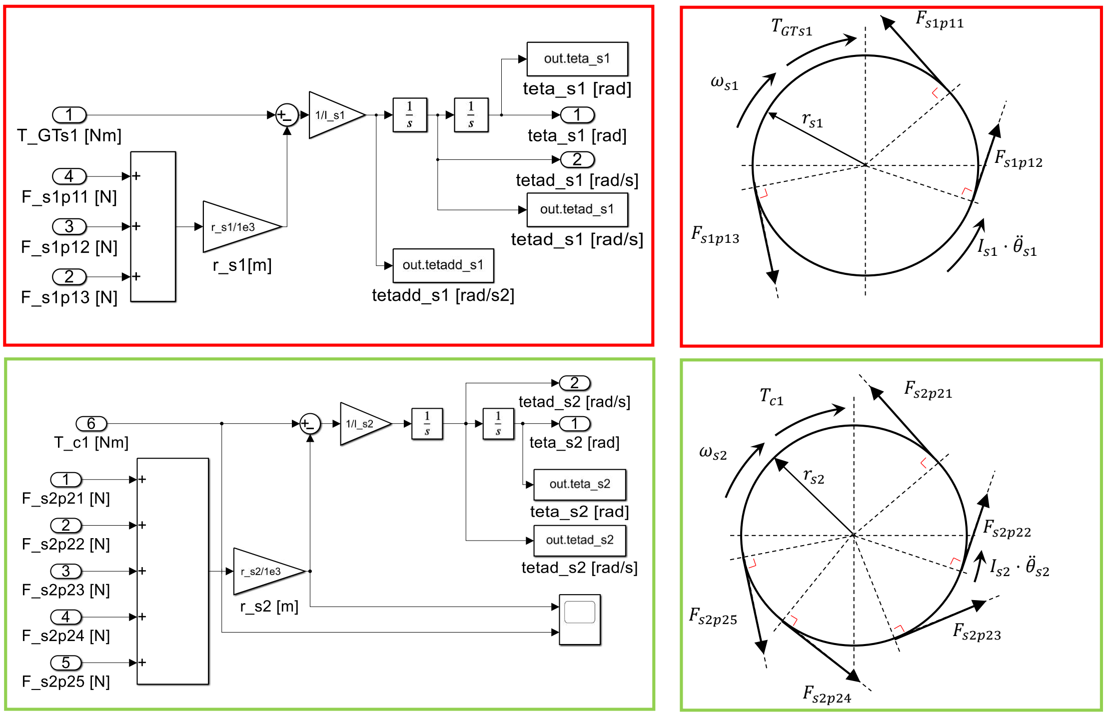

Figure 3.11: Simulink Balance Sun S1 and Balance Sun S2

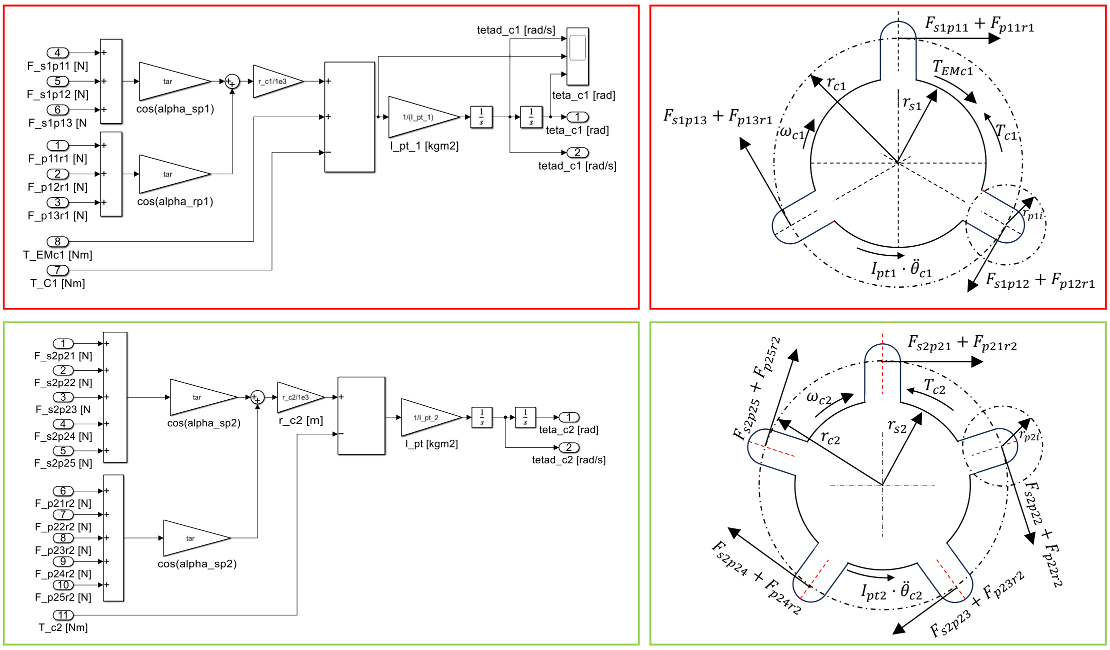

Figure 3.12: Simulink Balance Carrier C1 Balance Carrier C2

Now it's possible to analyse the balance of the sun s_i, Figure 3.11, and the carrier c_i, Figure 3.12, for the first, reed square with $i = 1$, and the second stage, green square with $i = 2$.

By comparing between Figure 3.11 and Figure 3.12 it is possible to see some differences:

- Figure 3.11 it is presents the contribution of the EM which, in the transitory phase, accelerates the carrier c_1 of the first stage and discharging torque in this element;
- Figure 3.12 is similar to the previous case, but in this case, the contribution of the EM is zero;
- in both cases, the forces of the carrier are the sum of the contact's force between the sun and the planets and the planets and the ring.

3.2.2 Gear Model

At this point, from the analysis of the light blue, orange and violet squares of Figure 3.7 and Figure 3.8. Now you can analyse the patterns of the meshing forces within the other blocks.

Before passing on how the forces are been modelled is opportune to explicate the theory on the base.

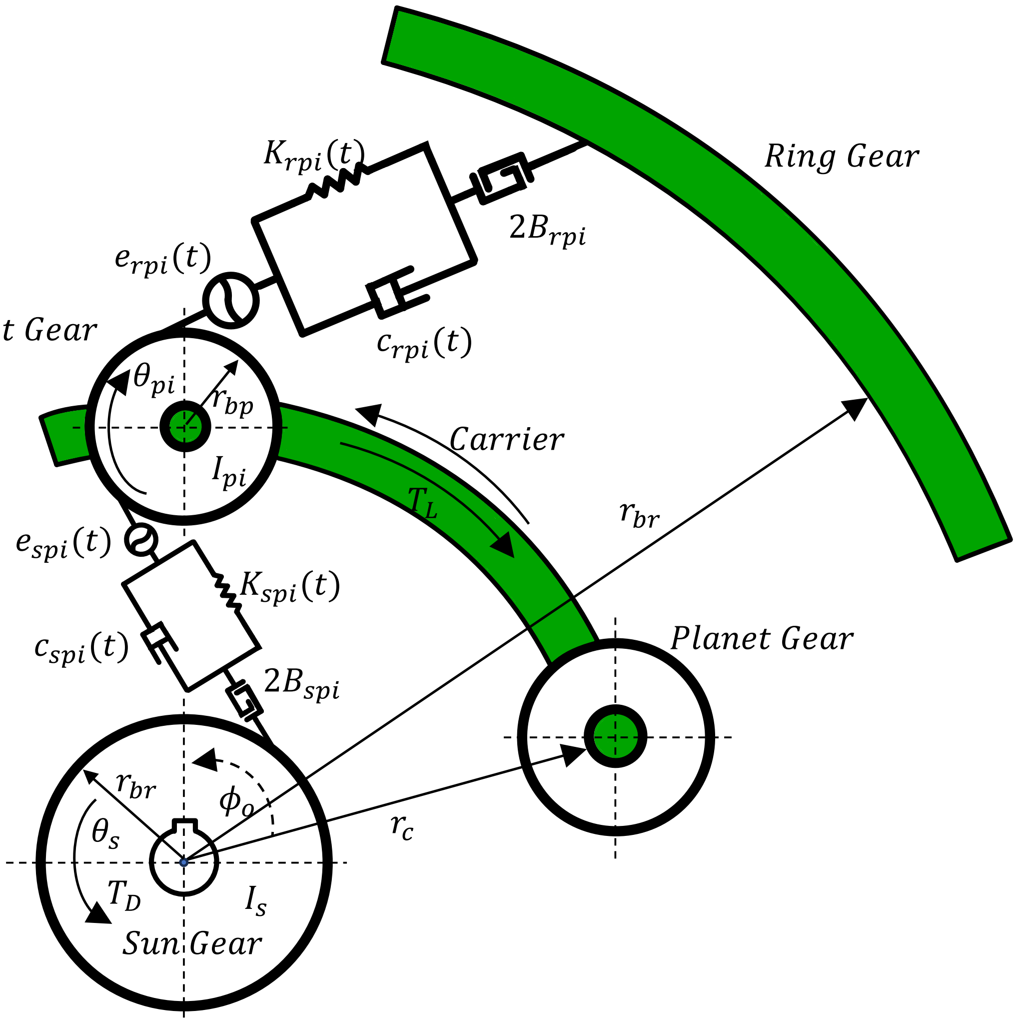

Figure 3.13: Mathematical Model of Planetary Transmission [33]

For the dynamic model of the planetary gearbox has been used a mathematical model considered as a contribution to the only rotation of the planet while revolution has been neglected , Figure 3.13 [33].

This model is used to analyse a double stage of reduction of a planetary combined gearbox which has three planets in the first stage and five stages in the second stage with an Electric Motor linked in the carrier of the first stage that discharges the torque to the sun gear s_2. In addition, there are five degrees of freedom in the first stage, the rotation of the sun, the rotation of the three planets and the rotation of the carrier c_1, and seven degrees of freedom in the second stage, which means the rotation of the sun s_2, the rotation of five planets and the rotation of the carrier c_2, linked to propeller's shaft. In addition, both ring gears for the two stages are fixed, so as to maximize the transmission ratio per single stage.

In this model, as anticipated, the effect of planet revolution is neglected and, although this means making an approximation because the forces on the bearings and therefore the forces on the housing are neglected, This allows you to use a simpler model with lower computational costs.

Also, given that the model offers a display of the temporal evolution of the forces, torques and speeds, it is possible to obtain the time in which the forces or torques get to the top and then give information about what the max value to take in consideration for the fatigue check or other checks for the cGB or for the housing and bearings in the second analysis.

In summary, you have:

- all stiffness of gear gearing constant between the sun and planets and the planets and the ring in the same stage;
- all damping factors equal and constant between the sun and planets and the planets and the ring in the same stage;
- meshing error neglected $e_{sp,i}(t) \simeq e_{rp,i}(t) \simeq 0$.

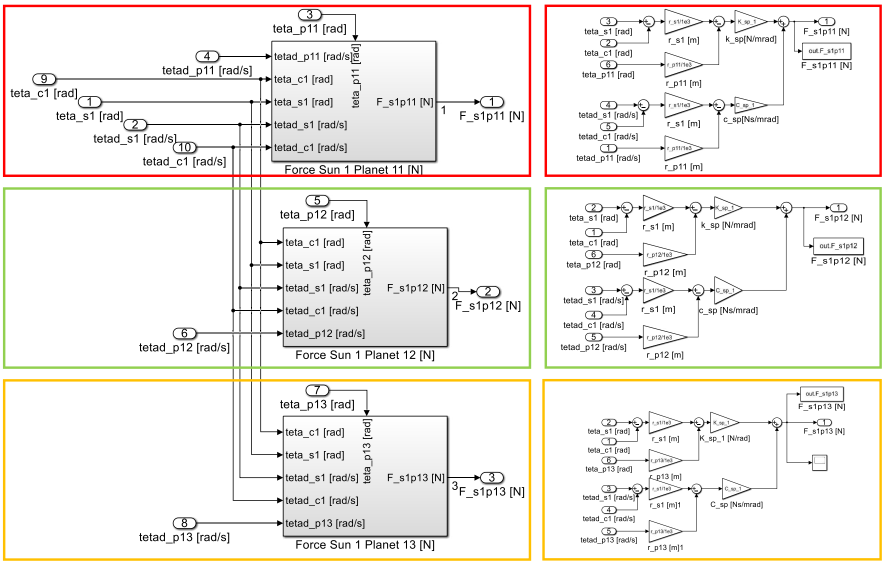

Figure 3.14: Simulink All Force Sun 1 Planet I

By referencing Figure 3.7 and Figure 3.8, for both inside the green block "All Force Sun 1 Planet 11-12-13" and "All Force Planet Stage 2 Ring 2" Figure 3.14 and Figure 3.15 are obtained.

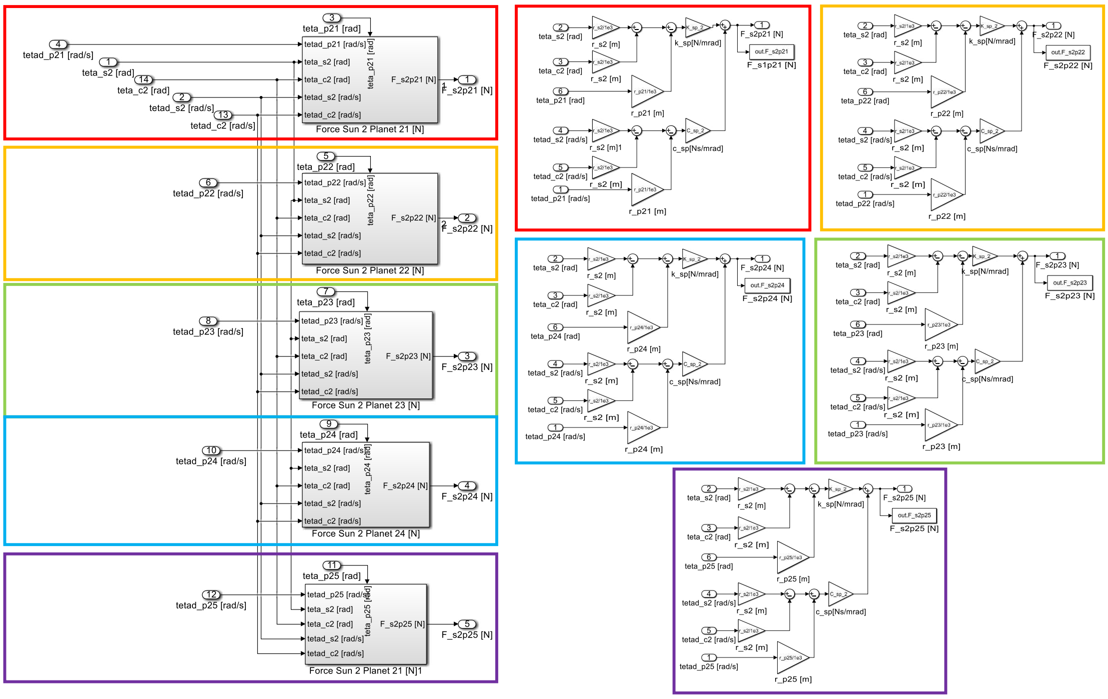

Figure 3.15: Simulink All Force Sun 2 Planet II

The equations which model the gearing forces between the sun and planets are reported to follow by eq. (3.41), for the first stage ($i = 1, ..., N_{pl,1}$), and by (3.42) for the second stage ($i = 1, ..., N_{pl,2}$).

$$\begin{aligned} F_{s1p1,i} &= K_{sp1} \cdot \Delta x_{eq,sp,1i} + c_{sp1} \cdot \Delta \dot{x}_{eq,sp,1i} \\ \Delta x_{eq,sp,1i} &= [(\theta_{s1} - \theta_{c1}) \cdot r_{s1} - \theta_{p1,i} \cdot r_{p1,i}] \\ \Delta \dot{x}_{eq,sp,1i} &= [(\dot{\theta}_{s1} - \dot{\theta}_{c1}) \cdot r_{s1} - \dot{\theta}_{p1,i} \cdot r_{p1,i}] \end{aligned} \tag{3.41}$$

$$\begin{aligned} F_{s2p2,i} &= K_{sp2} \cdot \Delta x_{eq,sp,2i} + c_{sp2} \cdot \Delta \dot{x}_{eq,sp,2i} \\ \Delta x_{eq,sp,2i} &= [(\theta_{s2} - \theta_{c2}) \cdot r_{s2} - \theta_{p2,i} \cdot r_{p2,i}] \\ \Delta \dot{x}_{eq,sp,2i} &= [(\dot{\theta}_{s2} - \dot{\theta}_{c2}) \cdot r_{s2} - \dot{\theta}_{p2,i} \cdot r_{p2,i}] \end{aligned} \tag{3.42}$$

$$F_{p1ir1} = K_{rp1} \cdot [(\theta_{p1i} - \theta_{rj}) \cdot r_{p1i} - \theta_{c1} \cdot r_{r1}] + c_{rp1} \cdot [(\dot{\theta}_{p1i} - \dot{\theta}_{rj}) \cdot r_{p1i} - \dot{\theta}_{c1} \cdot r_{r1}] \tag{3.43}$$

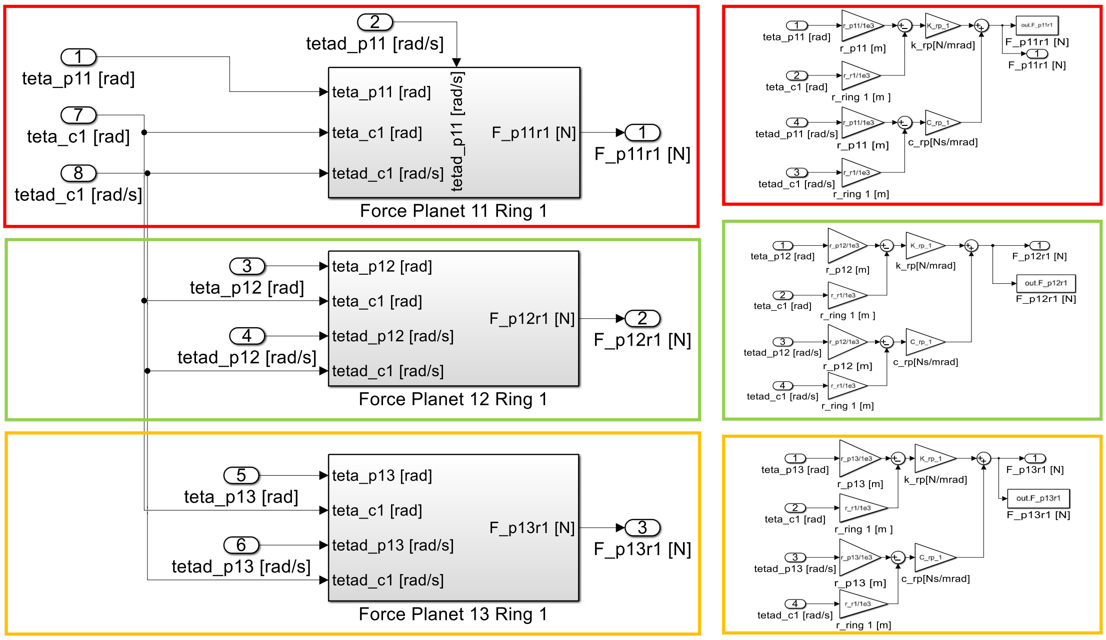

Figure 3.16: Simulink All Force Planet I Ring I

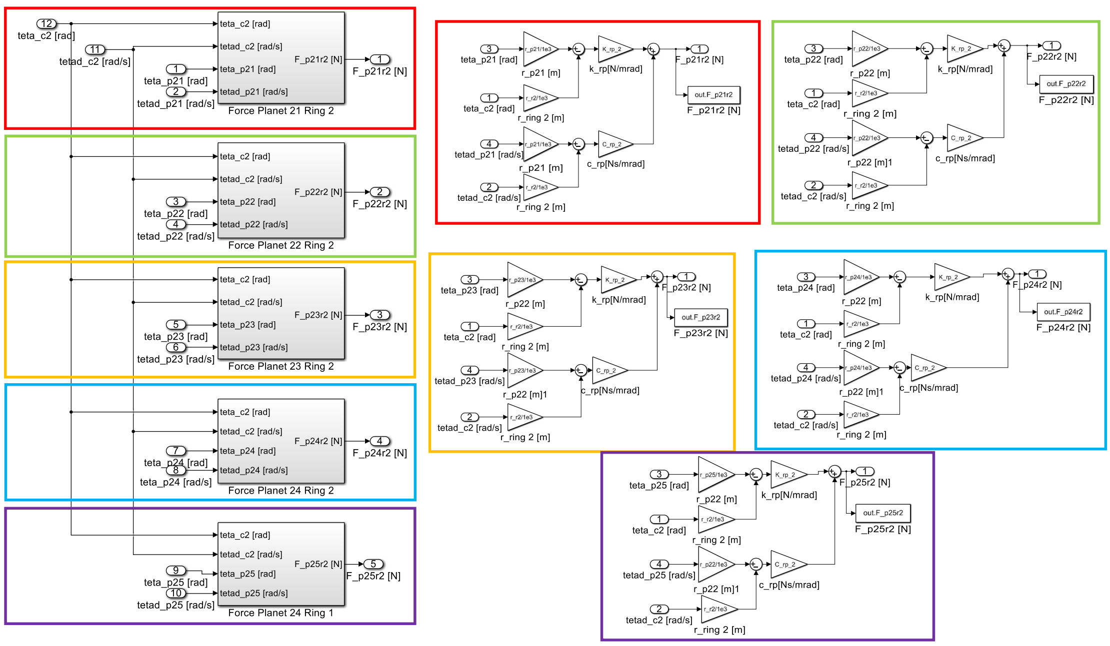

Figure 3.17: Simulink All Force Planet II Ring II

To follow there are the equations which describe the gearing force between the planets and the ring gear, in eq.(3.43) in general form, but recalling that the ring, for both the stages, is fixed so $\theta_{r,i} = 0$ with j = 1,2. In this way, we obtain by eq.(3.44) ($i = 1, ..., N_{pl,1}$), for the first stage Figure 3.16, and by eq. (3.45) ($i = 1, ..., N_{pl,2}$) for the second stage Figure 3.17.

$$
\begin{aligned}
F_{p1i,r1} &= K_{rp1} \cdot \Delta x_{eq,pr,1i} + c_{rp1} \cdot \Delta \dot{x}_{eq,pr,1i} \\
\Delta x_{eq,pr,1i} &= (\theta_{p1i} \cdot r_{p1i} - \theta_{c1} \cdot r_{r1}) \\
\Delta \dot{x}_{eq,pr,1i} &= (\dot{\theta}_{p1i} \cdot r_{p1i} - \dot{\theta}_{c1} \cdot r_{r1})
\end{aligned}
\tag{3.44}
$$

$$
\begin{aligned}
F_{p2ir2} &= K_{rp2} \cdot \Delta x_{eq,pr,2i} + c_{rp2} \cdot \Delta \dot{x}_{eq,pr,2i} \\
\Delta x_{eq,pr,2i} &= (\theta_{p2i} \cdot r_{p2i} - \theta_{c2} \cdot r_{r2}) \\
\Delta \dot{x}_{eq,pr,2i} &= (\dot{\theta}_{p2i} \cdot r_{p2i} - \dot{\theta}_{c2} \cdot r_{r2})
\end{aligned}
\tag{3.45}
$$

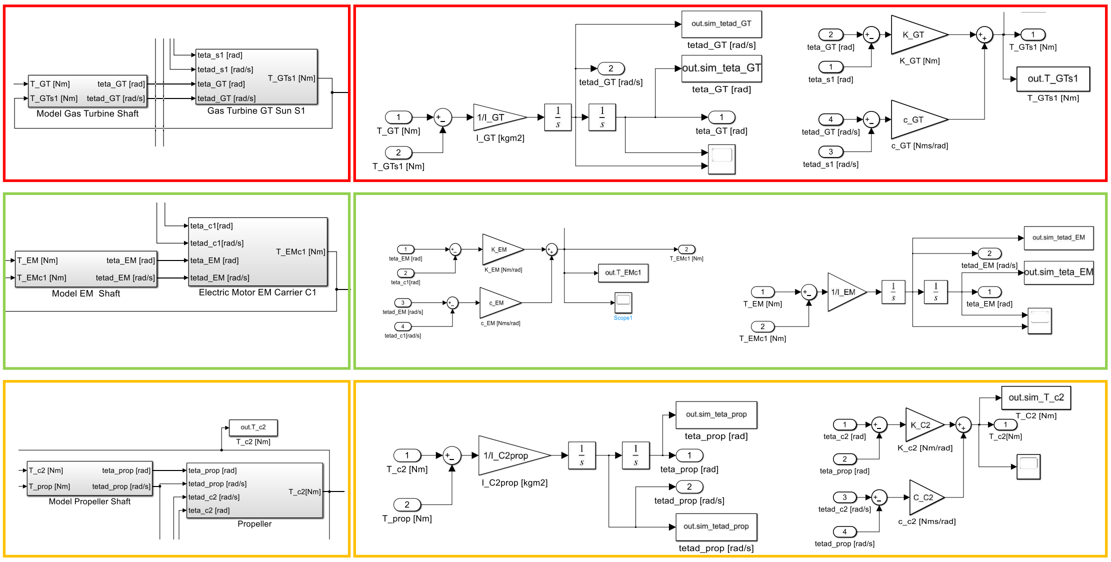

Figure 3.18: Simulink Gas Turbine - Electric Motor and Propeller Models **da qui**

In the end, we analyse the last three green blocks of Figure 3.5, "Model Gas Turbine Shaft" and "Gas Turbine GT Sun S1", eq.(3.46)(3.47), in red square; "Model EM Shaft" and "Electric Motor EM Carrier C1", in eq. (3.48)(3.49), in green square; "Model Propeller Shaft" and "Propeller", in eq.(3.50)(3.51), in orange square in Figure 3.18.

$$
T_{GT} - T_{GTs1} - I_{GT} \cdot \ddot{\theta}_{GT} = 0 \tag{3.46}
$$

$$
T_{GTs1} = K_{GT} \cdot (\theta_{GT} - \theta_{s1}) + c_{GT} \cdot (\dot{\theta}_{GT} - \dot{\theta}_{s1}) \tag{3.47}
$$

$$T_{EM} - T_{EMc1} - I_{EM} \cdot \ddot{\theta}_{EM} = 0 \tag{3.48}$$

$$T_{EMc1} = K_{EM} \cdot (\theta_{EM} - \theta_{c1}) + c_{EM} \cdot (\dot{\theta}_{EM} - \dot{\theta}_{c1}) \tag{3.49}$$

$$T_{C2} - T_{prop} - I_{C2prop} \cdot \ddot{\theta}_{prop} = 0 \tag{3.50}$$

$$T_{c2} = K_{C2} \cdot (\theta_{c2} - \theta_{prop}) + c_{C2} \cdot (\dot{\theta}_{c2} - \dot{\theta}_{prop}) \tag{3.51}$$

3.2.3 Boundary Condition

In this subsection, the boundary conditions of our gearbox will be deepened.

In Figure 2.18 it is easy to understand what is the rotation speed of every single part and, if we were in hybrid cruising conditions, then the solar of the first stage rotates at the speed of the turbine, the carrier of the last stage rotates at the speed of the propeller, and the speed of rotation of the carrier of the first stage, or of the solar of the second stage, is given by the ratio of transmission.

To calculate the rotational speed of each planet is possible to do reference at Figure 3.19.

In Figure 3.19 it is possible to choose three system of reference:

- an integral solar system (red);
- an inertial reference system (black);
- a local referecen system on planet (green);
- three rays in reference to the primitive circumferences of the solar($r_{s,i}$),) the carrier ($r_{c,i}$) and the ring ($r_{r,i}$);
- tangential speed $v_{s,i}$ and $v_{c,i}$ of the points C_1 and O_p (in orange).

It has been hypothesized the wheels roll without sliding on each other and this means that there are two kinematic constrains:

- the points that belong to both wheel O_s and wheel O_p in C_1 have the same speed;
- the speed of the O_p wheel at point C_2 is zero.

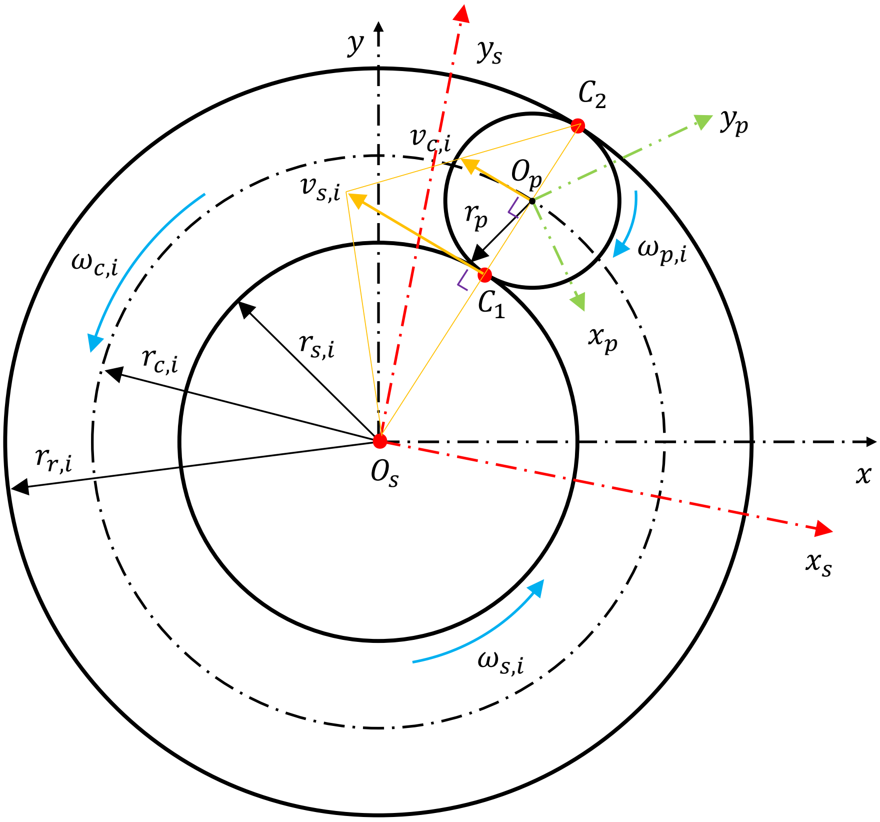

Figure 3.19: Boundary Condition - Planet Rotational Speeds

From all these hypotheses it is possible to write the following equations:

$$\overline{\omega_s} \times \overline{O_s C_1} = \overline{V_{Op}} + \overline{\omega_P} \times \overline{O_p C_1} \tag{3.52}$$

$$\overline{V_{C2}} = \overline{V_{Op}} + \overline{\omega_p} \times \overline{O_p C_2} \tag{3.53}$$

from which:

$$\overline{V_{Op}} = -\overline{\omega_p} \times \overline{O_p C_2} \tag{3.54}$$

is replaced and is obtained

$$\overline{\omega_s} \times \overline{O_s C_1} = 2 \cdot \overline{\omega_p} \times \overline{O_p C_1} \tag{3.55}$$

explaining is obtained

$$\overline{\omega_s} \times \overline{r_s} = 2 \cdot \overline{\omega_p} \times \overline{r_p} \tag{3.56}$$

from which:

$$\omega_{p,i} = \omega_{s,i} \cdot \frac{r_{s,i}}{2r_{p,i}} = \omega_{s,i} \cdot \frac{z_{s,i}}{2z_{p,i}} \tag{3.57}$$

With the same reasoning it is possible to get the speed of the carrier, eq.(3.58) to (3.61) as verification to the transmission ratio eq.(2.64).

$$\overline{v_{c,i}} = \overline{v_{Op}} = \overline{\omega_{c,i}} \times \overline{O_s O_p} = -\overline{\omega_p} \times \overline{C_2 O_p} \tag{3.58}$$

$$v_{c,i} = \omega_s \cdot \frac{r_s}{2} \tag{3.59}$$

$$v_{c,i} = \omega_{c,i} \cdot (r_s + r_p) \tag{3.60}$$

$$\omega_{c,i} = \omega_s \cdot \frac{r_s}{2(r_s + r_p)} \tag{3.61}$$

3.3 Propeller Model

By reference in Figure 3.5, in light blue, it is possible to see:

- the propeller's block reported in Figure 3.20;
- the pitch controller model reported in section 3.4 Figure 3.23;
- the atmosphere model reported in section 3.5 Figure 3.25.

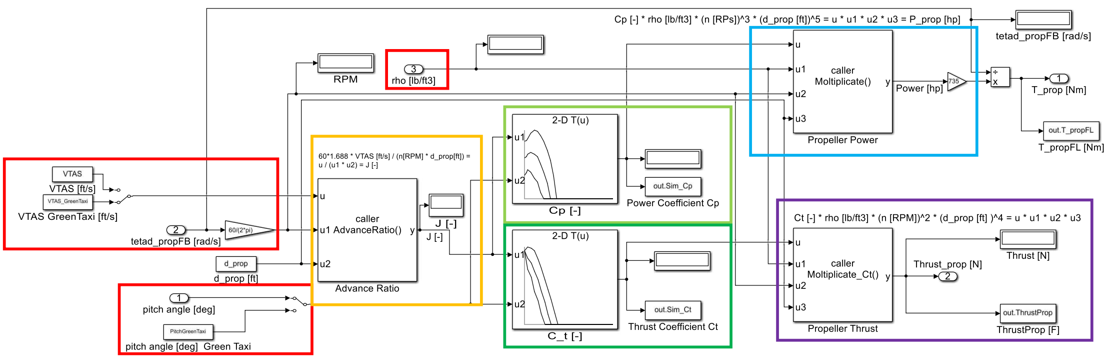

Figure 3.20: Simulink Propeller Model

The blocks in Figure 3.20 represents:
the red blocks are the input's parameters:

- the True Air Speed Vehicle in $[ft/s]$ (VTAS), the real airspeed which collision itself with the aircraft;
- the $\dot{\theta}_{FB}$ in $[rad/s]$ the feedback signal by "Model Propeller Shaft" in Figure 3.18;
- the pitch angle in $[deg]$ represents of how much is showered the propeller of the aircraft;
- the propeller's diameter in $[ft]$

The orange block represents the function which calculates the advance ratio $J[-]$ reported in eq.(3.62).

$$J = 60 \cdot 1.688 \cdot \frac{VTAS}{n \cdot d} \tag{3.62}$$

Through the Advance Ratio $J[-]$, eq.(3.62), is possible to calculate the power coefficient $C_P[-]$ and the thrust coefficient $C_T[-]$ by Simulink's element called 2-D Lookup Table of reported in light and dark green blocks in Figure 3.20. In these blocks there are implemented the eq.(3.64)(3.63) to calculate these factors, Fgiure 3.21 3.22.

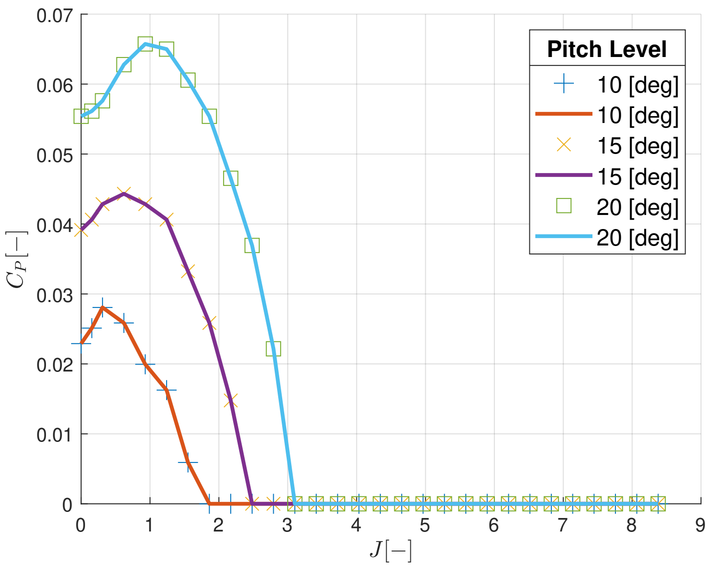

Figure 3.21: Simulink Power Coefficient C_P

$$C_P = \frac{1.188 \cdot 10^8 \cdot P_{prop}}{\rho \cdot \omega^3_{prop,FB} \cdot d^5_{prop}} \tag{3.63}$$

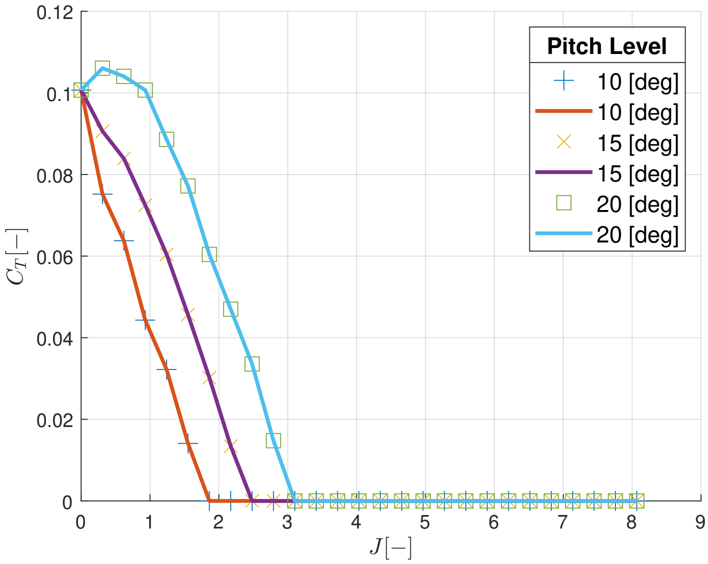

Figure 3.22: Simulink Thrust Coefficient C_T

In which:

- P_{prop} is the propeller's power in $[hp]$;
- ρ air density dependent on the quote of flight in the considered phase of the mission $[lb/ft^3]$;
- $\omega_{prop,FB}$ is the propeller's speed in feedback in $[cycle/s]$;
- d_{prop} propeller's diameter in $[ft]$.

$$C_T = \frac{3600 \cdot Th}{\rho \cdot \omega_{prop}^2 \cdot d_{prop}^4} \tag{3.64}$$

In which:

- T_h is the propeller's thrust in $[N]$;
- ρ, $\omega_{prop,FB}$ and d_{prop} are the density of the air, propeller's speed in feedback and propeller's diameter.

The light blue and violet blocks represent the function by which the fluid-dynamic power of the propeller, eq.(3.65), so the torque if we divided it with the rotational speed, and the fluid-dynamic thrust of the propeller, eq.(3.66), are calculated.

$$P = C_P \cdot \rho \cdot \omega^3_{prop,FB} \cdot d^5_{prop} \tag{3.65}$$

$$T_h = C_T \cdot \rho \cdot \omega^2_{prop,FB} \cdot d^4_{prop} \tag{3.66}$$

3.4 Pitch Controller Model

In the end, it is modelled the pitch controller, namely the model part which define how much the propeller of the aircraft is out of gear (Figure 3.23).

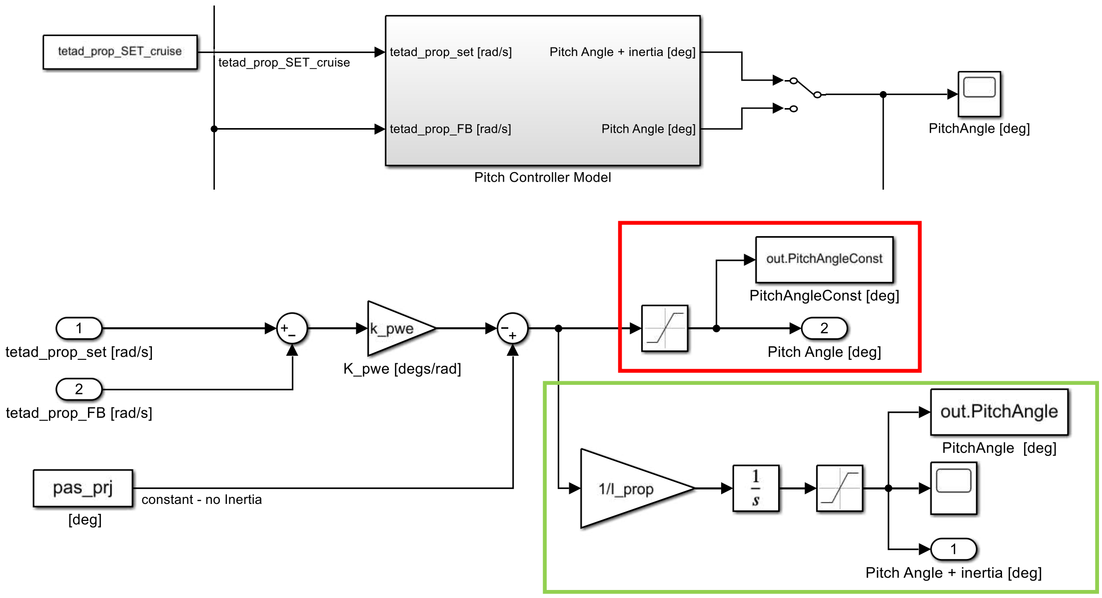

Figure 3.23: Simulink Pitch Controller Model

This mode takes input an angular velocity error ($e = \omega_{SET} - \omega_{FB}$) and by this calculates a pitch angle.

The speed error is multiplied by a gain ($K_{p,we} = 20\frac{deg}{rad/s}$) and then subtracts the design pitch value ($pass_{prj}$). Then, if you consider the inertia of the propeller or not, you can have a "PitchAngleConst" (red square) or "PitchAngle" (green square). Both have saturations as the inclination of the helix is between $10deg$ and $20deg$.

The ω_{SET} input depends on the phase of the mission and it is fixed and imposed from outside, while the ω_{FB} is taken by the model (Figure 3.5)

3.5 Atmosphere Model

At the end it is introduced the model of the atmosphere (Figure 3.24 - [37]), that is how the temperature and the density changes in function of the flight altitude in the relative phase of the mission (Figure 3.25).

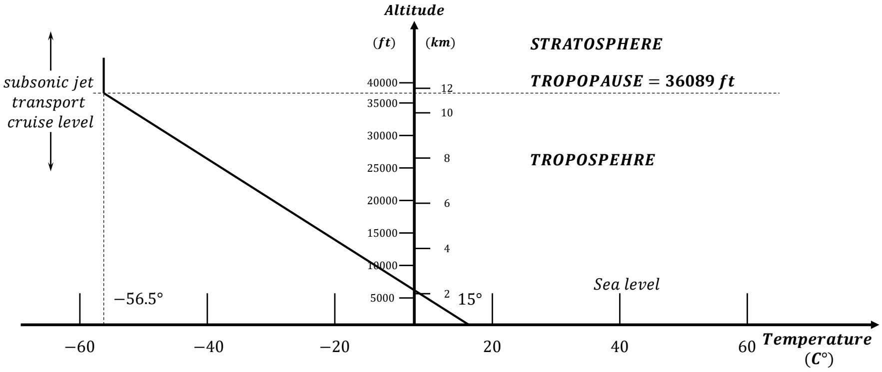

Figure 3.24: Atmosphere Model [37]

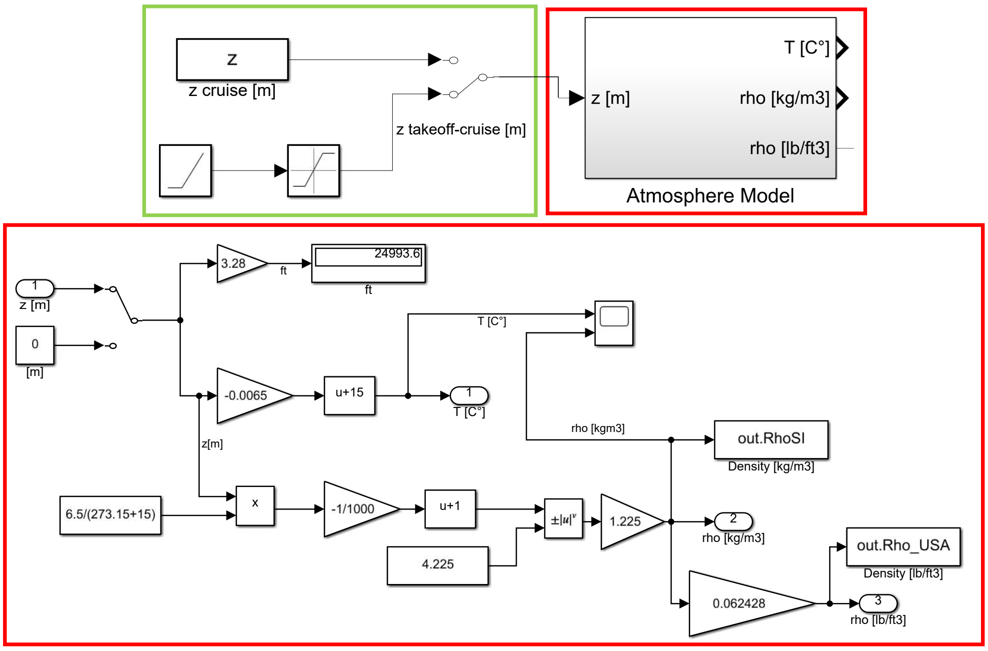

Figure 3.25: Simulink Atmosphere Model

In Figure 3.25 is possible to see different blocks:

- the green block represent the input variables (cruise and takeoff) in which the cruise phase is a array with the fixed reference quota, while the take-off phase is a vector with dependency line from zero to the reference altitude ($25000 ft$ or $7620 m$);
- the red block represents the model of the atmosphere with the output temperature and dentity in the international (SI) and American (USA) system.

Chapter 4

Results

The objective of this chapter is to present the results obtained from the dynamic analysis of the two-stage reduction planetary hybrid In-Line transmission (Figure 3.5).

As mentioned above, the meshing between the gears is similar to a damper spring system.

At first, the results will be presented in the various phases of flight (cruise and take-off) assuming that the stiffness is constant for the duration of the simulation in the Stationary Behavior in Section 4.1 ($K = f(m_i, z_i, \varepsilon_i)$), while in the section Non stationary Behavior 4.2 the frequency of meshing shall be taken into account, that is to say, that the stiffness is variable as a function of time [$K = f\,(m_i, z_i, \varepsilon_i, \omega_{s,i}(t))$].

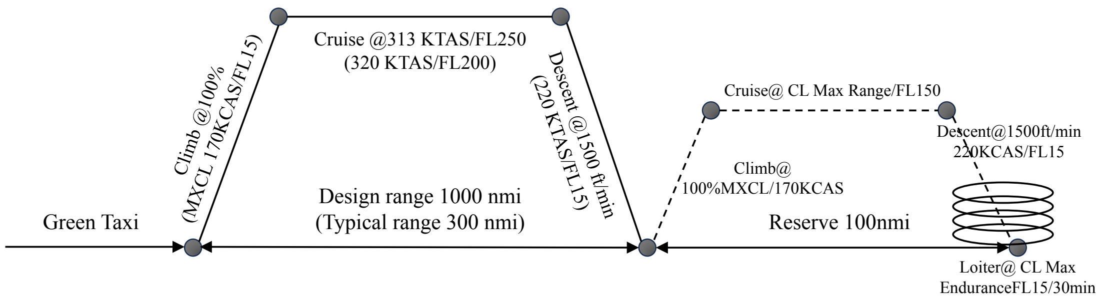

Figure 4.1: Reference Mission Profile

All this will be done on the generic mission profile in Figure 4.1, in particular in the Climb and Cruise phase both in hybrid propulsion mode.

In the Figure 4.1 it is possible to see:

- the calibrated airspeed (170KCAS) and the quote of reference (FL15) in the climb phase;

- the True Airspeed (313 KTAS) and the quote of reference (FL250) in the cruise phase;
- the speed of descent (1500 ft/min) to the reference altitude (FL15) in the descent phase.

4.1 Stationary Behavior

The results obtained in the cruise and take-off phases will be shown below using a constant gear-up stiffness.

The results will show and comment on the evolution of torques, forces and pitch angles in the relevant phase of the flight mission.

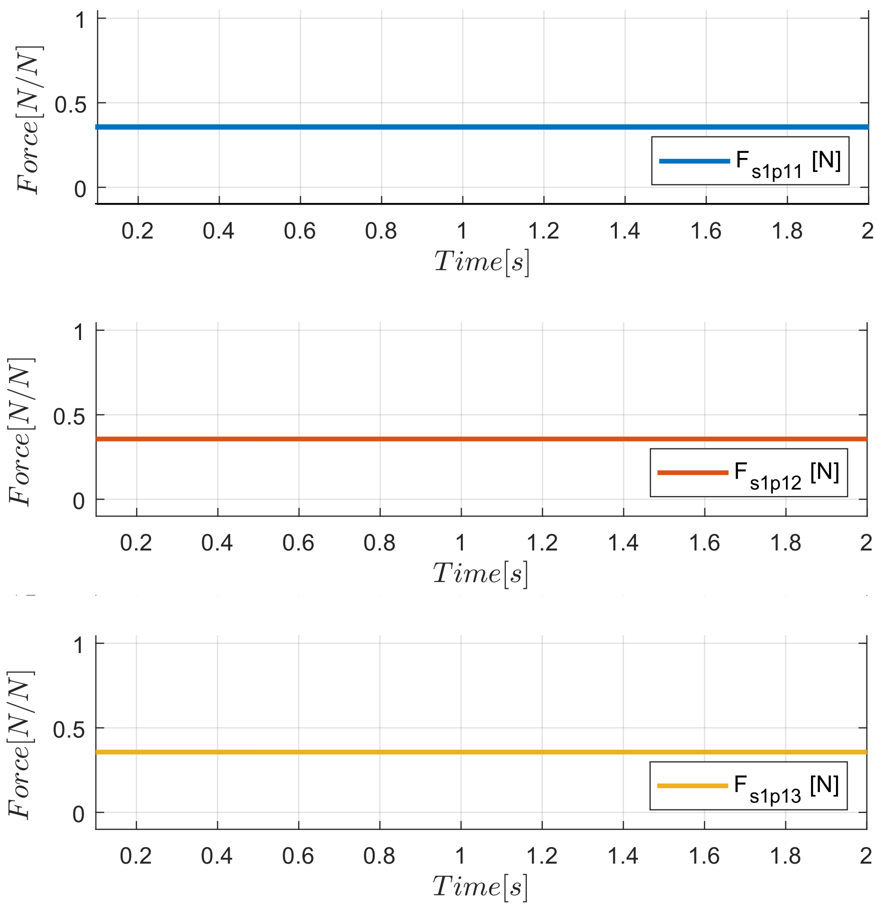

Figure 4.2: All Forces Sun-Planet Meshing - Stage One - Constant Stiffness - Cruise Phase

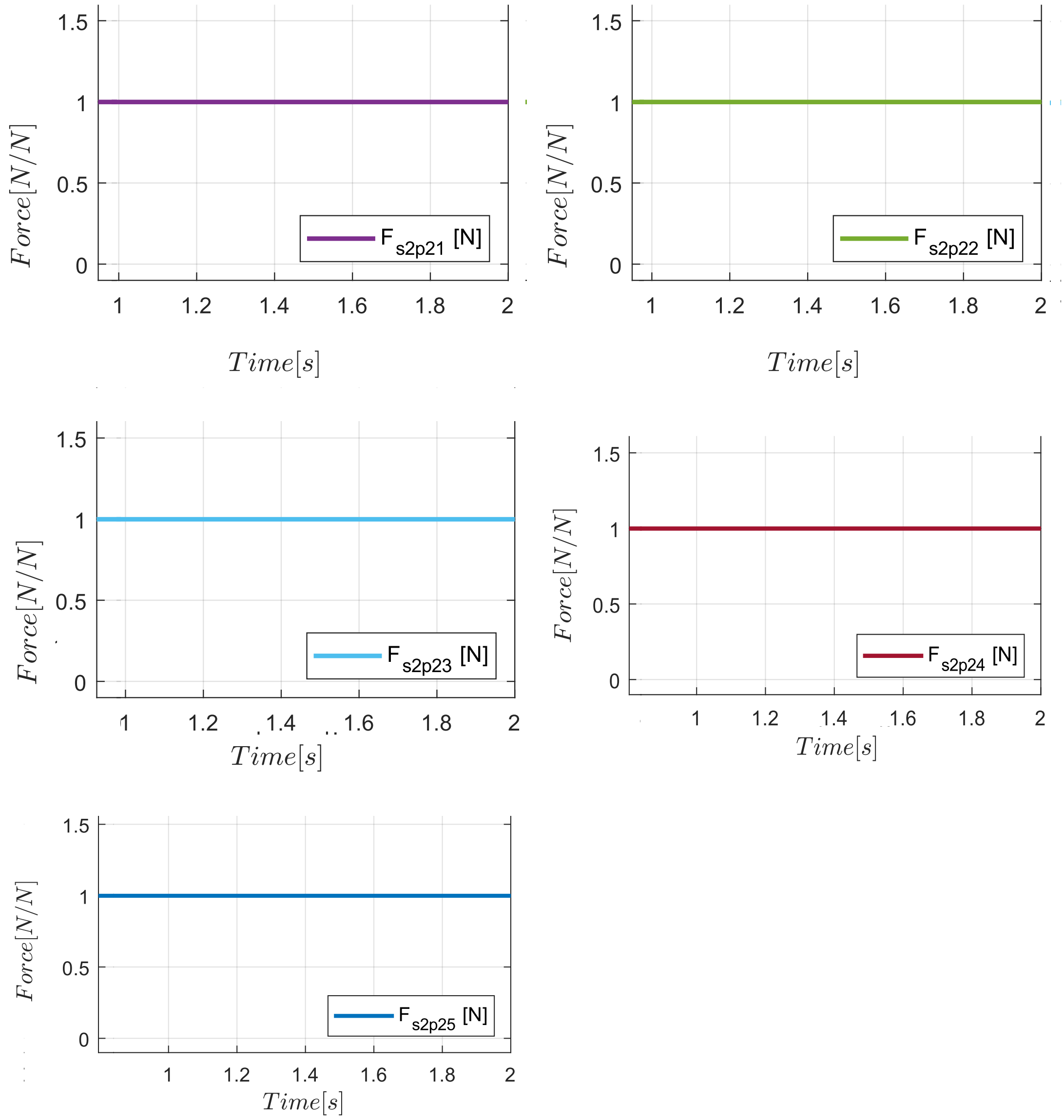

Figure 4.3: All Forces Sun-Planet Meshing - Stage Two - Constant Stiffness - Cruise Phase

In Figure 4.2 and 4.3 it is possible to see all meshing forces between solar and planetary of the first ($F_{s1,p1,i}$), Figure 4.2 , and second stage, Figure **??** ,($F_{s2p2,j}$).
The forces have been dimensioned and it is possible to see that from the passage between the first and the second stage there is a multiplication of about 2.5 times.
All forces are constant during the cruise phase and they don't introduce delays of phase between they. In addition, there are no oscillations of any kind as the stiffness of the mesh is constant.

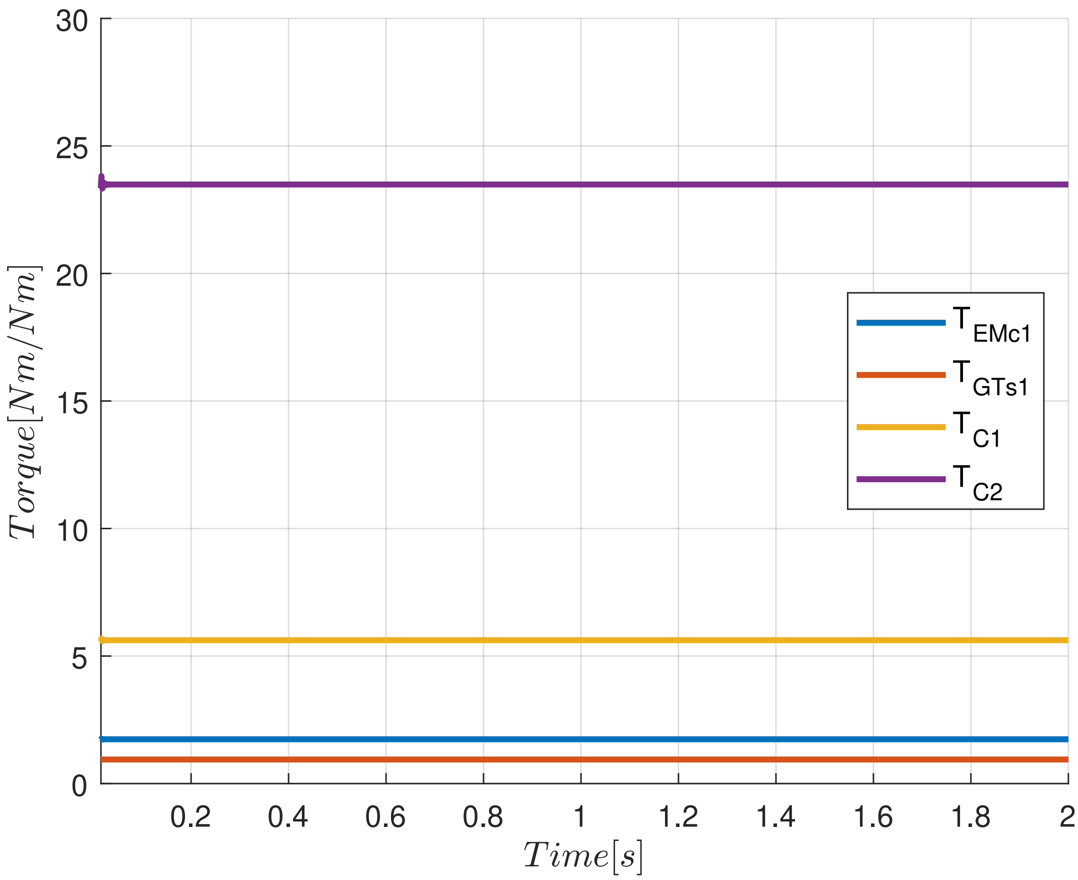

Figure 4.4: Torques - Constant Stiffness - Cruise Phase

In Figure 4.4 it is possible to see:

- all torques are consistent with how they should be for the cruise phase, that is constant throughout the duration of the phase;
- the torque of the EM (T_{EMc1}) is about double that of the GT (T_{GTs1});
- the torque at the exit of the carrier 1 (T_{C1}), then at the input of the solar second stage, is about 6 times that of the turbine (T_{GTs1}) and about 3 times that of the electric motor (T_{EMc1});
- the output torque (T_{C2}) is greater than 20 times the input for the turbine;
- all torques show no fluctuation in their values.

In the end, there it is reported the comparison between the output torque of the gearbox and the fluid dynamic torque of the propeller.

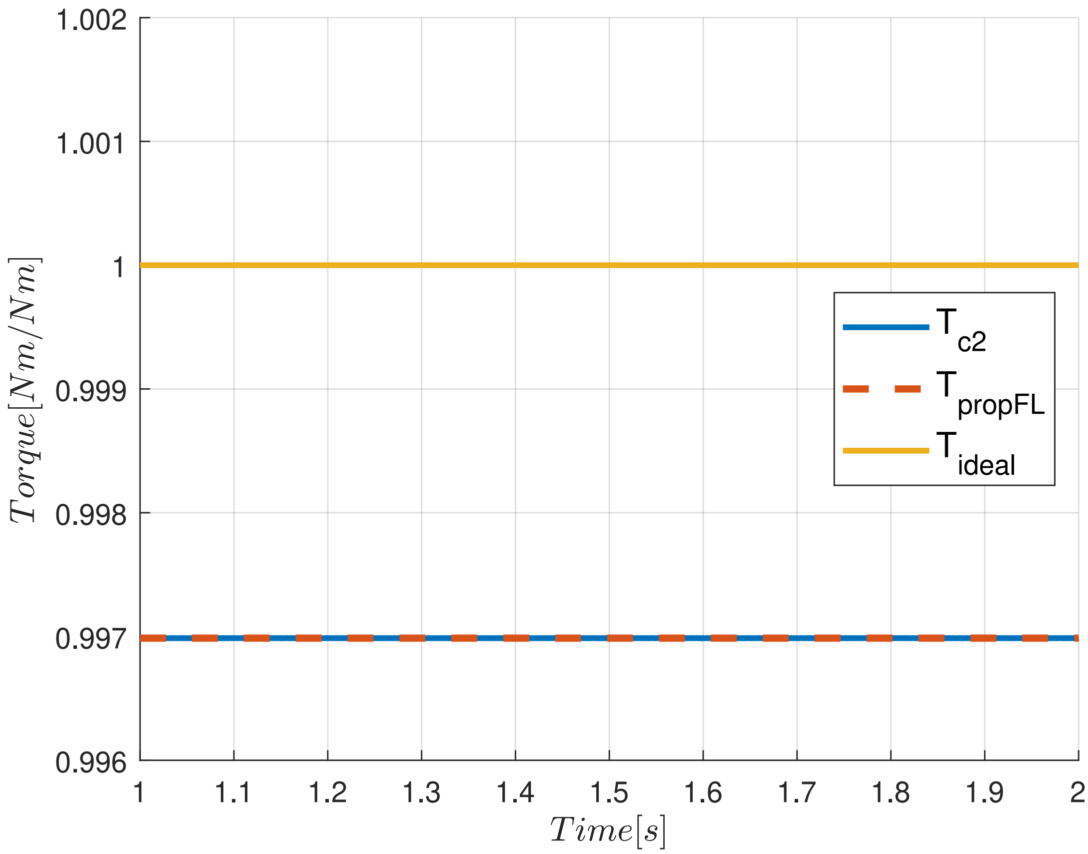

Figure 4.5: Comparison between Torque Output from the GB and Dynamic Fluid Torque of the Propeller - Constant Stiffness - Cruise Phase

In Figure 4.5 it is reported the summary of output torque the GB and it shows:

- T_{c2} the torque given output by the gearbox (light blu) by the model in Figure 3.5;
- T_{propFL} in red how the torque output of the Propeller Model in reference to Figure 3.20;
- T_{ideal} it is a ideal, constant and numerically exact torque given by the global transmission ratio of the GB reported in eq. (2.65).

In addition to this, the fluid dynamic torque of the propeller (T_{propFL}) is co-linear with the output torque of GB (T_{c2}). Moreover the difference between the numerically correct value, T_{ideal}, and the output value of the model, T_{c2}, is less of 0.3 per cent.

As for all the other figures of this section, the pairs do not have any type of fluctuation of their mean value.

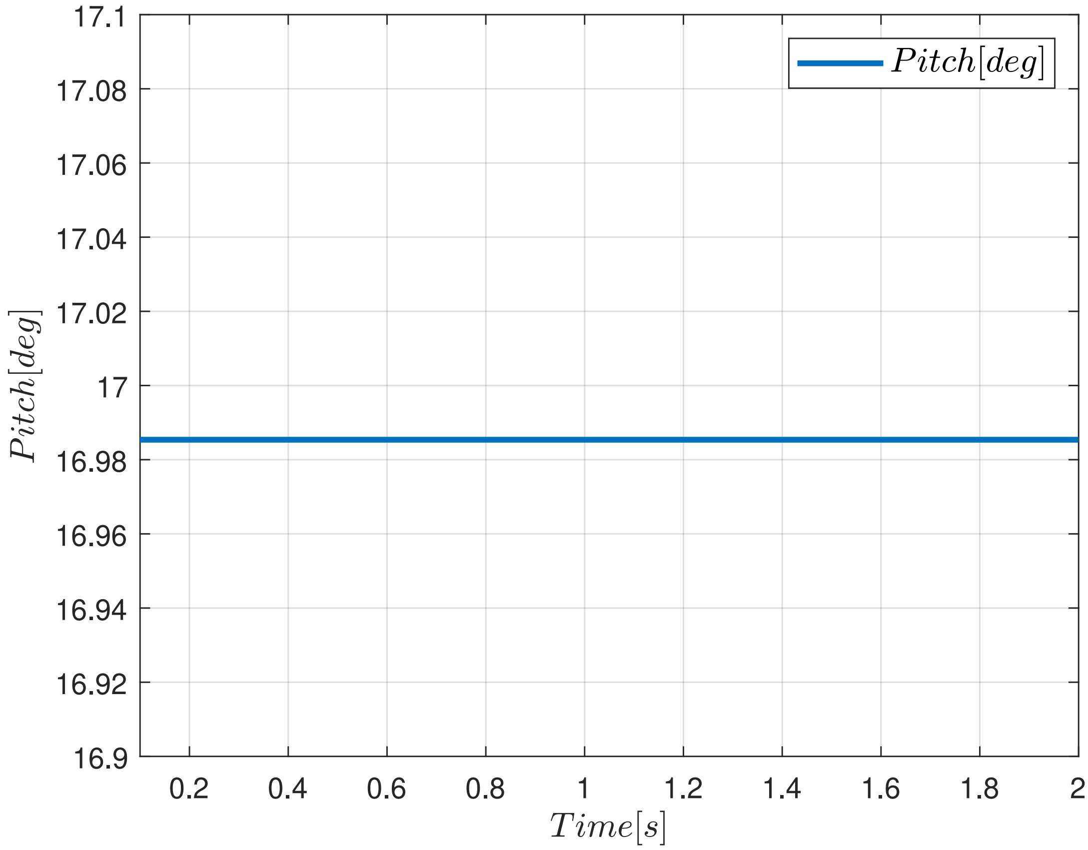

Figure 4.6: Pitch - First Order Modeling - Constant Stiffness - Cruise Phase

Figure 4.6 shows the course of the step and it is a constant value for all the duration of the phase of the mission.

Moreover, all these analyses were carried out with the hypothesis that the propeller has been modeling whit first order, that is according to the red box shown in the Figure 3.23.

Below are the results of the quantities that are changing when considering a second order for the pitch, in reference to the green box in Figure 3.23.

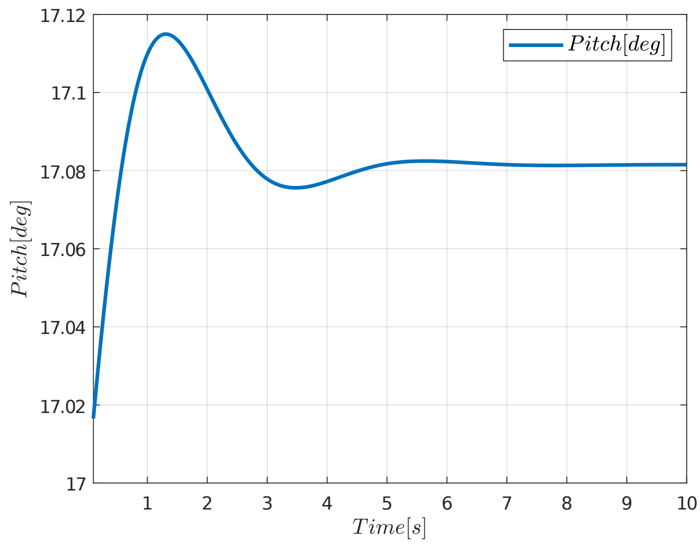

Figure 4.7: Pitch - Second Order Modeling - Constant Stiffness - Cruise Phase

In Figure 4.7 it is possible to see when the pitch controller dynamics are considered. It is simulated with a second order system and it reported the presence of overshoot up to a value of regime higher than Figure 4.6.

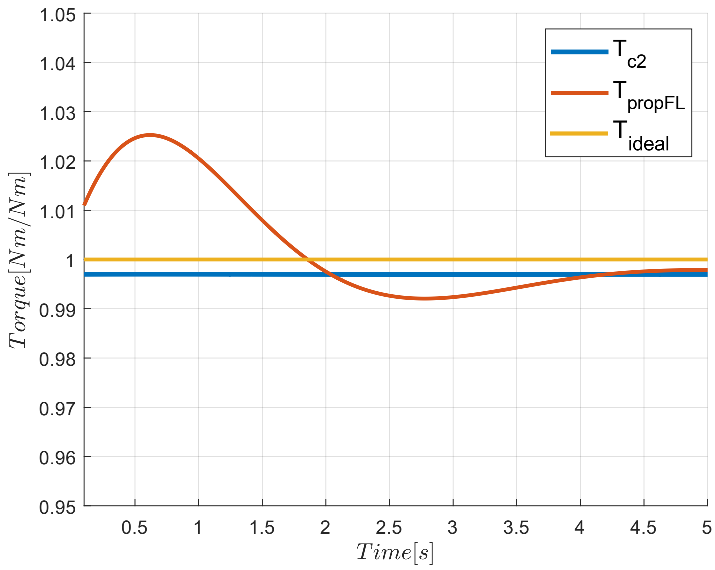

Figure 4.8: Fluid Dynamic Torques - Output GB Torque and Constant Torque with Second Order Modelling of the Pitch - Constant Stiffness - Cruise Phase

The direct consequence of this is reported in Figure 4.8 where it is possible to see how the propeller dynamic fluid torque (T_{propFL}) changes between about 1 and 3 per cent in the first 3 seconds and then stabilizes at the speed value with an error of less than 0.3 per cent as shown in Figure 4.5.

The cruise phase is over. The results are related to the analysis of take-off or climb phase, with reference to Figure 4.1, always with constant gear-up stiffness.

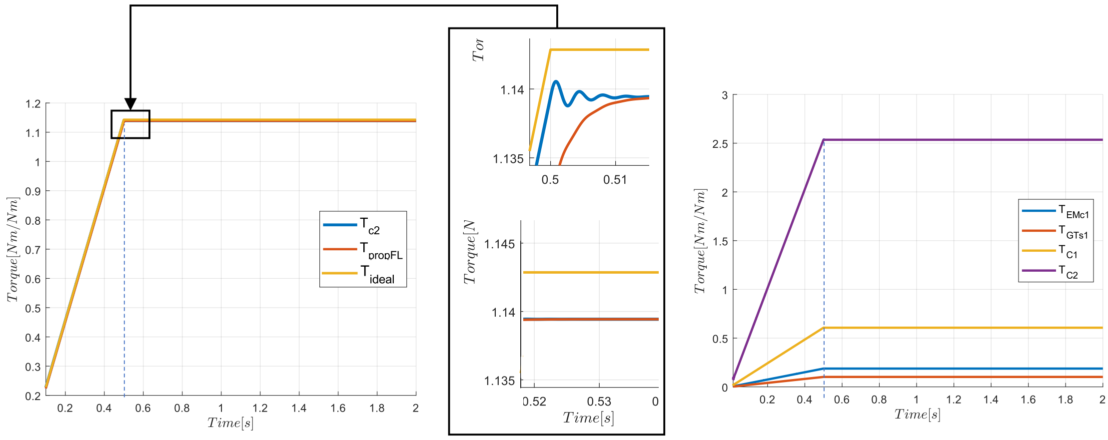

Figure 4.9: Torque - Constant Stiffness - Take-off Phase

In Figure 4.9 it is possible to see:

- the output torque from the GB (T_{c2}) has small oscillations in the transition between the Climb and Cruise phases and it consider all dynamic effects by all torques within the gearbox;
- dynamic fluid torque (T_{propFL}) no oscillation;
- the difference between the dynamic fluid torque (T_{propFL}) and the ideal torque (T_{ideal}) is given by the transmission ratio is about 0.61 percent;
- the trend of the torques of the EM, GT, $C1$ and $C2$ have a linear course in the phase of take-off and reflect the behaviour in the phase of Cruise brought back in Figure 4.4

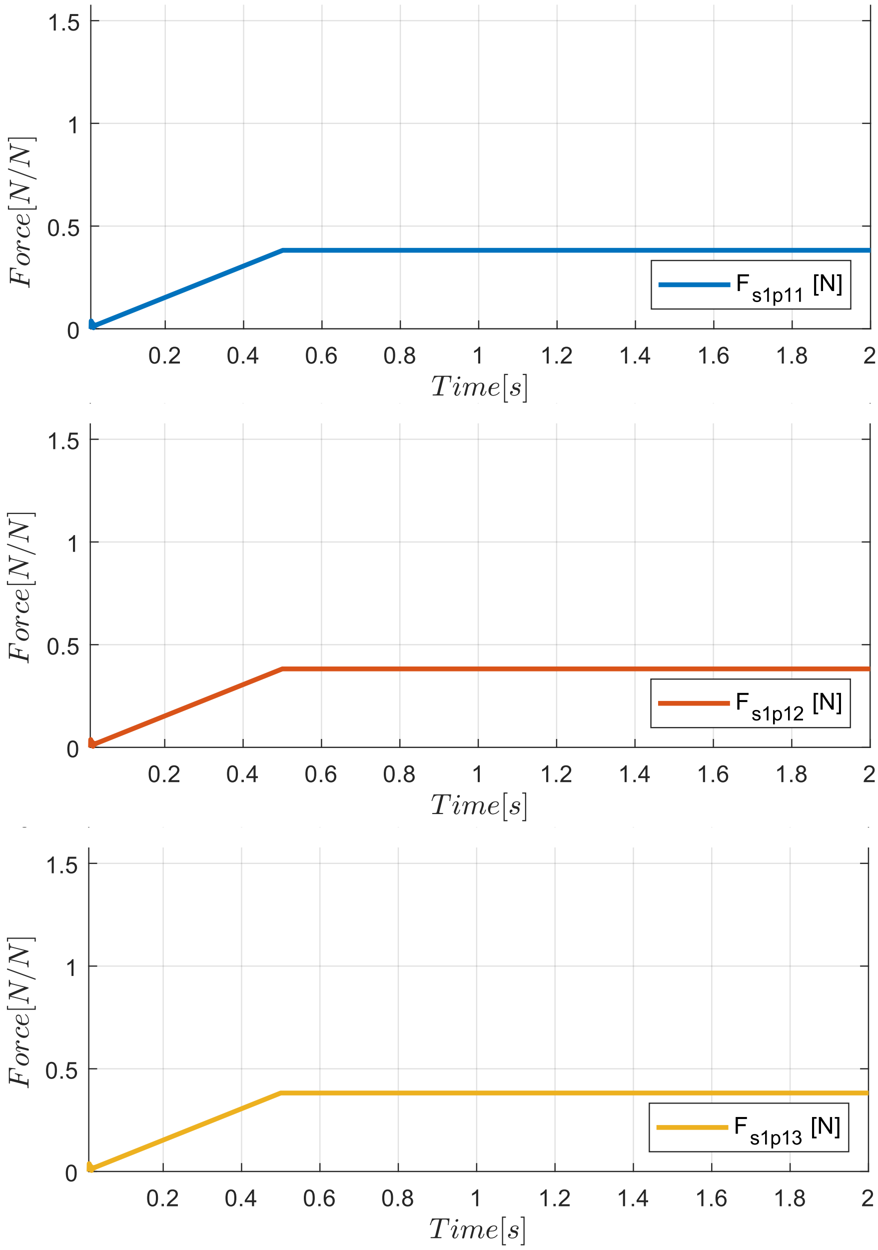

Figure 4.10: Forces - Stage One - Constant Stiffness - Take-off Phase

The trend of the forces of the first stage reduction is reported in Figure 4.10 and it reflects that of the torques. There is a linear trend in the takeoff phase until a constant trend in the regime phase and there are not oscillation.

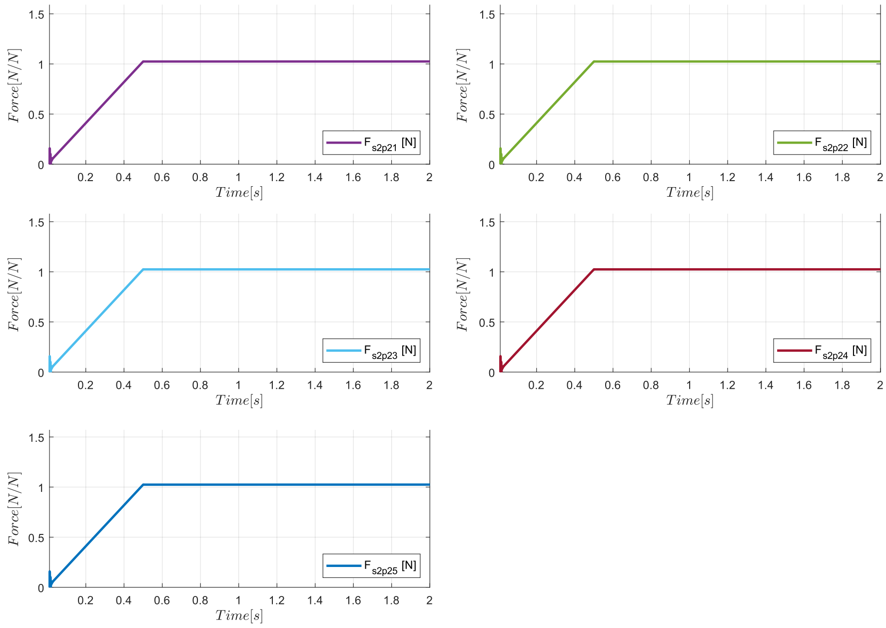

Figure 4.11: Forces - Stage Two - Constant Stiffness - Take-off Phase

Figure 4.11 shows the trend of the forces of the second stage of reduction of the take-off phase. The considerations are similar to those above for Figure 4.10. In addition, it is possible to see that between the first and the second stage there is an increase of about 2.5 times.

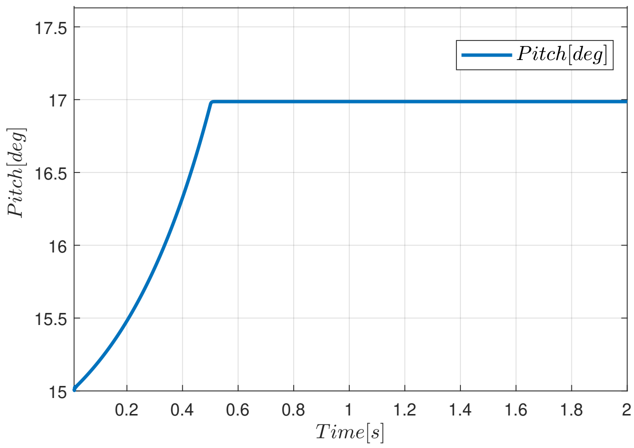

Figure 4.12: Pitch - First Order Modeling - Constant Stiffness - Take-off Phase

The Pitch has a quadratic course in the initial stretch of take-off until to arrive to a constant value and equal to that of the phase of cruise brought back in Figure 4.6.

4.2 Non Stationary Behavior

The same type of analysis will be reported below considering a variable stiffness, namely with a meshing frequency.

It will be showed firstly the results on the cruise phase and after then on take-off phase.

Finally, the results obtained with variable and constant meshing stiffness will be compared.

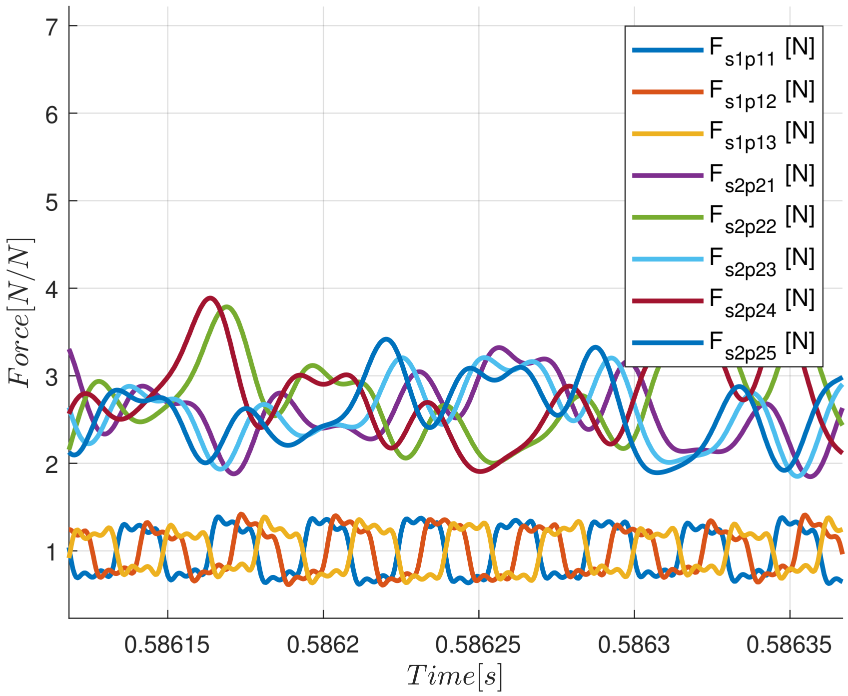

Figure 4.13: Forces - Variable Stiffness - Cruise Phase

From the comparison between Figures 4.13 and Figure 4.2 and 4.3 it is noted as:

- the average value of the forces of the first stage and the average value of the forces of the second stage reflect the trend in Figure 4.2 and 4.3;
- a large magnification must be made to visualize the phenomenon, since the speed of rotation and therefore the frequencies are high;
- all forces show a variable pattern over time of the module due to the dependence on the frequency with which they come into contact.

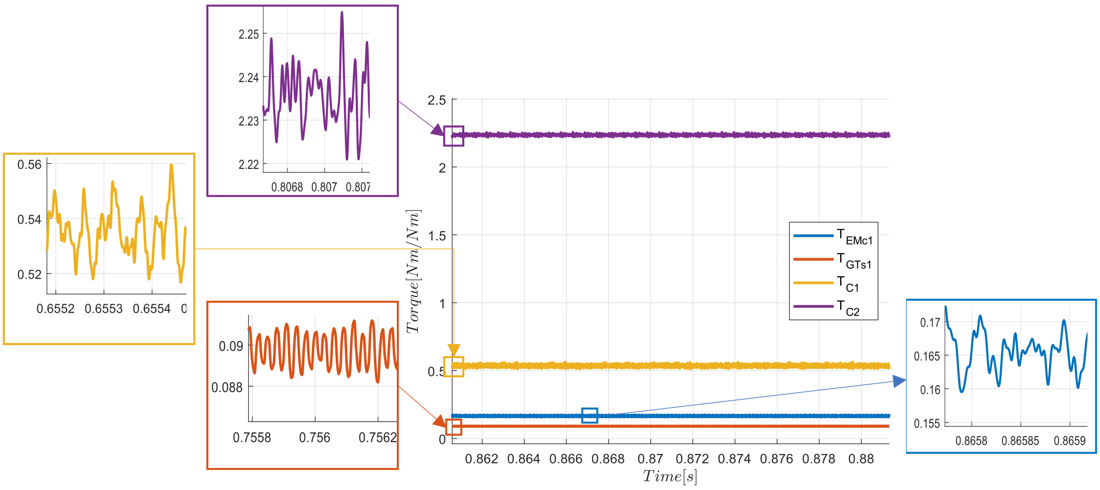

Figure 4.14: Torques - Variable Stiffness - Cruise Phase

The comparison between Figure 4.14 and Figure 4.4 shows: all four torques have more or less obvious fluctuations; the T_{GTs1} torque is the one that has fluctuations less similar to the trend of the gear stiffness; the torques leaving the carrier $C1$ and the carrier $C2$ are those which are most affected by the effect of variable stiffness; and the trend of the T_{c2} torque is given by the overlap of all other correct gear ratios.

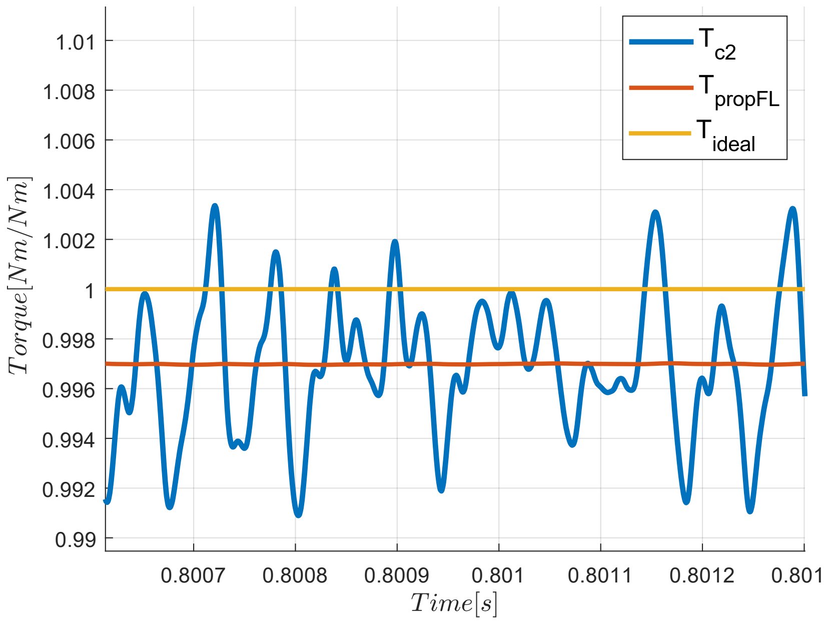

Figure 4.15: Torques Output of GB - Variable Stiffness - Cruise Phase

The Figure 4.15 shows: the difference between the dynamic fluid torque (T_{propFL}) and the ideally correct torque (T_{ideal}), given by the gear ratios, is 0.3 per cent as shown in Figure 4.5; the average value of (T_{c2}) matches the trend of (T_{propFL}); the T_{c2} trend is given by the overlap of the other corrected pairs of the transmission ratio according to the eq.(2.65); the maximum difference between T_{c2} and T_{ideal} is -0.8 per cent and a MAPE is 0.6 per cent.

The trend of the Pitch with a second or first order modeling is identical to the case where the stiffness remains constant.

If Pitch is modeled with a second order then the trend is similar to that reported in Figure 4.8 with the difference that the torques will introduce of the oscillations similar to those brought back in Figure 4.14.

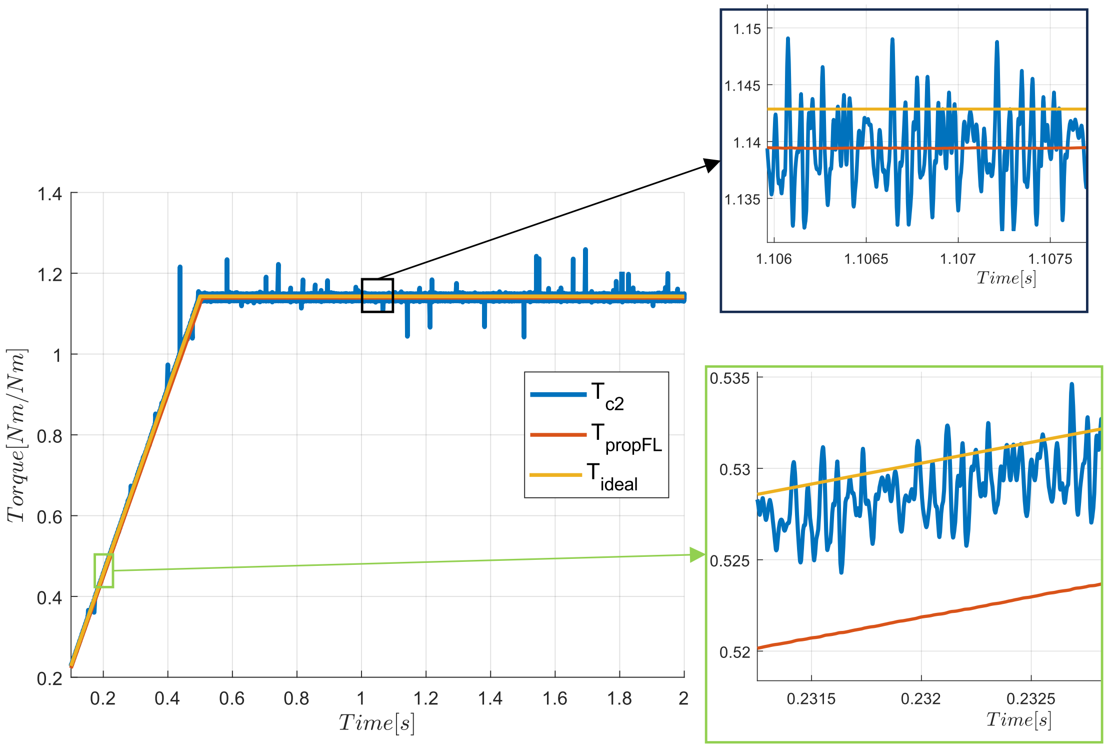

Figure 4.16: Torques Output of GB - Variable Stiffness - Take-Off Phase

The trend of the torques is similar to that reported in Figure 4.9, but with small differences in this case, in Figure 4.16:

- there are oscillation of the torques in both phases, climb and cruise, given by gear-meshing variable stiffness;
- the value of T_{c2} is affected by oscillation given due to the overlap of the torques inside the GB;

- the fluid dynamics torque (T_{propFL}) is not affected by variable stiffness;
- the difference between the fluid dynamics torque (T_{propFL}) and the ideal torque (T_{ideal}) is around 1.88 per cent in take-off phase and 0.43 per cent in cruise phase;
- the maximum amplitude of the output torque from the GB (T_{c2}) is about 1.13 percent of its mean value.

4.2.1 Green Taxi Simulation

The taxi phase is the part of the mission that takes place before the take-off or post-landing phase of an aircraft. This is the time spent after landing until the aircraft is parked and the engines are turned off (taxi/idle in), but also the period between engine start and take-off (taxi/idle out). The case dealt with in the Figure 4.1 refers to the pre-take-off phase. In addition, the term "green" indicates that the energy for propulsion is given entirely by the EM and therefore without the thermal part of GT. This results in fuel savings of between 10 per cent and 30 per cent in operation in the pre-take-off phase or after landing [38]-[39].

Inputs at this stage are always in terms of torques that the gearbox must transmit to the propeller to obtain that push date so that the aircraft can move on departure or off the runway for take-off or parking.

Considering an MN of 0.03 it is possible to obtain the necessary dynamic fluid thrust that must be applied to the aircraft during the taxi phase.

The conditions under which the aircraft is in that phase are:

- air temperature and density at Sea Level;
- MN of the Sea Level, namely $MN = 0.03$;
- propeller rotation speed of 30 per cent compared to cruise ($\omega_{prop,taxi} = 0.3 \cdot \omega_{prop,cruise}$);
- a minimum pitch angle of 10 deg;
- VTAS accordin to eq.(4.1)(4.2)

$$VTAS = \sqrt{\left(\frac{2(P_0 - P)}{\rho}\right)} \tag{4.1}$$

$$P_0 - P = \left[\left(1 + \frac{\gamma - 1}{2} \cdot \frac{v^2}{v_{sound}^2}\right)^{\frac{\gamma}{\gamma-1}} - 1\right] \cdot P \tag{4.2}$$

In which:

- VTAS is the real speed with which an atmospheric air instead of an aircraft;
- γ is the ratio of the specific heat coefficient at constant pressure (c_p) divided by the specific heat coefficient at constant volume (c_v);
- P_0 is the total pressure written in compressible speed according to eq.(4.2) given by the sum of dynamic pressure and static pressure;
- ρ is the air density at Sea Level;
- v and v_{sound} are the displacement speeds of the aircraft and the speed of sound calculated at Sea Level.

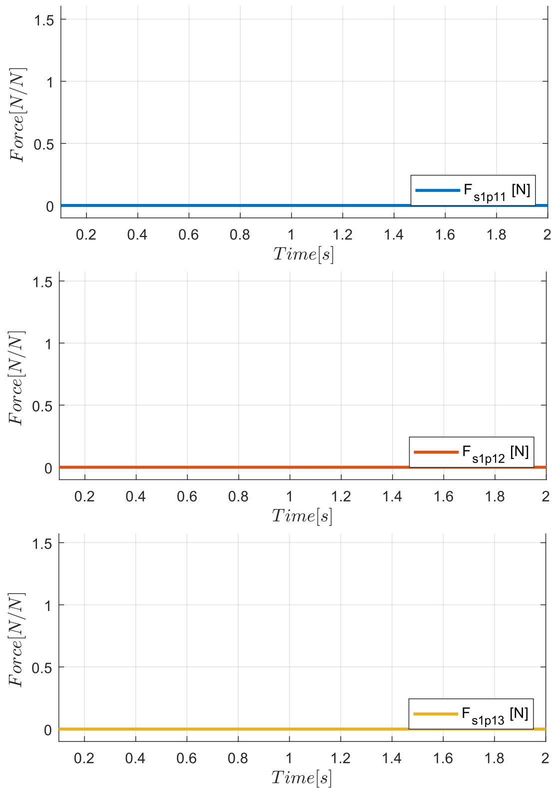

Figure 4.17: Forces Stage One - Constant Stiffness - Taxi Phase

In Figure 4.17 it is possible to see how the forces on the first stage planetary are all zero ($F_{s1p1,i} = 0$) for all mission phase and there are not oscillation.

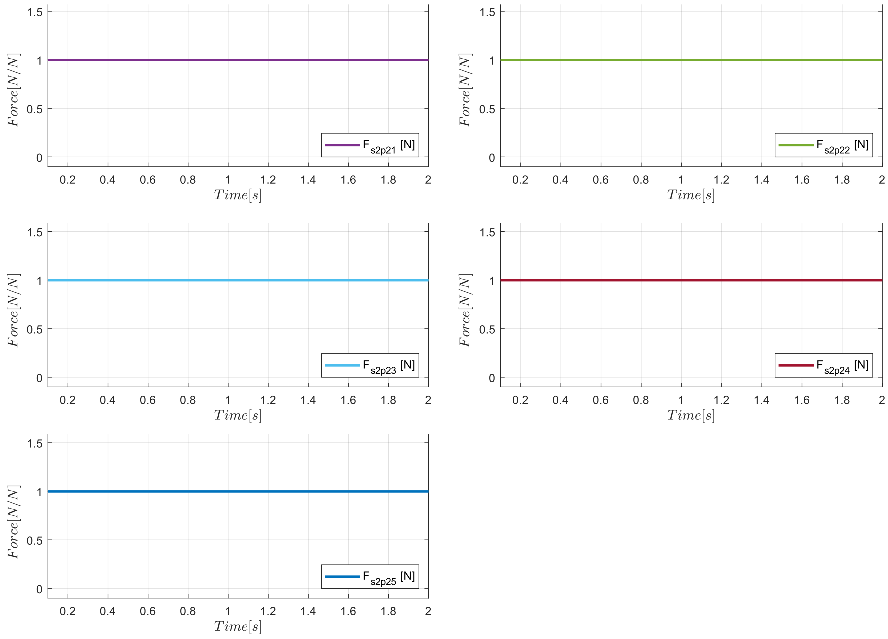

Figure 4.18: Forces Stage Two - Constant Stiffness - Taxi Phase

While in Figure 4.18 the forces of second planetary stage are not zero ($F_{s2p2,i} = 1$). This succeed because the total EM torque is discharged in the second stage and the GT contribution is null. Also here there are not oscillation. The angle of the propeller is similar to that shown in Figure 4.6 only with a 10 deg wintering.

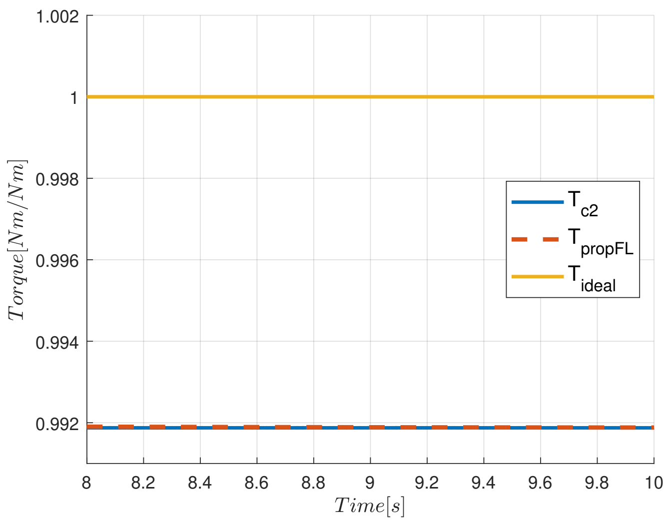

Figure 4.19: Output Torques Gearbox - Constant Stiffness - Taxi Phase

In the end, Figure 4.19 shows the output torque's trend of the Gearbox. The torques are consistent with the phase of the mission, in fact they are all constant as in the cruise phase.

The difference between the ideal and the real behavior, namely the difference between ideal torque (T_{ideal}), fluid dynamic torque (T_{propfl}) and output gearbox torque (T_{c2}) is around the 0.8 per cent, a negligible difference.

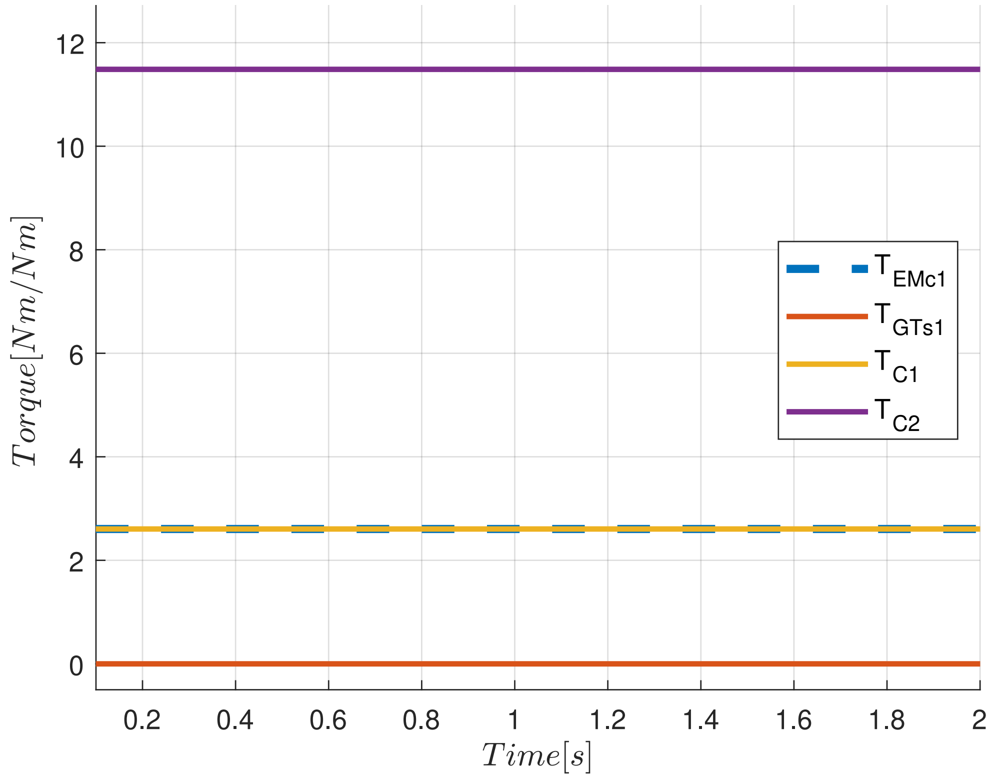

Figure 4.20: Torques GB - Constant Stiffness - Taxi Phase

In Figure 4.20 it is possible to see how first stage torque is zero ($T_{GTs1} = 0$), the contribution of torque that arrives to the carrier (C_1) is given totally by the EM, and the output torque from the carrier C_2 is in accordance with the eq.(2.65) with ($T_{Gts1} = 0$).

The same results obtained in the Green Taxi phase with a stiffness that varies over time are reported.

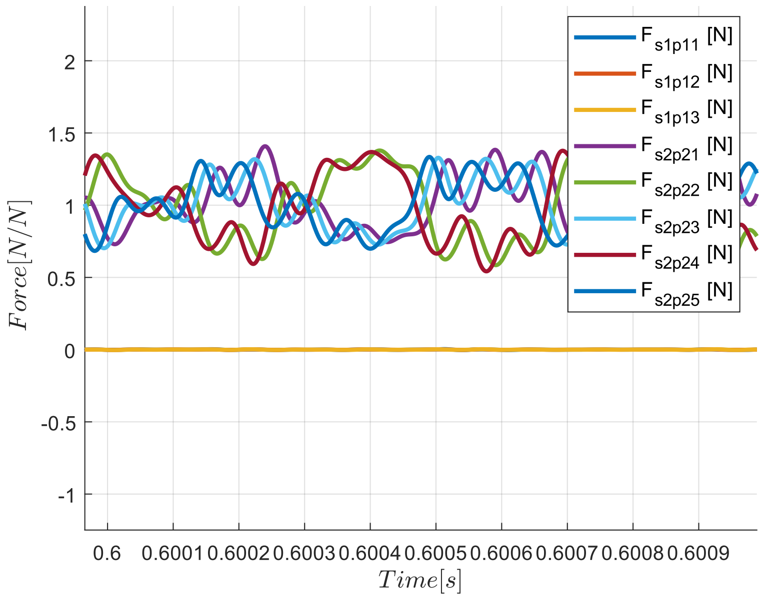

Figure 4.21: Forces GB - Variable Stiffness - Taxi Phase

The Figure 4.21 shows how the forces on the first stage are always null in accordance with Figure 4.17; the forces on the second stage have a variable trend over time, each has a certain phase delay with the other, but average value of all matches that reported in Figure 4.18.

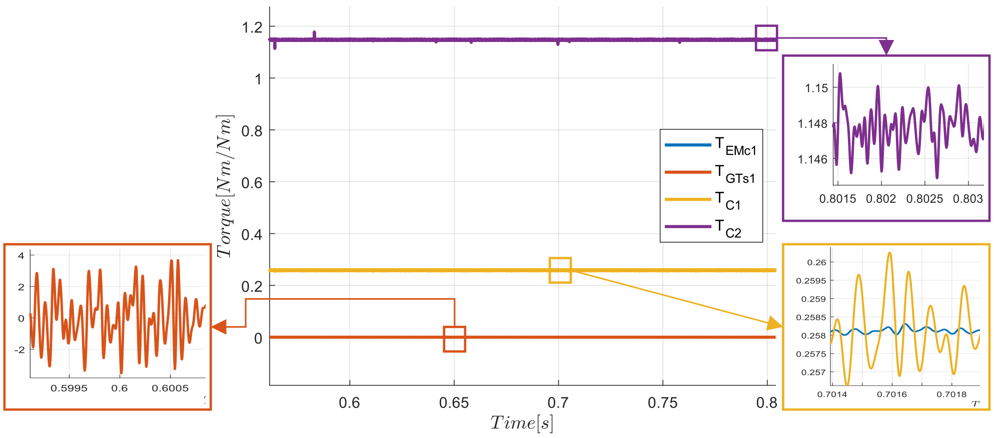

Figure 4.22: Torques GB - Variable Stiffness - Taxi Phase

In this case, in Figure 4.22, it is possible to see: the solar torque of the first stage has a variable trend, but a zero mean value; the output torque of the first stage carrier (T_{C1}) varies over time depending on the body diagram shown in Figure 3.12 and the average value of this torque matches the output of the EM (T_{EMc1}); the torque output from the second carrier (T_{C2}) has a more variable trend over time as it turns out to be the product between the torque of the EM and the transmission ratio of the second stage in accordance with the eq.(2.65).

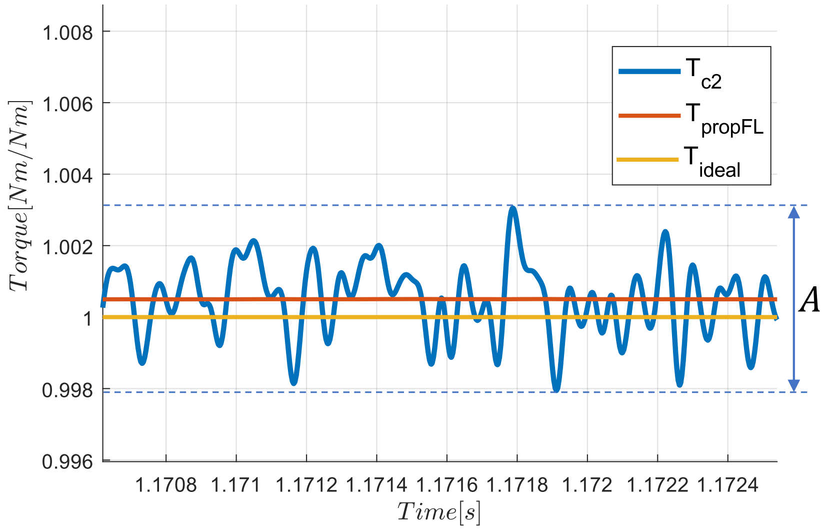

Figure 4.23: Torques Output GB - Variable Stiffness - Taxi Phase

In the end, the Figure 4.23 shows:

- the trend of the torque coming out of the second stage (T_{C2}) is in agreement with that shown in Figure 4.23 (purple box);
- the difference between the maximum and minimum value (A) is 0.5 per cent of the ideal torque (T_{ideal});
- the average value of the output torque of the GB (T_{C2}) matches the T_{ideal} and the difference between this and the fluid dynamic torque (T_{propFL}) is negligible;
- the comparison between Figures 4.15 and 4.23 shows that the difference between the torques is less in the green taxi phase than the cruise.

Chapter 5

Conclusion and Future Development

In conclusion, it is possible to note how the choice of the best architecture in terms of mass and volume for a transmission for a turboprop aircraft falls on a planetary-type double-stage (In-Line) gearbox compared to an Off-Set configuration with double speed jump.

The transition from a conventional propulsion gearbox (GB) to a hybrid parallel type (cGB) is strongly related to the correct choice of both the type of electric motor to be adopted, both at its speed of rotation. Moreover, a high-speed electric motor is not necessarily adaptable to a given transmission architecture and the higher speed is the most suitable. Therefore, chosen the type of flow of the electric motor, the rotation speed of the latter affects the gear ratio reached by the transmission but has a low effect in terms of mass flow to the entire system (the electric motor is shaped by a power function where $m_{[kg]} = f(P_{[kW]}, \omega_{[rad/s]}, \alpha_{[-]})$).

The results obtained from conventional gearbox have been shown to have power characteristics in line with today's turboprops.

The results obtained from the dynamic behavior of the transmission are in line with the torques produced by the propeller of the aircraft. Differences below 1 per cent occur at all stages of the mission (taxi, take-off and cruise) using a constant gear-up stiffness; while with a variable stiffness as a function of time there are maximum differences of about 2 per cent at take-off.

Differences with a constant stiffness are lower in modulus than with variable stiffness. Moreover, in this case, the maximum amplitudes in the output torque from the transmission have an amplitude equal to 1.2 per cent of the mean value of the same torque (take-off).

The dynamic fluid torque does not show any type of oscillation as it turns out to be that obtained from the maps of propeller operation and therefore only in function of the fluid dynamic conditions in which this work. In other words, it is not depending by the model order number.

Torque oscillations in the taxi phase are lower than in the cruise phase consistent with the lack of torque input from the gas turbine ($T_{GTs1} = 0$).

The pitch angle of the propeller is also consistent with the flight phase of the aircraft. Considering a second order modeling of the Pitch this produce small oscillations (less than 3 percent) in the dynamic fluid torque.

Considering all this it is possible to have some ideas for future developments, such as:

- to fix the shaft lengths;
- define the geometry of the housing, the seals and its maintenance;
- define the bearing position;
- implement a model that correlates the choice of lubricant for bearings with transmission losses;
- to use a more complex dynamic model, of a revolutionary type, to identify the mechanical stress discharged on the bearings and on the housing on which to subsequently implement fatigue tests.

As a continuation of these initial ideas, it would still be possible to expand the study on other components, such as gas turbine, electric motor and propeller. In particular, define operational maps for these parts, have information on the power flows and fuel or electricity consumed, and new and wider maps of operation for different types of propellers adopted (number of different blades and angles of light).

Finally, following the previous points, it would still be possible to understand the usefulness of using or not a clutch to couple or decouple the shafts of the gas turbine and electric motor, and how this impacts both on mass and volume, both in terms of fuel consumption and energy savings.

Appendix A

Code

main.m

This is the general code through which the various sub-programs are launched starting from the loading of the inputs, to the pre-sizing file (Lewis-Hertz for each identified architecture) up to the dynamic simulation through Simulink.

```
%% MAIN
clear all; close all; clc

%% Inputs
title= "test.txt"; % Insert template you are analyzing
Power_GT = XX; %[kW] Insert Gas Turbine Power to mission phase
prop_rpm = XX; %[RPM] Insert Propeller Speed to mission phase

tetad_prop_SET_takeoff = [linspace(0,10,1000001)', XX *2*pi/60*
ones(1000001,1)]; % XX in [RPM] to [rad/s]
tetad_prop_SET_cruise = [linspace(0,10,1000001)', XX *2*pi/60*
ones(1000001,1)]; % XX in [RPM] to [rad/s]
tetad_prop_SET_GreenTaxi = [linspace(0,10,1000001)', XX *2*pi/60*
ones(1000001,1)]; % XX in [RPM] to [rad/s]

GT_rpm = XX; %[RPM] Insert Gas Turbine Speed to mission phase
Power_EM = XX; %[kW] Insert Electric Motor Power to mission phase
EM_rpm = 4.5*1e3; %[RPM] % Insert EM Speed to mission phase

%% Material
Sigma_Rp02 = XX; %[MPa] Yield strength
Cs_Lewis = XX; %[-] Safety coefficient of Lewis
Cs_Hertz = XX; %[-] Safety coefficient of Hertz
Young = 210e3; %[MPa] Form of Youg
HB = XX; % Hardness in scale Brinnell
k_EM = XX; % kg/Nm constant electric motor
```

ArchitectureName.m

The names of the various sub-programs called vary according to the type of architecture being analyzed **OffSet.m; OffSet-h1.m; OffSet-h2.m; Mixed.m; PT6ASpurGearHybrid.m**.

The last script, the one on which the dynamic transmission model is based.

```
%%Sizing
run("ArchitectureName.m") % Insert: PT_6A_Spur_Gear_Hybrid.m

Mass_EM = k_EM * T_EM^0.33; % Electric Motor Model
mass_tot_hybrid = mass_tot_convetional + Mass_EM;% Total mass of combined gearbox (cGB)

(Power_EM+Power_GT)/mass_tot_hybrid %Power Density adopted
```

Steady Speed

Sub-program loading the stationary rotation speed of the individual transmission components.

```

steady_prop = XX *2*pi/60; % Steady propeller speed - Mission Phase: Cruise Phase or Take-Off or Green Taxi [rad/s]
steady_GT = GT_rpm * 2*pi/60; % Steady GasTurbine speed - Cruise Phase  [rad/s]
steady_EM = EM_rpm * 2*pi/60; % Steady ElectricMotor speed - Cruise [rad/s]

steady_s1 = steady_GT; % Steady-state Solar Rotation Speed Stage 1 [rad/s]
steady_c1 = steady_EM; % Steady-state Carrier Rotation Speed Stage 1 [rad/s]

steady_p11 = z_s1/ (2*z_p11) *steady_s1; %(w_s1-w_c1)*z_s1/z_p11*2*pi/60; % Steady-state Planet Rotation Speed Stage 1 [rad/s]

steady_s2 = steady_GT/(1+z_r1/z_s1); % Steady-state Solar Rotation Speed Stage 2 [rad/s]
steady_c2 = steady_GT/( (1+z_r1/z_s1)*(1+z_r2/z_s2)); % Steady-state Carrier Rotation Speed Stage 2 [rad/s]

steady_p21 = z_s2/ (2*z_p21) *steady_s2;% Steady-state Planet Rotation Speed Stage 2[rad/s]
```

Input Dynamic Model GT EM.m

This script loads the parameters of the gas turbine and electric motor, such as gains and inertias.

```
run("Input_Dynamic_Model_GT_EM.m")

fprintf("\nStart Inertia and Dynamic Stiffnes and Meshing Damping about GT and EM Load\n");
eps = 0.1;

%% Material
Poisson = 0.3;
G = Young/(2*(1+Poisson)); %MPa N/m2

%% Gain - Gas Turbine
K_GT = (pi*G/1e3*d_GT^4)/(32*l_shaft); % [Nm]
c_GT = 2*eps*sqrt(K_GT*mass_d_GT);

%% Inertia Gas Turbine
I_GT = 0.5*mass_d_GT*(d_GT/1e3)^2; %kgm2

%% Gain - Electric Motor
K_EM = pi*G/1e3*d_C1^4/(32*L_C1p1);
c_EM = 2*eps*sqrt(K_EM*mass_C1);

%% Inertia Electri Motor
I_EM = 0.5*mass_d_EM*(d_EM/1e3); %kgm2
fprintf("\nEnd Inertia and Dynamic Stiffnes and Meshing Damping about GT and EM Load\n");
```

Inertia.m

This script loads the inertia of all gears inside the GB.

```
run("Inertia.m")
%% Inertia First Stage
I_s1 = 0.5*mass_s1*(r_s1/1e3)^2; %kgm2
I_p11_rot = 0.5*mass_p11*(r_p11/1e3)^2; %kgm2
I_p12_rot = 0.5*mass_p12*(r_p12/1e3)^2; %kgm2
I_p13_rot = 0.5*mass_p13*(r_p13/1e3)^2; %kgm2

I_prop = 1e2; %kgm2

%% Inertia Second Stage
I_s2  = 0.5*mass_s2*(r_s2/1e3)^2; % kgm2
I_p21_rot = 0.5*mass_p21*(r_p21/1e3)^2; % kgm2
I_p22_rot = 0.5*mass_p22*(r_p22/1e3)^2; % kgm2
I_p23_rot = 0.5*mass_p23*(r_p23/1e3)^2; % kgm2
I_p24_rot = 0.5*mass_p24*(r_p24/1e3)^2; % kgm2
I_p25_rot = 0.5*mass_p25*(r_p25/1e3)^2; % kgm2

%% Carrier
```

```
I_pt_1 = (2*pi*2.5)/(256*(w_s1/w_c1)^2) * Np_1 * b_s1 * (2*r_s1/1e3)^2 * (2*r_s1/1e3+2*r_p11/1e3)^2; % From literature
I_pt_2 = (2*pi*2.5)/(256*(w_s2/w_c2)^2) * Np_2 * b_s1 * (2*r_s2/1e3)^2 * (2*r_s2/1e3+2*r_p21/1e3)^2; % From literature
```

StiffnessGainKuangYang.m

This part loads a first type of stiffness, the fixed and constant type.

```
run("StiffnessGain_KuangYang.m")
```

StiffnessGainMesh.m

As the first, in this case the script loads a time variable stiffness, namely depending on the frequency of meshing.

```
run("Stiffness_Gain_Mesh.m")
```

Steady Angle.m

This program loads the values of the angles of the various elements when the transitory is finished. When the transitory is finished the torques and forces are expressed as the product between a gain (K) for a delta angle ($\Delta\theta$) or shift (Δx) The calculation is performed considering the Cruise phase.

```

%% Steady Angle
teta_GT_steady = 0; % [rad]
teta_s1_steady = teta_GT_steady - T_GT/K_GT ; % [rad]

teta_EM_steady = 0; %T_EM/K_EM+teta_c1_steady; % [rad]
teta_c1_steady = teta_EM_steady - T_EM/ K_EM;

teta_planet_I_steady = ((teta_s1_steady-teta_c1_steady)*r_s1/1e3 - F_s1pl1/K_sp_1) / (r_p11/1e3);


teta_prop_steady = 0; % [rad]
teta_c2_steady = T_prop/K_C2 + teta_prop_steady;% [rad]
teta_s2_steady = teta_c1_steady - T_s2/K_C1; % [rad]
teta_planet_II_steady = (teta_s2_steady*r_s2/1e3 + F_s2pl2/K_sp_2 - teta_c2_steady*r_s2/1e3)/(r_p21/1e3) ;% [rad] r_p21/1e3 * r_s2/r_r2 + r_p21/1e3

steady_pitch = XX; % [deg]
```

Propellers Data.m

This Script loads all data related to the propeller of the aircraft. In particular, it charges the power and thrust coefficients as a function of advance ratio, VTAS and propeller diameter. It also uploads pitch propeller data.

```
run("Propellers_Data.m")
```

DatiSim = SimulinkModel.slx

This is the command that starts the dynamic analysis of the cGB model via Simulink. It is possible to start two analyses, the less exorbitant one with no time-dependent meshing (**GBKconst.slx**), or the one with variable frequency of meshing in the time domain (**GBKvar.slx**).

```
DatiSim = sim("SimulinkModel.slx"); % With or whitout time-
variable stiffness meshing
```

Graph.m General script with which it is possible to show the developments of forces, torques and pitch angles.

```
run("Graph.m")
```

Bibliography

[1] Rosa Maria Arnaldo Valdés, Victor Fernando Gomez Comendador, and Luis Manuel Braga Campos. «How Much Can Carbon Taxes Contribute to Aviation Decarbonization by 2050 TFT». In: *13* 3 (2021). URL: https://www.mdpi.com/2071-1050/13/3/1086.

[2] In: (). URL: https://www.spaceconomy360.it/industria-spaziale/giu-dell85-le-co2-dellaviazione-civile-nel-2050-ecco-come-fare/.

[3] Vincent Boulanger et al. «Parallel-Hybrid Powertrain Architectures and their Challenges for a Regional Aircraft». In: (Aug. 2021). DOI: 10.2514/6.2021-2444.

[4] Monroe Conner. «NASA Armstrong Fact Sheet: NASA X-57 Maxwell». In: *Oct 28, 2019* (). URL: https://www.nasa.gov/centers/armstrong/news/FactSheets/FS-109.html.

[5] Rolls-Royce Airbus and Siemens Team up for Electric Future. «Airbus Newsroom». In: *2017, November 28* (). URL: https://www.airbus.com/en/newsroom/press-releases/2017-11-airbus-rolls-royce-and-siemens-team-up-for-electric-future.

[6] Lamouroux L. and Bénard E. «EcoPulse: a hybrid-electric regional aircraft demonstrator». In: *CEAS Aeronautical Journal* 11(2) (2019). DOI: 10.1007/s13272-019-00386-4.

[7] Cesnik et al. «EcoPulse - A hybrid-electric aircraft demonstrator». In: *CEAS Aeronautical Journal* 11(2) (). DOI: 10.1007/s13272-019-00384-6.

[8] Maria Cristina Cameretti et al. «Modeling and Investigation of a Turboprop Hybrid Electric Propulsion System». In: *Aerospace* 5.4 (2018). ISSN: 2226-4310. DOI: 10.3390/aerospace5040123. URL: https://www.mdpi.com/2226-4310/5/4/123.

[9] Vankan, Jos and Lammen, Wim. «Parallel hybrid electric propulsion architecture for single aisle aircraft - powertrain investigation». In: *MATEC Web Conf.* 304 (2019), p. 03008. DOI: 10.1051/matecconf/201930403008. URL: https://doi.org/10.1051/matecconf/201930403008.

[10] W. Johnson. «Design and Analysis of Rotorcraft». In: *NASA, Tech. rep. TP–2009-215402* (2015). URL: https://rotorcraft.arc.nasa.gov/ndarc/media/Files/reportsAndPapers/NDARC-NASA-TP-2009-215402.pdf.

[11] Senty, P. Plencner, R. M. and Wickenheiser, T. J. «Propeller performance and weight predictions appended to the Navy/NASA engine program». In: *Aircraft Propulsion And Power* (July 1, 1983). URL: https://ntrs.nasa.gov/api/citations/19830024539/downloads/19830024539.pdf.

[12] R.J. Willis. «New equations and charts pick off lightest-weight gears». In: *Product engineering 5* (1963), pp. 64–75.

[13] Ben Ebihara Dexter Johnson and Benjamin Choi Mark Siebert Gerald V. Brown Albert F. Kascak and Carl Buccieri. «NASA Glenn Research Center Program in High Power Density Motors for Aeropropulsion». In: (January 1, 2005). URL: https://ntrs.nasa.gov/citations/20060003628.

[14] Kevin Antcliff et al. «Mission Analysis and Aircraft Sizing of a Hybrid-Electric Regional Aircraft». In: (Jan. 2016). DOI: 10.2514/6.2016-1028.

[15] EASA. «EASA.IM.E.041 - Pratt and Whitney Canada PW100 series engines». In: (August 2023). URL: https://www.easa.europa.eu/en/document-library/type-certificates/engine-cs-e/easaime041-pratt-and-whitney-canada-pw100-series.

[16] EASA. «EASA.IM.E.008 - Pratt and Whitney Canada PT6A-67 series engines». In: (18 February 2022). URL: https://www.easa.europa.eu/en/document-library/type-certificates/engine-cs-e/easaime008-pratt-and-whitney-canada-pt6a-67-series.

[17] EASA. «EASA.IM.E.059 - Pratt and Whitney Canada PT6T series engines». In: (30 October 2015). URL: https://www.easa.europa.eu/en/document-library/type-certificates/engine-cs-e/easaime059-pratt-whitney-canada-pt6t-series-engines.

[18] EASA. «EASA.IM.E.017 - Pratt and Whitney Canada PW206 and PW207 series engines». In: (8 August 2022). URL: https://www.easa.europa.eu/en/document-library/type-certificates/engine-cs-e/easaime017-pratt-and-whitney-canada-pw206-and-pw207.

[19] EASA. «EASA.IM.E.126 - Pratt and Whitney Canada PW210 series engines». In: (2021). URL: https://www.easa.europa.eu/en/document-library/type-certificates/engine-cs-e/easaime126-pratt-and-whitney-canada-pw210-series.

[20] EASA. «EASA.IM.E.040 - Rolls-Royce Corporation AE 2100 series engines». In: (29 August 2008). URL: https://www.easa.europa.eu/en/document-library/type-certificates/engine-cs-e/easaime040-rolls-royce-corporation-ae-2100-series.

[21] Roll Royce. «M250 Turboprop». In: (). URL: https://www.rolls-royce.com/~/media/Files/R/Rolls-Royce/documents/customers/defence-aerospace/M250%20FIRST%20network%20directory%202015.pdf.

[22] EASA. «EASA.IM.E.010 - General Electric CT7 series engines». In: (17 December 2020). URL: https://www.easa.europa.eu/en/document-library/type-certificates/engine-cs-e/easaime010-general-electric-ct7-series-engines.

[23] EASA. «EASA.E.070 - GE M601 and H80 series turboprop engines». In: (21 June 2021). URL: https://www.easa.europa.eu/en/document-library/type-certificates/engine-cs-e/easae070-ge-m601h80-series-turboprop-engines.

[24] Aero. «World Power Systems Briefing». In: (February 2020). URL: http://tealgroup.com/images/TGCTOC/sample-wpsba.pdf.

[25] Honeywell. «TPE 331-10 Turboprop Engine». In: (). URL: https://aerospace.honeywell.com/content/dam/aerobt/en/documents/learn/products/engines/brochures/N61-1491-000-000-TPE331-10TurbopropEngine-bro.pdf.

[26] In: (). URL: https://www.novagear.ch/.

[27] N. Leque and A. Kahraman. «A Three-Dimensional Load Sharing Model of Planetary Gear Sets Having Manufacturing Errors». In: *Journal of Mechanical Design* 139 (Dec. 2016). DOI: 10.1115/1.4035554.

[28] Barry James and Owen Harris. «Predicting Unequal Planetary Load Sharing Due to Manufacturing Errors and System Deflections, with Validation Against Test Data». In: (Mar. 2002). ISSN: 0148-7191. DOI: https://doi.org/10.4271/2002-01-0699. URL: https://doi.org/10.4271/2002-01-0699.

[29] Fürst, M. Otto, M. Stahl, K. Götz, J. Siglmüller, F. «Experimental investigation of the dynamic load sharing of planetary gearboxes». In: (2022). DOI: 10.1007/s10010-021-00507-5. URL: https://doi.org/10.1007/s10010-021-00507-5.

[30] Zhixian Shen et al. «Dynamic modeling of planetary gear set with tooth surface wear». In: *Procedia Manufacturing* 49 (2020). Proceedings of the 8th International Conference on Through-Life Engineering Services – TESConf 2019, pp. 49–54. ISSN: 2351-9789. DOI: `https://doi.org/10.1016/j.promfg.2020.06.010`. URL: `https://www.sciencedirect.com/science/article/pii/S2351978920316474`.

[31] Vassallo Giorgio et al. «Analysis of the mechanical transmission of the hybrid-electric propulsion system for an innovative regional transport aircraft». In: (2022).

[32] Riccardo Calamante, Massimo Sorli, and Andrea De Martin. «Modellazione di un riduttore epicicloidale e relativa difettosità in un sistema di servocomando elettromeccanico EMA». In: (2019-2020).

[33] Lei Fan et al. «Nonlinear dynamic modeling of a helicopter planetary gear train for carrier plate crack fault diagnosis». In: *Chinese Journal of Aeronautics* 29.3 (2016), pp. 675–687. ISSN: 1000-9361. DOI: `https://doi.org/10.1016/j.cja.2016.04.008`. URL: `https://www.sciencedirect.com/science/article/pii/S1000936116300292`.

[34] *An Estimate of Mesh Stiffness and Load Sharing Ratio of a Spur Gear Pair*. Vol. 6th International Power Transmission and Gearing Conference: Advancing Power Transmission Into the 21st Century. International Design Engineering Technical Conferences and Computers and Information in Engineering Conference. Sept. 1992, pp. 1–9. DOI: `10.1115/DETC1992-0001`. eprint: `https://asmedigitalcollection.asme.org/IDETC-CIE/proceedings-pdf/DETC92/09372/1/6670316/1\_1\_detc1992-0001.pdf`. URL: `https://doi.org/10.1115/DETC1992-0001`.

[35] R. G. Parker and J. Lin. «Mesh Phasing Relationships in Planetary and Epicyclic Gears ». In: *Journal of Mechanical Design* 126.2 (May 2004), pp. 365–370. ISSN: 1050-0472. DOI: `10.1115/1.1667892`. eprint: `https://asmedigitalcollection.asme.org/mechanicaldesign/article-pdf/126/2/365/5556959/365\_1.pdf`. URL: `https://doi.org/10.1115/1.1667892`.

[36] Bertucci Alessandro, Jacazio Giovanni, and Sorli Massimo. «Mathematical Model of a Epicyclic Reducer Type I». In: ().

[37] Mustafa Cavcar. «The International Standard Atmosphere (ISA)». In: *Anadolu University* (). URL: `http://fisicaatmo.at.fcen.uba.ar/practicas/ISAweb.pdf`.

[38] Paola Di Mascio et al. «Optimization of Aircraft Taxiing Strategies to Reduce the Impacts of Landing and Take-Off Cycle at Airports». In: *Sustainability* 14 (2022). ISSN: 2071-1050. DOI: `10.3390/su14159692`. URL: `https://www.mdpi.com/2071-1050/14/15/9692`.

[39] Anaïs Luisa Habermann et al. «Study of a Regional Turboprop Aircraft with Electrically Assisted Turboshaft». In: *Aerospace* 10.6 (2023). ISSN: 2226-4310. DOI: `10.3390/aerospace10060529`. URL: `https://www.mdpi.com/2226-4310/10/6/529`.